Topics in Physics and Astrophysics of LIGO

Thesis by

Yuri Levin

In Partial Fulfillment of the Requirements

for the Degree of

Doctor of Philosophy

California Institute of Technology

Pasadena, California

1999

(Submitted May 7, 1999)

ii

Acknowledgements

I thank Kip Thorne for excellent supervision, for his open heart and wise counsel throughout the years I spent at Caltech. Conversations with Kip have been an infinite source of inspiration and optimism.

Kip has withdrawn from being a co-author of any of my publications; however, he is responsible for a significant number of ideas that went into this thesis, and for clarity of the prose of its published part. Kip had also spent long and patient hours in almost futile attempts to teach me the basics of English grammar.

Vladimir Borisovich Braginsky has taught me his unique way of thinking about quantum measurements, has suggested to me two projects which eventually resulted in publications, and was a collaborator in the third one. I thank Vladimir for his friendship, hospitality, encouragement, optimism, and for sharing his unorthodox opinions about Russian politics.

I thank Farid Khalili, Nir Shaviv and Sergey Vyatchanin for fruitful collaboration and friendship.

I thank University of Melbourne for hospitality during my annual visits.

Over the years, I have learned a lot from scientific discussions with Anton Kapustin, Glenn Soberman, Peter Goldreich, Ron Drever, Sterl Phinney, Lars Bildsten, Lee Lindblom, Ann Esin, Jeff Kimble, Eugene Chiang, Ben Owen, Reem Sari and Rick Jenet. The free and democratic spirit of the TAPIR group helped me to enter the field of theoretical astrophysics (including relativity).

I thank Jane Fridlyand, Renee Frisbie, Julie Kanevsky, Anton Kapustin, Ania Kashina, Julia Kempe, Rada Konvisser, Ruben Krasnopolsky, Te-Yi Kung, Yoram Lithwick, Vladik and Nina Logvinenko, Eugene, Lialia and Sasha Miloslavsky, Ranjan Mukhopadhayay, Peter Pich, Anoop Prasad, Michele Pickerell, Alex Samuel, Hilla Shaviv, Julia Shifman and Sergey Skorik for their friendship, food and support during difficult times.

Abstract

This thesis deals with three topics, all of which are related to the generation or detection of gravitational waves:

(I) **The Standard Quantum Limit (SQL) for LIGO and Quantum Non-demolition (QND) measurements, which allow one to overcome the SQL.** Two particular QND measurement schemes are considered: (i) a Speed Meter, in which a small Fabry-Perot cavity attached to a LIGO test mass produces a phase shift proportional to the test mass's speed; and (ii) the Braginsky-Khalili nonlinear meter (BK-meter), in which a gravity-wave-induced motion of the nodes of the light beam inside a LIGO optical cavity is read out using a nonlinear medium which couples light to a microwave readout device. Our analysis shows that

(a) Using the Speed Meter one can perform naturally a **broad-band** QND measurement of a force acting on the test mass; however, this requires circulating light power which is unrealistically high for LIGO.

(b) The BK-meter can provide a natural way to perform a **narrow-band** QND measurement of a force acting on the mirrors of the optical cavity.

While neither of these QND measurement schemes can be immediately implemented for LIGO, they might provide conceptual steps towards the design of a practical QND interferometer.

(II) **Mechanical thermal noise in LIGO**. We develop a new method of calculating thermal noise in mechanical systems, which is based on a direct application of the Fluctuation-Dissipation theorem. This method is capable of handling mechanical systems with inhomogeneous dissipation, by contrast with previous methods (based on decomposing motion of the system into normal modes), which give incorrect results when the dissipation is inhomogeneous.

We apply our direct method to an **internal** thermal noise in LIGO test masses. We find that:

(a) The test-mass surface defects will make a larger contribution to thermal noise than was previously inferred by combining the (incorrect) mode-sum method with measurements of the Q's of the test masses' modes.

(b) Our direct method is more precise and computationally less expensive for small beam sizes than the previous mode-sum method.

We also apply our direct method of analysis to **suspension** thermal noise in LIGO. We find that by careful positioning the laser beam spot on the mirror face and by monitoring independently the motion of the suspension wires, it may be possible to reduce the suspension thermal noise by a factor ~ 100 in spectral density.

(III) **R-modes in Neutron Stars (NS) in Low-Mass X-ray Binaries (LMXBs)**. We study the suggestion that the accretion of gas onto a neutron star in an LMXB triggers an instability in which the star's r-modes are amplified by gravitational-wave emission. We find that if this is the case, then the subsequent neutron-star evolution depends critically on whether the neutron-star viscosity decreases with temperature, or is temperature-independent.

In the former case, the Neutron Star goes through runaway cycles of rapid (~ 1 month) heating—rapid (~ 1 month) spindown—slow ($\sim 10^5$ years) cooling—slow ($\sim 10^6$ years) spin-up. In this scenario the duration of the gravitational radiation from the unstable r-modes is so short that even LIGO-III interferometers are unlikely to be able to catch a single LMXB in the throes of its gravitational-wave emission.

In the latter (temperature-independent) case, however, the Neutron Star probably settles down into an equilibrium state with constant spin rate and temperature, and becomes a steady emitter of gravitational waves, which might be detectible by LIGO-II interferometers.

All of the capters in this thesis, except the introductory chapter I, have been published or are in press.

Contents

4 Runaway heating by r-modes of neutron stars in Low-Mass X-ray binaries (paper V)   106

List of Figures

Chapter 1 Introduction

In some heuristic sense, LIGO [1] (the Laser Interferometer Gravitational-wave Observatory) can be thought of as a constant battle between God and Devils. "God" provides astrophysical sources, which produce gravitational waves; through LIGO, humans will detect and measure these waves and study the Universe (which is God's creation, some argue). "Devils," on the other hand, will keep confusing our knowledge of the Universe by introducing microphysical noise into the gravitational-wave detectors.

Chapters II and III of this thesis study the nature of some microphysical "devils" and ways to neutralize their actions, while Chapter IV studies a particular class of astrophysical sources of gravitational waves.

More specifically, Chapter II (papers I and II) studies detector noise which is fundamentally due to the quantum-mechanical nature of the LIGO test masses. Techniques to reduce this quantum-mechanical noise are called Quantum Nondemolition (QND) measurements. In Chapter II we analyze two specific QND measurement schemes.

Chapter III (papers III and IV) concentrates on issues in thermal noise in LIGO test masses and their suspensions—i.e., noise that is ultimately caused by local dissipative processes ("anti-Maxwell demons"). We develop a theoretical approach which allows us to better understand the thermal noise in LIGO, and suggests ways of reducing it.

Chapter IV (paper V) deals with r-modes in strongly accreting rapidly rotating neutron stars. R-modes are a class of oscillatory motions in rotating stars, which are similar to Rossby waves in the ocean in that their restoring force is Coriolis in origin and disappears if the star is nonrotating. When r-modes are excited, they

---

[1]Everything in this section equally applies to other intereferometric gravitational wave detection systems—to VIRGO, GEO-600, TAMA, etc.

emit gravitational waves and grow as a result of gravitational-radiation reaction, with the growth energy coming from the star's rotation. We study the thermal and spin evolution of neutron stars, which are spun up by accretion to high rotational frequencies (~ 300Hz) and in which the r-modes become unstable.

In what follows we give a separate subintroduction for each of these chapters.

1.1 Towards Quantum Nondemolition Measurement for LIGO

In this section of the Introduction we discuss the limit that Quantum Mechanics places on the precision of a displacement measurement for a free mass. Since LIGO measures the relative displacement of freely suspended test masses on which gravitational waves act, this "free-mass standard quantum limit" constrains LIGO's gravitational-wave sensitivity. We then discuss some ideas on how to overcome this quantum-mechanical limit in the context of LIGO.

1.1.1 Standard Quantum Limit for a free test mass.

Let us consider a measurement in which a displacement x of some free mass m is monitored over a time interval of duration τ. Then, unless a measuring apparatus is prepared in some special way, there is a quantum-mechanical limit (called the Standard Quantum Limit, abbreviated as SQL) on how well such a measurement can be performed (Braginsky and Khalili, 1992). The error of measurement averaged over the duration of the measurement process cannot be less than

$$\Delta x_{\text{SQL}} = \sqrt{\frac{\hbar\tau}{m}}. \tag{1.1}$$

Special ways of preparing a measuring apparatus so that the limit (1.1) can be overcome are referred to as "Quantum Nondemolition (QND) measurements" [2].

---

[2]The notions of SQL and of QND measurement are used in broader contexts than just monitoring displacement of a free mass. They are especially extensively used by the Quantum Optics community.

Qualitatively, the origin of the SQL can be demonstrated as follows:

Consider an idealized process of monitoring x, which consists of two discrete displacement measurements, x_1 and x_2, taken at the beginning and end of the time interval τ respectively. If the precision of the first measurement is Δx_1, then due to the Heisenberg uncertainty principle the test mass should get a momentum kick, the value of which has an uncertainty $\Delta p_1 \geq \hbar/\Delta x_1$. If Δx_1 and Δp_1 are uncorrelated (no "special preparation" of the measuring device), then the uncertainty of the second measurement is

$$(\Delta x_2)^2 = (\Delta x_1)^2 + \left(\frac{\Delta p_1}{m}\tau\right)^2 + (\delta x_2)^2, \tag{1.2}$$

where δx_2 is the intrinsic error of the second measurement (i.e., the noise superposed onto the output by the measuring device itself). Therefore, the following inequality holds:

$$(\Delta x_2)^2 \geq (\Delta x_1)^2 + \frac{\hbar^2\tau^2}{4(\Delta x_1)^2 m^2}. \tag{1.3}$$

Minimizing Eq. (1.3) with respect to Δx_1, we obtain the Standard Quantum Limit (SQL):

$$\Delta x_2 \geq \sqrt{\frac{\hbar\tau}{m}}. \tag{1.4}$$

This SQL is not an artifact of our idealized form of measurement. Every measurement of position introduces a *back-action* kick, which affects the overall precision of subsequent position measurements. The process of a realistic continuous position monitoring introduces a *back-action* random force acting on the test mass. The more intrinsically precise is the measurement, the greater is this back-action force. This statement can be quantified in the following way:

Let $\hat{x}(t)$ be the operator for the test-mass position in the Heisenberg picture. Then the output of a continuous position measurement $\bar{x}(t)$ can be written as (Braginsky and Khalili, 1992)

$$\bar{x}(t) = \hat{x}(t) + \delta x(t). \tag{1.5}$$

Here $\delta x(t)$ is an operator representing the *intrinsic* noise introduced by the measuring device itself [analog of δx_2 in Eq. (1.2)]. (Example: if the measuring device is an

interferometer like LIGO, then $\delta x(t)$ is the measurement error due to shot noise).
One can construct the spectral density $S_x(f)$ of this intrinsic noise:

$$S_x(f) = \int_{-\infty}^{\infty} \langle \delta x(0)\delta x(t) \rangle e^{2\pi i f t} dt. \tag{1.6}$$

We shall denote by $S_F(f)$ the spectral density of the continuous back-action force
F_{BA} acting on the test mass. (For LIGO the role of the back-action is played by
the radiation-pressure noise). The Heisenberg uncertainty relation is enforced by the
following inequality:

$$S_F(f)S_x(f) \geq \frac{\hbar^2}{4}, \tag{1.7}$$

which holds as long as δx and the back-action force F_{BA} are uncorrelated (i.e., when
there is no special preparation of the measuring device) (Braginsky and Khalili, 1992).
In this case, the spectral density of the total noise in the displacement measurement
is given by the sum of the intrinsic and the back-action noises:

$$S_x^{\mathrm{total}}(f) = S_x(f) + |Z(f)|^2 S_F(f). \tag{1.8}$$

Here $Z(f)$ is the admittance of the mechanical system; for a free test mass $Z(f) = -m^{-1}(2\pi f)^{-2}$.

Taking into account the generalized uncertainty relation (1.7), one can infer from
Eq. (1.8) that

$$S_x^{\mathrm{total}}(f) \geq \frac{\hbar}{m(2\pi f)^2}. \tag{1.9}$$

Equation (1.9) is a rigorous formulation in spectral language of the Standard Quantum
Limit for a free mass.

1.1.2 Standard Quantum Limit for LIGO

In LIGO, rather than measuring the displacement of a single free mass, one measures a linear combination x_{LIGO} of displacements of the four different test masses:

$$\hat{x}_{\text{LIGO}} = (\hat{x}_1 - \hat{x}_2) - (\hat{x}_3 - \hat{x}_4). \tag{1.10}$$

One can view $\hat{x}_{\text{LIGO}}$ as one of the generalized coordinates of the sysem of four test masses; the corresponding conjugate momentum operator is

$$\hat{p}_{\text{LIGO}} = \frac{1}{4}\left[(\hat{p}_1 - \hat{p}_2) - (\hat{p}_3 - \hat{p}_4)\right]. \tag{1.11}$$

The generalized momentum operator $\hat{p}_{\text{LIGO}}$ is chosen in such a way that $[\hat{x}_{\text{LIGO}}, \hat{p}_{\text{LIGO}}] = i\hbar$. One can go through an argument which is completely analogous to the argument in the previous section, and obtain the SQL for x_{LIGO}. The only difference from the case of a free mass is that $dx_{\text{freemass}}/dt = p_{\text{freemass}}/m$, whereas for LIGO there is an extra factor of four: $dx_{\text{LIGO}}/dt = 4p_{\text{LIGO}}/m$. Therefore, after simple algebra, one gets

$$\Delta x_{\text{LIGO}}^{\text{SQL}} = 2\Delta x_{\text{freemass}}^{\text{SQL}}, \tag{1.12}$$

or, in spectral language,

$$S_{x_{\text{LIGO}}}^{\text{SQL}} = \frac{4\hbar}{m(2\pi f)^2}, \tag{1.13}$$

where m is the mass of each of the identical test masses. It is conventional to discuss LIGO's output in the language of the interferometer's strain $h = x_{\text{LIGO}}/L$, where L is the length of each of the interferometer's arms. In terms of strain the SQL for LIGO becomes

$$\tilde{h}^{\text{SQL}}(f) = \frac{1}{L}\sqrt{S_{x_{\text{LIGO}}}^{\text{SQL}}} = 8.3 \times 10^{-23} \left(\frac{10\text{kg}}{m}\right)^{1/2} \left(\frac{30\text{Hz}}{f}\right) \left(\frac{4\text{km}}{L}\right) \text{Hz}^{-1/2}. \tag{1.14}$$

In LIGO-II interferometers (ca. 2004-2007) the quantum noise (1.14) will be comparable to the suspension thermal noise and comparable to the shot noise at $f \sim 100\text{Hz}$

(the minimum of the LIGO noise curve), and thus will be a significant contributor to the total noise (Weiss, R. et al. 1998). To overcome the SQL in LIGO III (ca. 2008), it will be necessary to increase the mass m from 11kg to, say, 300kg (which may be impractical), or to use techniques of Quantum Nondemolition measurements, which are the subject of the next section.

1.1.3   Quantum Nondemolition (QND) measurement for LIGO

It has been known for almost twenty years that the SQL is not a fundamental limit, and that in principle it is possible to beat the SQL by so-called QND measurement techniques (Braginsky and Khalili, 1992). However, all of the QND schemes proposed so far are of gedanken nature and are not practical for implementation in LIGO. The two main difficulties in inventing a practical QND scheme are:

(1) It is hard to invent a QND measurement which does not require very large circulating optical power, and

(2) It is hard to invent a QND scheme which works over a broad range of frequencies $\Delta f \sim f$, which is what is required in LIGO.

The yet unrealized "Holy Grail" of the field has been to find some *practical* way of implementing QND measurements. The work in this thesis does not change this state of affairs; instead, two more purely gedanken schemes for QND measurements are discussed in papers I and II. We would like to believe that these new gedanken schemes may provide insight that will aid in the search for a practical solution.

Two QND measurement procedures have been previously invented in the context of optical measurements of test-mass *displacement* (Unruh 1982, Jaekel and Reynaud 1990, Vyatchanin et al. 1993, 1995, 1996). We first discuss these measurements from an intuitive point of view, and then make a brief excursion into the mathematical formalism. We show that in this class of procedures it is difficult to perform a *broadband* QND measurement.

We then outline in general terms QND techniques based on measuring the test-mass speed (Braginsky and Khalili, 1990; paper I of this thesis; Braginsky et al.,
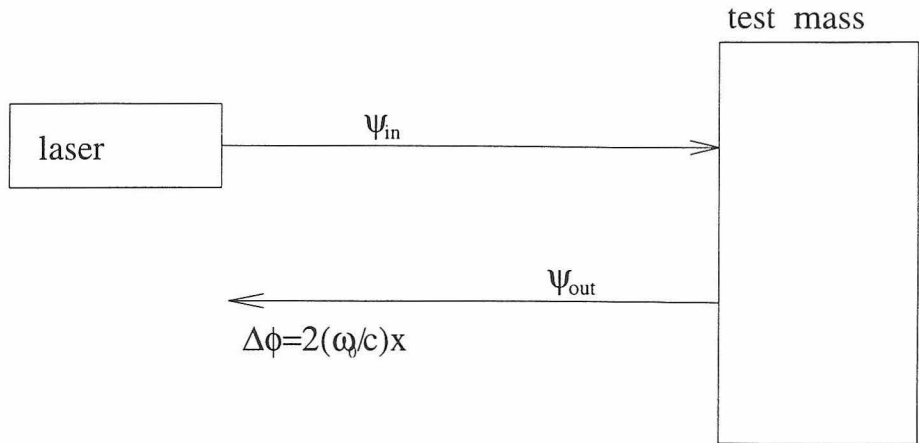
Figure 1.1: **An optical transducer.**
The test-mass displacement x is determined by measuring the phase shift ϕ of the reflected light.

1999). We explain why speed meters are generally more suitable to perform *broad-band* QND measurements, by contrast with displacement meters. This will enable the reader to put in context paper I of this thesis.

Finally, we will give a brief introduction to paper II, which deals with a particular narrow-band QND measurement scheme.

QND in the context of displacement measurements. In this subsection we restrict ourselves to optical measurements of the displacement of a single test mass. (The generalization to LIGO is straightforward.) Figure 1.1 depicts a particular displacement measurement that we have in mind: a laser beam is reflected off the test mass, and the displacement of this test mass is inferred by measuring the phase shift of the reflected light. Figures 1.2a and 1.2b present cartoons of the quantum state of the incident and reflected light respectively.

These cartoons provide intuitive insight for understanding and inventing QND schemes. The incident light is assumed to be in a coherent state, with equal magnitudes of phase and relative amplitude fluctuations. [In this we follow a series of papers by Vyatchanin et al. 1993, 95, 96. In the other version of this QND measurement (Unruh 1982, Jaekel and Reynaud 1990) the input light is squeezed.] We draw a coherent state as a circular blob of "quantum uncertainty" in the light's os-
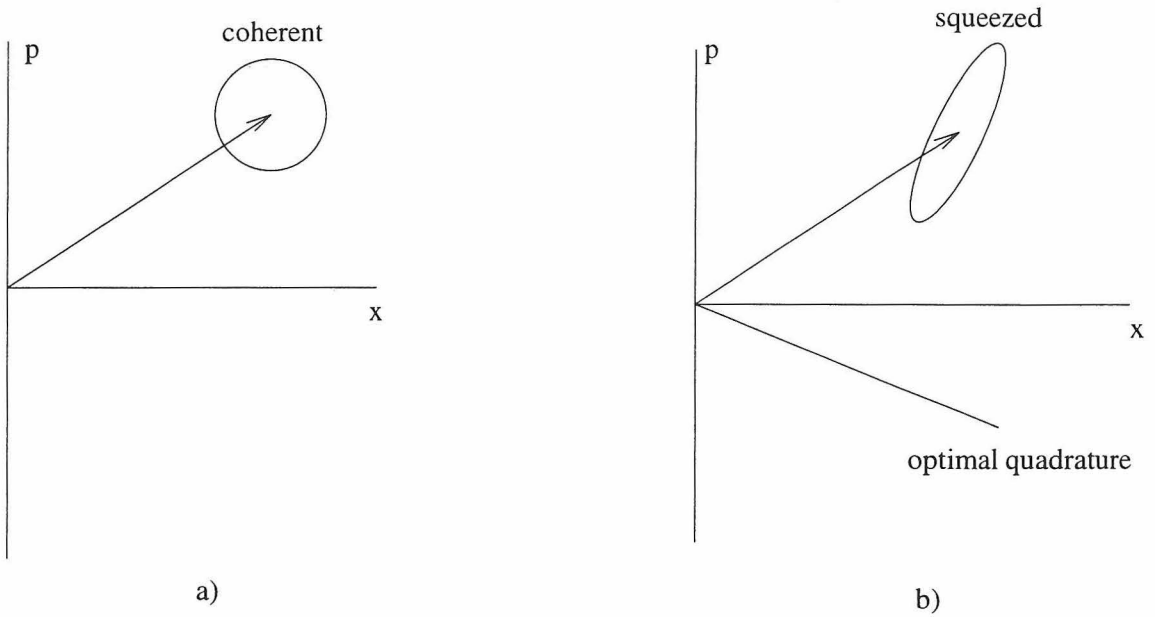
Figure 1.2: **Phase-space cartoons of incident coherent light (Fig. 1.2a) and reflected squeezed light (Fig. 1.2b) for the measurement scheme of Fig. 1.1.**
These cartoons treat the light as a single-mode oscillator and therefore have only intuitive value. The optimal quadrature of the light, which should be used when measuring an external force acting on the test mass, is the one perpendicular to the large axis of the squeezed ellipse (Fig. 1.2b).

cillator phase space [3]. The amplitude fluctuations of the incoming light drive the displacement fluctuations of the test mass; these displacement fluctuations in turn create fluctuations in the phase of the reflected light. Thus, the reflected light will be in a state with phase and amplitude correlated, i.e., in a particular case of a *squeezed* state. The cartoon of the quantum state of this reflected light is shown in Fig.1.2b; the "blob" of quantum phase and amplitude uncertainty is an inclined ellipse, which depicts the correlation between the amplitude and the phase of the reflected light.

We observe that the phase noise of the reflected light is larger than that of the incoming light. This increase in the phase uncertainty due to the radiation-pressure back-action enforces the SQL.

If our aim is to measure an external force acting on the test mass, then instead of measuring the phase one can do better by measuring a particular linear combination of the phase and amplitude of the reflected light. A linear combination of phase and amplitude is called a *quadrature* in the language of Quantum Optics. As was pointed out by Vyatchanin and Matsko (1993), when monitoring an *external* force the optimal quadrature to measure is the one perpendicular to the small axis of the ellipse of "quantum uncertainty" in Fig.1.2b. Before we describe how to implement such a measurement, let us discuss more mathematically the squeezing of the light by interaction with a test mass (the so-called ponderomotive squeezing).

It is convenient to consider both the incoming and outgoing light as a sum of a classical monochromatic wave and quantum vacuum fluctuations (Vyatchanin and Matsko, 1993):

$$\psi_{\text{in}} = A e^{i\omega_0(t-x/c)} + \int_{-\omega_0}^{\infty} d\Omega \sqrt{\frac{\hbar(\omega_0+\Omega)}{Sc}} a_{\text{in}}(\omega_0+\Omega) e^{i(\omega_0+\Omega)(t-x/c)} + \text{c.c.}, \quad (1.15)$$

$$\psi_{\text{out}} = A e^{i\omega_0(t+x/c)} + \int_{-\omega_0}^{\infty} d\Omega \sqrt{\frac{\hbar(\omega_0+\Omega)}{Sc}} a_{\text{out}}(\omega_0+\Omega) e^{i(\omega_0+\Omega)(t+x/c)} + \text{c.c.} \quad (1.16)$$

---

[3] For a single-mode oscillator these cartoons can be justified rigorously in terms of Wigner pseudo-probability functions. However, in our situation there are many modes involved, and therefore one cannot rigorously use a single-mode phase space to describe the light. It serves a purely intuitive purpose here.

Here $\psi_{\text{in/out}}$ stands for an in/outgoing light wave operator, which for our purposes can be considered to be scalar; ω_0 is the angular frequency of the incoming light, S is the area of the beam, c is the speed of light, and A is chosen to be real. The operators $a_{\text{in}}(\omega)$ represent vacuum quantum fluctuations superposed on the classical monochromatic wave. They observe the usual commutation relations for a scalar field quantized in one spatial dimension: $[a(\omega_1), a(\omega_2)] = 0$ and $[a(\omega_1), a^\dagger(\omega_2)] = 2\pi\delta(\omega_1 - \omega_2)$. The incoming light power is given by $W = cSA^2/4\pi$.

The operator for the radiation-pressure force is $F_{\text{rp}} = (S/2\pi)\psi_{\text{in}}^\dagger\psi_{\text{in}}$, and the Fourier component of its fluctuating part is

$$F_{\text{fl}}(\Omega) = 2\sqrt{\frac{W\hbar\omega_0}{2\pi c^2}}\left[a_{\text{in}}(\omega_0 + \Omega) + a_{\text{in}}^\dagger(\omega_0 - \Omega)\right]. \qquad (1.17)$$

This fluctuating force will displace the test mass randomly; the fluctuating displacement is given by

$$\hat{x}_{\text{fl}}(\Omega) = -\frac{F_{\text{fl}}(\Omega)}{m\Omega^2}. \qquad (1.18)$$

The operators for the outgoing modes are related in the Heisenberg picture to the operator of the test-mass displacement $\hat{x}$ through $a_{\text{out}}(\omega_0 + \Omega) = a_{\text{in}}(\omega_0 + \Omega) + 2i\sqrt{2\pi W\omega_0/\hbar c^2}\hat{x}$. Therefore,

$$
\begin{aligned}
a_{\text{out}}(\omega_0 + \Omega) &= a_{\text{in}}(\omega_0 + \Omega) - i\frac{2W\omega_0}{mc^2\Omega^2}\left[a_{\text{in}}(\omega_0 + \Omega) + a_{\text{in}}^\dagger(\omega_0 - \Omega)\right] \\
&+ 2i\sqrt{\frac{2\pi W\omega_0}{\hbar c^2}}x_s(\Omega),
\end{aligned} \qquad (1.19)
$$

where x_s is the test-mass displacement caused by an external perturbation other than the radiation-pressure force (e.g., by a gravitational wave). Equation (1.19) is a multimode Bogolyubov transformation, and the state of the reflected light is a so-called multimode squeezed state (see, e.g., Milburn and Walls 1994).

The process of measuring a particular quadrature of the outgoing field is mathe-

matically equivalent to measuring quantity

$$B(\phi, \Omega) = e^{i\phi(\Omega)} a_{\text{out}}(\omega_0 + \Omega) + e^{-i\phi(\Omega)} a_{\text{out}}^\dagger(\omega_0 - \Omega). \qquad (1.20)$$

The optimal choice of $\phi(\Omega)$ for measuring the signal x_s (corresponding to the quadrature perpendicular to the squeezed ellipse of Fig. 1.2b) turns out to be (Vyatchanin et al. 1993, 1995, 1996)

$$\phi(\Omega) = -\cot^{-1}(2W\omega_0/mc^2\Omega^2). \qquad (1.21)$$

With this choice of ϕ, the spectral density of the noise when measuring x_s is

$$S_x^{\text{total}}(\Omega) = \frac{W_{\text{SQL}}}{W} S_x^{\text{SQL}}(\Omega) = \frac{W_{\text{SQL}}}{W} \frac{\hbar}{m\Omega^2}, \qquad (1.22)$$

where W is the power of the incoming light and $W_{\text{SQL}} = mc^2\Omega^2/2\omega_0$. We see that by increasing the input power W beyond W_{SQL}, we can beat the SQL, thus performing a QND measurement on the test mass. The $S_x \propto W^{-1}$ scaling of the noise spectral density with optical input power is a common feature of all optical QND measurements. [In the scheme proposed by Unruh (1982), the input light is squeezed as well. The scaling $S_x \propto W^{-1}$ then holds if the magnitude of squeezing is kept constant.]

The practical implementation of a quadrature measurement can be performed by a homodyne detector; see Fig. 1.3 for a diagram and an explanation. A homodyne detector measures the quadrature

$$B(\Omega) = e^{i\phi} a_{\text{out}}(\omega_0 + \Omega) + e^{-i\phi} a_{\text{out}}^\dagger(\omega_0 - \Omega), \qquad (1.23)$$

where ϕ is the phase of the local oscillator used in the homodyne detection. The important experimental constraint is that ϕ is frequency-independent, by contrast with what is required for a QND measurement on a free test mass [cf. Eq. (1.21)].

This feature of frequency-independence of the homodyne phase makes the simple-minded QND scheme described above suitable only for narrow-band QND measure-
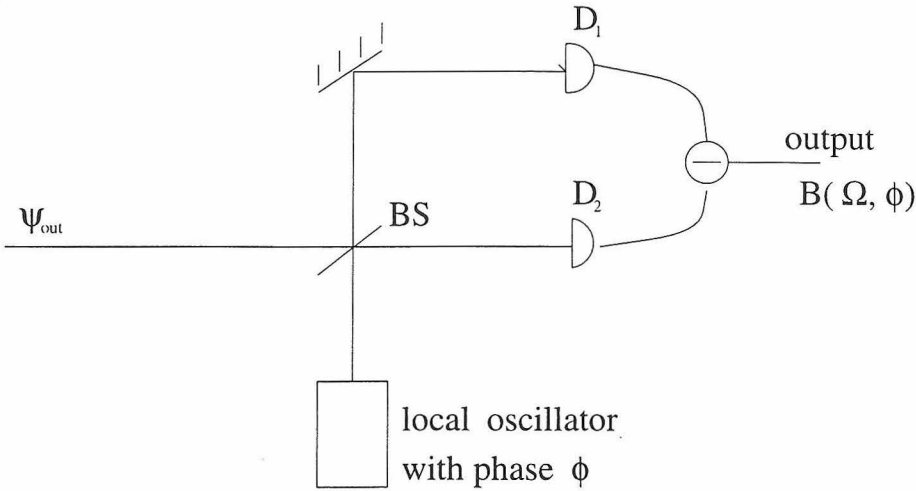
Figure 1.3: **Principle of operation of a homodyne detector.**
The beam splitter BS mixes the field ψ_{out} with the strong local oscillator field, which has a tunable phase ϕ. The currents from the two photodiodes, D_1 and D_2, are subtracted to give the output. The Fourier component of the output is the quadrature $B(\Omega, \phi) = e^{i\phi}a_{\text{out}}(\omega_0 + \Omega) + e^{-i\phi}a_{\text{out}}^{\dagger}(\omega_0 - \Omega)$.

ments.

Two methods are known which allow one to extend the ideas in this subsection to broad-band QND measurements: (1) use a speed meter instead of a displacement meter (Braginsky and Khalili 1990), or (2) put the outgoing light through a carefully tuned off-resonance Fabry-Perot cavity before performing the homodyne detection (Kimble et al. 1999). Speed meters are discussed in the next subsection and in paper I; the work on Kimble's idea is still in progress, and it will not be discussed in this thesis.

Speed meter as a QND measuring device. In the previous subsection we discussed optical schemes for a test-mass displacement measurement; in those schemes the phase shift of light reflected off a test mass was proportional to the test-mass displacement x:

$$\Delta\phi \propto x. \tag{1.24}$$

One can also construct an optical measuring device that responds to the test mass's

speed, rather than its displacement. In this case $\Delta\phi \propto \dot{x}$ or, in Fourier language,

$$\Delta\phi(\Omega) \propto i\Omega x(\Omega). \tag{1.25}$$

Particular examples of such speed meters are analyzed in a paper by Braginsky and Khalili (1990) and in paper I of this thesis; here we concentrate on the generic features of speed measurements.

From Eq. (1.25) we see that zero-frequency motion of the test mass is not coupled to light; therefore, the fluctuating radiation-pressure (back-action) force satisfies $F_\text{fl}(\Omega) = 0$ for $\Omega = 0$. More generally, for small Ω, we must have

$$F_\text{fl}(\Omega) \propto i\Omega \left[a(\omega_0 + \Omega) + a^\dagger(\omega_0 - \Omega) \right], \tag{1.26}$$

which should be compared with the analogous Eq. (1.17) for a displacement meter. Putting together Eqs. (1.18), (1.25) and (1.26), we see that

$$a_\text{out}(\omega_0 + \Omega) = a_\text{in}(\omega_0 + \Omega) + iC \left[a_\text{in}(\omega_0 + \Omega) + a_\text{in}^\dagger(\omega_0 - \Omega) \right], \tag{1.27}$$

where C is a constant which does *not* depend on frequency [by contrast with Eq. (1.19)]. Therefore, for an optimal quadrature measurement, one can use a *frequency-independent* homodyne phase. *This allows a broad-band QND measurement to be performed on a speed meter by using conventional techniques of Quantum Optics.*

A particular example of a QND measurement by a speed meter is worked out in detail in paper I. In this paper, we consider a scheme where a rigid Fabry-Perot cavity is attached to the test-mass itself. The cavity's mirrors have equal reflectivity, and it is pumped on resonance; therefore, the light goes straight through the cavity. The phase shift of the light exiting the cavity does not depend on the cavity's stationary position; however, it is sensitive to the cavity's speed.

In the paper we identify the optimal linear combination of the output modes which should be measured to extract information about an external force acting on the test mass. We devise a homodyne-detection-based QND measurement scheme,

which works for a broad range of frequencies. Unfortunately, in the paper the broad-band nature of such a measurement is not emphasized; we hope that the preceding paragraphs have filled in this gap. Nonetheless, paper I contains the first analysis of a measurement by a speed meter, in which the light field is explicitly quantized and homodyne detection is used.

Narrow-band intracavity QND measurement   Paper II presents an idea for a QND measurement which is completly different from the ideas discussed above. It is based on a proposal by Braginsky and Khalili (1996) for a new design of a gravitational-wave detector, in which the signal is read out from the *inside* of a Fabry-Perot resonator. In this scheme, the gravitational-wave-induced spatial shift of the standing optical wave inside the LIGO resonator is read out by a microwave oscillator containing an optically-nonlinear medium. The details of this design are reviewed in paper II.

We trace exactly the path by which the back-action is enforced in this scheme, starting from the microwave oscillator used for the readout, through the nonlinear medium into the light, then through the light to the test-mass mirrors that confine it. We find a side effect of this back-action, unnoticed by Braginsky and Khalili: the fluctuations of light pressure, which enforce the back-action, will be independently recorded by the microwave readout device. We show that this side effect allows one to perform a QND measurement, but only in a narrow range of frequencies.

Since paper II was written, Braginsky, Gorodetsky and Khalili (1997, 1998) have come up with new ideas for an intracavity measurement, which probably make the original Braginsky-Khalili idea obsolete. The QND scheme of paper II is not readily applicable to these new intracavity measurements, and therefore its ultimate relevance is uncertain. We include paper II in this thesis for completeness, and also because the idea for QND measurements presented in it is different from all previous QND ideas, and may suggest directions for future QND research.

1.2   Issues in thermal noise for LIGO

A LIGO interferometer generally monitors the linear combination

$$x_{\mathbf{LIGO}} = x_1 - x_2 - (x_3 - x_4) \tag{1.28}$$

of the displacements of the four test masses [cf. Eq. (1.10)]. The quantity x_i is in fact the displacement of the mirror surface of the i-th test mass, averaged over the beam spot on the mirror.

The term "thermal noise" in the context of LIGO refers to noise in the interferometer output, caused by random mechanical motions of thermal origin. In particular, each of the x_is will be fluctuating due to random thermal motion of its i-th mirror surface. Thermal noise is expected to be the dominant noise for LIGO in the frequency band of $35 - 130$Hz for LIGO-I and of $20 - 100$Hz for LIGO-II (Weiss et al. 1998).

From now on we concentrate on a single test mass, since the thermal noises from all of the test masses just add linearly in spectral density.

In general, thermal noise can be subdivided into two components:
(i) Internal thermal noise, which is directly connected to dissipative processes in the test mass itself, and
(ii) Suspension thermal noise, which is connected to dissipative processes in the fibers by which the test mass is suspended.

Before the work reported in this thesis, both suspension and internal thermal noise were analyzed by using the so-called method of normal-mode decomposition (NMD) (Saulson 1990, Gillespie and Raab 1995, Bondu and Vinet 1995). In what follows we present the ideas behind NMD, with the ultimate purpose to point out under what circumstances this method of calculation is not correct. Our presentation of NMD differs somewhat from the original presentation in Saulson (1990)

The key steps for the NMD calculation of thermal noise are:
a) Identify all the elastic normal modes of the test mass and suspension. These modes

can be characterized by generalized coordinates q_1, q_2, etc. The readout variable x [in our case, the displacement of the mirror surface averaged over the laser beam spot [cf. Eq. (3.3) of paper III] is a linear combination of these generalized coordinates:

$$x = \alpha_1 q_1 + \alpha_2 q_2 + ..., \tag{1.29}$$

where α_i are real numbers.

b) Assume that each of the modes is an *independent* (we will specify shortly what exactly is meant by this) oscillator coupled to the heat bath. Such oscillators are well described by a Langevin-like equation in the frequency domain:

$$\left[\omega_i^2 - \omega^2 - i\omega_i^2 \phi_i(\omega) \right] \tilde{q}_i(\omega) = f_i(\omega), \tag{1.30}$$

where $\tilde{q}_i(\omega)$ is the fourier component of the $q_i(t)$, the loss angle $\phi_i(\omega)$ is responsible for the damping of the i-th mode, and ω_i is the angular frequency of the i-th mode. The random Langevin force f_i satisfies the single-mode Fluctuation-Dissipation relation (Callen and Welton 1954, Saulson 1990):

$$S_{f_i}(\omega) = \frac{4 k_B T \omega_i^2}{m \omega} \phi_i(\omega), \tag{1.31}$$

where $S_{f_i}(\omega)$ is the spectral density of the Langevin force f_i, k_B is the Boltzmann constant and T is the temperature of the elastic system. Substituting Eq. (1.31) into Eq. (1.30), one can find the spectral density S_{q_i} of the thermal fluctuations of the i-th mode:

$$S_{q_i}(\omega) = \frac{4 k_B T \omega_i^2 \phi_i(\omega)}{\left[(\omega_i^2 - \omega^2)^2 + \omega_i^4 \phi_i(\omega)^2 \right] \omega}. \tag{1.32}$$

c) All of the normal modes were assumed to be *independent*; therefore the spectral density of the readout S_x is a properly weighted sum of the spectral densities of the normal modes:

$$S_x = \alpha_1^2 S_{q_1} + \alpha_2^2 S_{q_2} + ..., \tag{1.33}$$

where α's are taken from Eq. (1.29).

Saulson has argued that for most materials used in the LIGO test masses and suspensions, the loss angle $\phi(\omega)$ will be aproximately frequency-independent in the range of frequencies of interest (say, $10 - 10^4$Hz). One can then measure ϕ_i by measuring the quality factors Q_i of the various normal modes, and using the relation $\phi_i(\omega_i) = 1/Q_i$.

In practice, to use Eq. (1.33) for calculation of internal thermal noise, one needs to run costly computer simulations for a particular test mass, which evaluate the angular frequencies ω_i of the modes and their coupling coefficients to the light beam α_i. The smaller the beam size on the mirror, the larger the number of modes which contribute to the internal thermal noise. For small beam sizes the series in Eq. (1.33) converges slowly.

The NMD method has a more serious drawback than just high computational cost and poor convergence. The method heavily relies on the assumption that the modes are *independent*, i.e., *uncorrelated* with each other. Speaking mathematically, NMD assumes that $\langle f_i f_j \rangle = 0$ for $i \neq j$, i.e., that the Langevin forces of different modes are uncorrelated. Paper III shows that this assumption is valid only when the sources of dissipation are distributed homogeneously in the test mass, and that spatially inhomogeneous dissipation always introduces correlations between diferent modes. In this case, one must add complicated cross-terms to the right-hand-side of Eq. (1.33), and the NMD computations become intractable.

Paper III develops a new method, based on earlier ideas of Gonzalez and Saulson (1994), for evaluating thermal noise in mechanical systems. This method is based on a direct application of the Fluctuation-Dissipation theorem and can handle inhomogeneous dissipation and arbitrary beam sizes with fairly simple computations. The single most important result of paper III is that the dissipation at the mirror surface will make a significantly larger contribution to the internal thermal noise than inferred from NMD.

Although paper III focuses explicitly on the internal thermal noise, its philosophy and method can be equally well applied to the suspension thermal noise. In paper

IV Braginsky, Vyatchanin and I use this direct-computation method to devise and analyze a scheme for reducing suspension thermal noise by a factor ~ 10 in amplitude. The key to this reduction is a careful adjustment of the position of the beam on the test-mass-mirror, and an optical-fiber-evanescent-field monitoring of the motion of the suspension fibers.

1.3 R-modes in rapidly rotating strongly accreting neutron stars

Chandrasekhar, Friedman and Shutz (CFS) have shown that some oscillatory modes of rapidly rotating stars can be driven by gravitational-radiation reaction (Chandrasekhar 1970, Friedman and Schutz 1978). Recently Andersson (1998) has discovered, and Friedman and Morsink (1998) showed analytically, that r-modes are subject to the CFS instability. Chapter IV (paper V) considers the thermal and spin evolution of accreting neutron stars in which r-modes become unstable.

This subsection gives a brief introduction to the CFS instability and to the physical nature of r-modes in rotating stars. Its purpose is to make the contents of Chapter IV understandable for a non-expert in theoretical astrophysics.

1.3.1 The CFS instability.

Figure 1.4 shows a picture of a star that is rotating rapidly in a clockwise direction. Let's consider a mode of the star, which looks like an ocean wave propagating along the equator against the direction of the star's rotation (i.e., counterclockwise). The surface of the star appears distorted in Fig. 1.4 due to this ocean-wave mode. One can show that when the rotational frequency of the star is increased, while keeping the wave-number of the excited mode fixed, then eventually the pattern of the mode is dragged by the star in the clockwise direction, even though the mode is propagating counterclockwise relative to the star.

When being dragged forward, such a mode carries negative energy and negative

angular momentum; that is, the star as a whole has smaller energy and angular momentum when the mode is excited than when the mode has no excitation. [4]

Therefore, the rotating star can lose angular momentum and energy by growing the negative-energy oscillatory mode. If this mode is coupled to gravitational radiation, then gravitational waves carry away the excess of angular momentum and energy. In this case the mode keeps growing due to the gravitational-radiation reaction. This instability was discovered by Chandrasekhar (1970) for Maclauren spheroids, and discussed more generally by Friedman and Schutz (1978). Neutron stars provide a natural setting for the CFS instability to operate, since their rotational frequency can be very high ($\sim$ 1kHz). However, for the CFS instability to operate, the gravitational-radiation reaction has to overcome viscous damping of the modes. It turns out that for f-modes (the fundamental-order "ocean waves" described above), the rotational frequency at which the CFS instability starts operating is very close to the theoretically maximal possible rotational frequency (the so-called "break-up" frequency). Thus, the CFS instability is probably not important for f-modes in real astrophysical situations. Recently Nils Andersson (1998) discovered, and Friedman and Morsink (1998) proved analytically, that r-modes are dragged forward by rotation at any angular velocity, even very small ones, and therefore are subject to the CFS instability. Lindblom, Owen and Morsink (1998) have computed the timescales of the r-mode gravitational-radiation driven growth and of the viscous damping, and have shown that the driving dominates for rapidly spinning newborn neutron stars–and, as a result, the r-mode instability will limit the rotational frequencies of neutron stars born in supernovae. R-modes were discovered and discussed in a classic paper by Papaloizou and Pringle (1978). R-modes are essentially vorticity patterns, which move relative to a rotating star (see Figures 1.5 and 1.6). The restoring force for the r-modes is the Coriolis force; in the slow-rotation limit, the r-mode frequency f is

---

[4]The negative angular momentum and energy can be understood from the following analogy: Consider a carriage moving fast with constant velocity, and a tennis ball in the carriage which flies backwards relative to the carriage, but moves forward relative to the ground. Then the motion of the ball reduces the momentum and kinetic energy of the whole system relative to what it would be if the ball were lying on the carriage floor. In this sense, the ball carries negative momentum and negative kinetic energy.

counterpropagating "ocean wave"
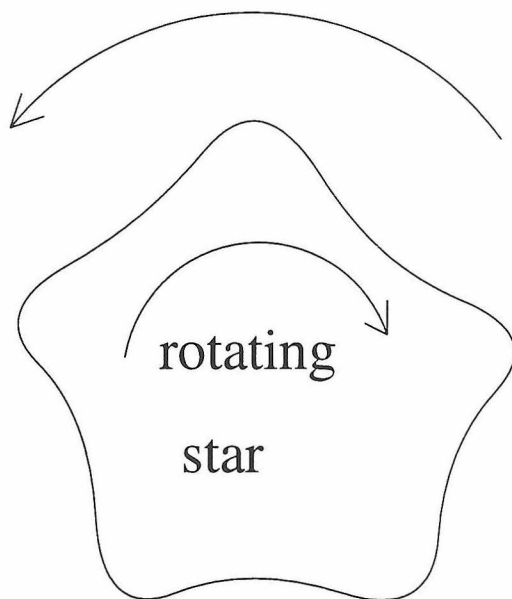
Figure 1.4: **The CFS instability.**
An equatorial "ocean wave" oscillatory mode is propagating counter to the rotation of the star. When the star rotates fast enough, the mode pattern gets dragged along in the direction of the star's rotation. Then the mode carries negative energy and angular momentum.

Fluid Motion in the $m = 2$ r-mode
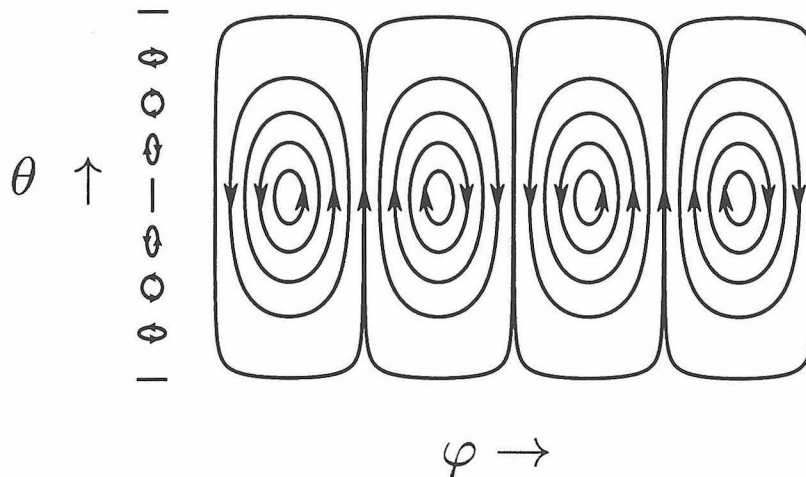
- The flow pattern is shown along with the small elliptical paths (on the left) of individual fluid elements. The flow pattern moves (to the left) past the fluid particles as the mode evolves.

Figure 1.5: **The r-mode patterns I (courtesy of Lee Lindblom).** R-modes are vorticity patterns which move relative to the star. All r-modes propagating counter to the star's rotation are CFS-unstable (Andersson 98).

Flow Pattern for the $m = 2$ r-mode

Polar View
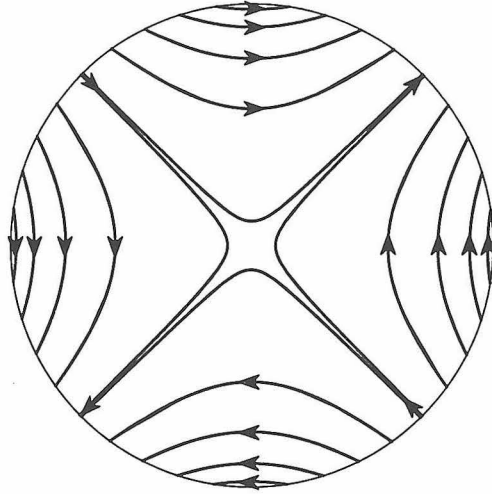
Equatorial View
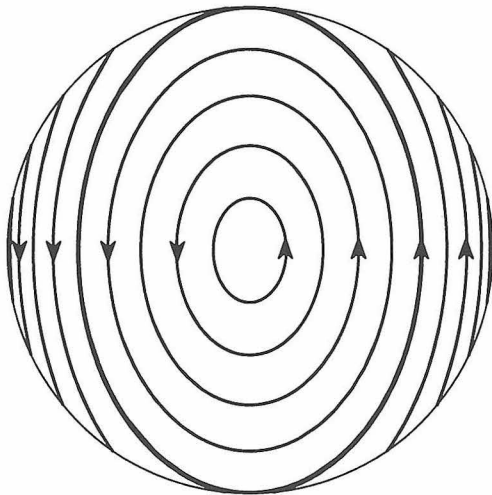
Figure 1.6: **The r-mode patterns II (courtesy of Lee Lindblom).**

related to the rotational frequency of the star f_0 by

$$f = \frac{(l-1)(l+2)}{l+1} f_0, \tag{1.34}$$

where l is the r-mode angular wave number. [In general, an r-mode's angular dependence is characterized by two integers, m and l. However, as Papaloizou and Pringle (1978) have shown, for barotropic stars only r-modes with $m = l$ can exist.]

R-modes couple to gravitational radiation predominantly through their current multipole moments, by contrast with f-modes, which couple to gravitational radiation through density multipole moments. The reason the r-mode instability is so strong is that the lowest-order r-mode ($l = m = 2$) satisfies the CFS criterion for instability; whereas typically only high-order ($l = m \geq 4$ or 5) f-modes are CFS unstable. (For low-order modes radiation-reaction is stronger and viscous damping is weaker, than for high-order modes).

1.3.2 R-modes in strongly accreting neutron stars.

Bildsten (1998) has conjectured that gravitational radiation could limit rotational frequencies of neutron stars in Low-Mass X-ray Binaries (LMXB's). This, Bildsten has argued, could explain why these neutron stars all have similar rotational frequencies, which do not seem to depend strongly on the rate of accretion. Bildsten's original idea was that the crust of an accreting neutron star could possess non-axisymmetric quadrupole moment which would emit gravitational waves; these waves would provide a gravitational-radiation reaction torque sufficient to compensate the accretional spin-up torque.

Andersson, Kokkotas and Stergioulas (1998), and Bildsten (1998) have idependently hypothesised that r-modes could also be the source of gravitational waves in the accreting neutron star, and that the r-mode instability may provide an alternative explanation for the observed narrow range of rotational frequencies of neutron stars in LMXB's. According to them, the r-mode instability would be triggered once the neutron star, which is spun up by accretion, reaches some critical frequency of rotation.

Then, they have argued, the star's r-modes would grow so that the gravitational-radiation reaction would compensate the accretional spin-up torque.

Whatever is the mechanism of the gravitational-wave emission, neutron stars in LMXB's could be a potentially detectable periodic source for LIGO-II, Bildsten and Andersson et al. have shown. One could then distinguish the r-mode gravitational waves from waves produced by frozen-in mass inhomogeneities, since they have different frequencies ($f_{quadrupole} = 2f_0$, whereas $f_{r-mode} = (4/3)f_0$ for the $l = m = 2$ r-mode).

In paper V we have investigated further the proposal that the r-mode instability is active in neutron stars in LMXB's. Our conclusions depend crucially on whether the dissipation of the r-mode decreases with temperature (as is the case, e.g., when shear viscosity dominates the r-mode damping), or instead is temperature-independent (as is the case when, e.g., the mutual friction of proton and neutron superfluids dominates the damping).

In the "temperature-dependent" case we found that the neutron star will undergo a few-million-year-long cycle of slow ($\sim 10^6$ years) spin-up—rapid (~ 1month) runaway heating—rapid (~ 1month) spin-down—slow ($\sim 10^5$ years) cooling.

We have shown that in this case it is very unlikely that any of the currently observed neutron stars in LMXBs in our galaxy are in the r-mode excited state of the cycle. The detection of gravitational radiation from extragalactic LMXBs in the r-mode excited state is also not likely, even with advanced LIGO interferometers.

H. Spruit (1998) has independently and simultaneously discovered the thermal runaway effect and argued that it will produce a gamma-ray burst of $1 - 8 \times 10^{51}$erg.

In the "temperature-independent" case, we find that a steady-state equilibrium is reached, in which both angular velocity and temperature are constant or are oscillating with periods of several hundreds of years. We make a robust prediction that this equilibrium neutron-star core temperature is around 4×10^8K. In this case the neutron stars are emitters of gravitational waves which could be detected by interferometers similar in sensitivity to LIGO-II, precisely in the way which was proposed by Bildsten and Andersson et al.

Therefore, paper V argues, if LIGO detects gravitational waves coming from a LMXB, which have the r-mode frequency, it will provide a strong experimental evidence for the superfluid nature of the neutron-star core.

Bibliography

[1] Andersson, N. 1998, ApJ, **502**, 708

[2] Andersson, N., Kokkotas, K. D. and Stergioulas, N. 1998, ApJ, in press [astro-ph/9806089]

[3] Barish, B *et al.* 1996, "LIGO advanced Research and Development Program Proposal," LIGO technical document LIGO-M970107-00-M

[4] Bildsten, L., ApJ, **501**, L89

[5] Bondu, F. and Vinet, J. Y. 1995, Phys. Lett. A, **198(2)**, 74

[6] Braginsky, V. B. and Khalili, F. Ya 1990, Phys. Lett. A, **147**, 251

[7] Braginsky, V. B. and Khalili, F. Ya 1992, Quantum Measurement (edited by K. S. Thorne, Cambridge University Press)

[8] Braginsky, V. B. and Khalili, F. Ya 1996, Phys. Lett. A, **218**, 167

[9] Braginsky, V. B., Gorodetsky, M. L. and Khalili, F. Ya 1997, Phys. Lett. A, **232**, 340

[10] Braginsky, V. B., Gorodetsky, M. L. and Khalili, F. Ya 1998, Phys. Lett. A, **246**, 485

[11] Chandrasekhar, S 1970, Phys. Rev. Lett., **24**, 611

[12] Callen, H. B. and Welton, T. A. 1951, Phys. Rev., **83**, 34

[13] Friedman, J. L. and Morsink, S. 1998, ApJ, **502**, 714

[14] Friedman, J. L. and Schutz, B. F. 1978, ApJ, **222**, 281

[15] Gillespie, A. and Raab, F. 1995, Phys. Rev. D, **52**, 577

[16] Gonzalez, G. I. and Saulson, P. R. 1994, J. Accoust. Soc. Am., **96**, 207

[17] Jaekel, M. T. and Reynaud, S. 1990, Europhys. Lett., **13**, 301

[18] Kimble, H. J. *et al.* 1999, work in progress

[19] Lindblom, L., Owen, B. J. and Morsink, S. 1998, Phys. Rev. Lett, **80**, 4843

[20] Milburn, G. J. and Walls, D. F. 1994, Quantum Optics (Springer)

[21] Papaloizou, J. and Pringle, J. E. 1978, MNRAS, **182**, 423

[22] Saulson, P. R. 1990, Phys. Rev. D, **42**, 2437

[23] Spruit, H. 1998, A&A, **341**, L1

[24] Unruh, W. 1982, in *Quantum Optics, Experimental Gravitation and Measurement theory*, eds. Pierre Meystre and Marlin O. Scully (Plenum, 1982), p. 647

[25] Vyatchanin, S. P. and Matsko, A. B. 1993, JETP, **77**, 218

[26] Vyatchanin, S. P. and Zubova, E. A. 1995, Phys. Lett. A, **201**, 269

[27] Vyatchanin, S. P. and Matsko, A. B. 1996, JETP, **82**, 1007

[28] Weiss, R. et al. 1998, "LSC White Paper on Detector Research and Development," LIGO document

Chapter 2   Towards QND measurements for LIGO

2.1 Paper I: Speed Meter as a Quantum Nondemolition Measuring Device for Force

Written with F. Ya. Khalili, published in Phys. Rev. D, **54**, 4725;

presented here with minor changes.

ABSTRACT

Braginsky has proposed a *speed meter* (a speed or momentum measuring device), consisting of a small Fabry-Perot cavity rigidly attached to a freely moving test mass. This paper devises an optical readout strategy which enables the meter, when monitoring a classical force via speed changes, to beat the standard quantum limit—at least in principle.

2.1.1 Introduction

A laser interferometer gravitational wave detector is, in essence, a device for monitoring a classical force (the gravitational wave) that acts on freely moving test masses (the interferometer's suspended mirrors). "Advanced" detectors, expected to operate in the LIGO/VIRGO interferometric network [1] in the middle or later part of the next decade, will be constrained by the *standard quantum limit* (SQL) for force measurements [2, 3],

$$\Delta F_{\text{SQL}} = \sqrt{\hbar m/\tau^3} \ . \tag{2.1}$$

Here $\hbar$ is Planck's constant, m is the mass of the test body on which the force acts, and τ is the duration of the force.

It is well known that the SQL is not an absolute barrier to further sensitivity improvements [2]. With cleverness, one can devise so-called *quantum nondemolition* (or QND) measurement schemes, which beat the SQL. Although fairly practical QND techniques have actually been devised for resonant-mass gravitational-wave detectors [4], no practical QND technique yet exists for the interferometric gravitational-wave detectors on which LIGO/VIRGO is based. The effort to devise such a technique is of great importance for the long-term future of the LIGO/VIRGO network.

Although a practical QND technique for such detectors is not yet known, several idealized techniques have been formulated [5] and are playing helpful roles in the

search for a practical technique. Most of these idealized techniques are based on optical measurements of a test mass's position. One, however, is based on measurements of the mass's speed or momentum. This "speed meter" has been devised in initial, conceptual form by Braginsky [6], and he has argued that it should be capable of beating the SQL.

The purpose of this paper is to demonstrate that, when coupled to a specific optical readout scheme that we have devised, Braginsky's speed meter does, indeed, beat the SQL, at least in principle.

2.1.2 The Basic Idea of the Speed Meter

The fundamental idea underlying Braginsky's speed meter is to attach a small, rigid Fabry-Perot cavity to the test mass, whose speed is to be measured. The cavity's two mirrors are to have identical transmissivities and negligible losses, in the idealized variant we shall analyze. This means that, when the cavity is at rest and is excited by laser light that is pricisely in resonance with one of the cavity's modes, the light passes straight through the cavity without reflection and emerges from the other side unchanged. When the cavity starts moving, by contrast, it sees the incoming light Doppler shifted; and, as a result, the light emerging from the other side gets phase shifted by an amount

$$\Delta\phi = \frac{\omega_o v \tau}{c} , \qquad (2.2)$$

where v is the cavity's speed, ω_o is its eigenfrequency, and τ is its ringdown time. Here and throughout we assume that $v \ll c/(\omega_o \tau)$.

By measuring the phase of the emerging light, one can infer the speed of the cavity without learning anything about its position. This absence of information about position implies (Braginsky has argued) that such a device should be able to evade any back-action force of the measurement on the cavity's velocity (or momentum), and therefore should be capable of beating the SQL.
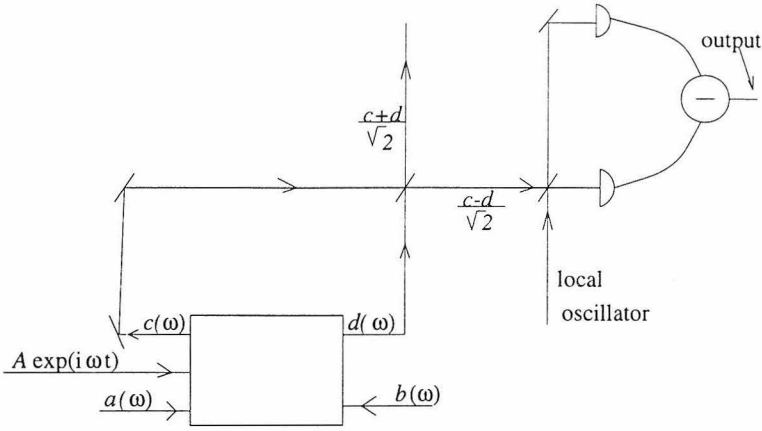
Figure 2.1: **Optical readout system for the QND speedmeter.**

2.1.3   Our Readout Scheme for the Speed Meter, and an Analysis of its Performance

In this section we shall exhibit an optical readout scheme for such a speed meter which does, indeed, enable it to beat the SQL. Our readout scheme is sketched in Fig. 2.1, whose details will become more clear in what follows.

Let

$$\psi_{in} = Ae^{-i\omega_0(t-x/c)} + \int_0^\infty d\omega \sqrt{\frac{\hbar\omega}{sc}} a(\omega)e^{-i\omega(t-x/c)} \tag{2.3}$$

be the incoming field on the left side of the cavity. The first term on the right-hand side of Eq. (2.3) represents classical pumping, and the second term shows quantum fluctuations of the incoming field; x is the position of the cavity and acquires time dependence when the cavity is moving; s is the area of the beam. Also $a(\omega)$, $b(\omega)$, $c(\omega)$ and $d(\omega)$ represent annihilation operators for four modes as in Fig. 2.1, and $t(\omega)$ and $r(\omega)$ represent frequency-dependent tranmission and reflection coefficients of the cavity respectively. In our set-up $t(\omega_0) = 1$, $r(\omega_0) = 0$.

Any motion of the cavity induces a time-dependence of x in Eq. (2.3), and hence with respect to the cavity the classical pump acquires frequencies different from ω_0. The resulting effect of the cavity motion is to scatter the classical part of the incoming wave into modes which would otherwise carry only vacuum fluctuations. A simple calculation produces the following relations:

$$
\begin{aligned}
c(\omega) &= t(\omega)a(\omega) + r(\omega)b(\omega) \\
&\quad + iA\frac{\omega_0}{c}\sqrt{\frac{sc}{\hbar\omega}}(t(\omega) - 1)\tilde{X}(\omega - \omega_0),
\end{aligned}
\tag{2.4}
$$

$$
\begin{aligned}
d(\omega) &= r(\omega)a(\omega) + t(\omega)b(\omega) \\
&\quad + iA\frac{\omega_0}{c}\sqrt{\frac{sc}{\hbar\omega}}r(\omega)\tilde{X}(\omega - \omega_0),
\end{aligned}
\tag{2.5}
$$

where $\tilde{X}(\Omega)$ is defined by

$$
x(t) = \int_{-\infty}^{\infty} \tilde{X}(\Omega)e^{-i\Omega t}d\Omega
\tag{2.6}
$$

We assume that the cavity is pushed by an external signal force $F_{\mathrm{s}}(t)$ (due, e.g., to a gravitational wave). Then its position obeys the free-mass equation of motion

$$
F = F_{\mathrm{s}} + F_{\mathrm{fl}} = m\ddot{x},
\tag{2.7}
$$

where F_{fl} stands for the random force produced by quantum fluctuations of the light. This force, as evaluated using momentum conservation, has the following Fourier transform

$$
\begin{aligned}
\tilde{F}_{\mathrm{fl}}(\Omega) &= \sqrt{\frac{W\hbar\omega_0}{2\pi c^2}}\left\{[1 - t(\omega_0 + \Omega)]\left[a(\omega_0 + \Omega) + a^\dagger(\omega_0 - \Omega)\right]\right. \\
&\qquad \left. - r(\omega_0 + \Omega)\left[b(\omega_0 + \Omega) + b^\dagger(\omega_0 - \Omega)\right]\right\}
\end{aligned}
\tag{2.8}
$$

for $\Omega \ll \omega_0$, where $W = scA^2/2\pi$ is the power of the incoming wave. Equation (2.8) can be simplified by noting that for the Fabry-Perot cavity $t + r = 1$, so the expression for the fluctuating force becomes

$$
\begin{aligned}
\tilde{F}_{\mathrm{fl}}(\Omega) &= \sqrt{\frac{W\hbar\omega_0}{2\pi c^2}}r(\omega_0 + \Omega)[a(\omega_0 + \Omega) - b(\omega_0 + \Omega) \\
&\qquad + a^\dagger(\omega_0 - \Omega) - b^\dagger(\omega_0 - \Omega)].
\end{aligned}
\tag{2.9}
$$

It is clear from Eq. (2.9) that $f(\omega) = [a(\omega) - b(\omega)]/\sqrt{2}$ is the only combination of the incoming modes which appears, multiplied by x, in the interaction part of the Hamiltonian . Therefore, all information about the motion of the cavity should be recorded in f and $f^\dagger$. The obvious suitable choice of readout is

$$e(\omega) = \frac{c(\omega) - d(\omega)}{\sqrt{2}}, \tag{2.10}$$

since, by putting Eqs. (2.6), (2.7), (2.9) into (2.10), we can express it as solely a function of f and the signal force:

$$
\begin{aligned}
e(\omega_0 + \Omega) = {}& [t(\omega_0 + \Omega) - r(\omega_0 + \Omega)]f(\omega_0 + \Omega) + \\
& 2i\frac{W\omega_0}{m\Omega^2 c^2}r(\omega_0 + \Omega)^2 \left[f(\omega_0 + \Omega) + f^\dagger(\omega_0 - \Omega)\right] \\
& + \sqrt{2}i\frac{\omega_0}{c}\sqrt{\frac{2\pi W}{\hbar\omega_0}}r(\omega_0 + \Omega)\frac{F_s(\Omega)}{m\Omega^2}.
\end{aligned}
\tag{2.11}
$$

It is attractive to read out $e(\omega)$ using homodyne detection as sketched in Fig. 2.1. The measurement output then is the homodyne quadrature

$$y(\Omega) = e(\omega_0 + \Omega)e^{i\psi(\Omega)} + e^\dagger(\omega_0 - \Omega)e^{-i\psi(\Omega)}, \tag{2.12}$$

where $\psi(\Omega)$ is a phase factor that we shall fix below so as to minimize the noise (see also [7]). Then the quantum noise spectral density in this measured quantity, as computed from the formula $\langle y(\Omega)y(\Omega')\rangle = S_y(\Omega)\delta(\Omega + \Omega')$, is

$$
\begin{aligned}
S_y(\Omega) = {}& 2\alpha^2(\Omega)\left\{1 - \cos\left[2\psi\left(\Omega\right)\right] - \right. \\
& \left. 2\alpha\left(\Omega\right)\sin\left[2\psi\left(\Omega\right)\right]\right\} + 1
\end{aligned}
\tag{2.13}
$$

where $\alpha(\Omega) = (2W\omega_0/m\Omega^2 c^2)|r(\omega_0 + \Omega)|^2$. This noise is minimized for

$$\tan 2\psi_{\text{min}}(\Omega) = \frac{1}{\alpha(\Omega)}. \tag{2.14}$$

Putting in explicitly $r(\Omega) = i\Omega\tau_{\text{ringdown}}/(1 + i\Omega\tau_{\text{ringdown}})$, we see that for large power

$W \gg mc^2/\omega_0\tau_{\mathrm{ringdown}}^2$ the minimum noise is

$$S_{\mathrm{y}} = \frac{1}{4\alpha(\Omega)^2} = \frac{m^2\Omega^4 c^4}{16W^2\omega_0^2|r(\omega_0 + \Omega)|^2}. \tag{2.15}$$

Here τ_{ringdown} is the e-folding time for resonant light to escape from the cavity. Now suppose that the form of the signal , $F_{\mathrm{s}}(\Omega)$, is known and we use an optimal filter to search in the output $y(\Omega)$ to see whether the signal is actually present. The signal to noise ratio for this search is given by

$$\frac{S}{N} = \frac{1}{2\pi}\int_{\Omega_1}^{\Omega_2} \frac{16\pi W\omega_0|r(\omega_0 + \Omega)|^2}{mc^2\Omega^2}\frac{|F_{\mathrm{s}}(\Omega)|^2}{\hbar m\Omega^2}d\Omega. \tag{2.16}$$

When the detection frequency is sufficiently small, i.e., when

$$\Omega \ll 1/\tau_{\mathrm{ringdown}}, \tag{2.17}$$

then $\psi(\Omega)$ is a constant ($\psi \to mc^2/4W\omega_0\tau_{\mathrm{ringdown}}^2$), which makes homodyne detection technically possible (see Fig. 2.1). The signal to noise ratio may then be higher than that limited by the SQL, provided that sufficiently large input power can be used:

$$\frac{S}{N} = \frac{W}{W_{\mathrm{SQL}}}\left(\frac{S}{N}\right)_{\mathrm{SQL}}, \tag{2.18}$$

where

$$\left(\frac{S}{N}\right)_{\mathrm{SQL}} = \frac{1}{\hbar m}\int \frac{|F_{\mathrm{s}}|^2}{\Omega^2}d\Omega \tag{2.19}$$

and

$$W_{\mathrm{SQL}} = \frac{mc^2}{16\pi\omega_0\tau_{\mathrm{ringdown}}^2}. \tag{2.20}$$

Thus the minimum detectible force may be lower than the Standard Quantum Limit by a factor of $\sqrt{W_{\mathrm{SQL}}/W}$:

$$F_{\min} = \sqrt{\frac{W_{\mathrm{SQL}}}{W}}\Delta F_{\mathrm{SQL}}. \tag{2.21}$$

If τ_{ringdown} is sufficiently small, then from Eq. (2.17) we see that one could perform a

broad-band QND measurement by using the frequency-independent homodyne phase.

Equation (2.20) obviously holds for a broad-band signal as well, but the expression for W_{SQL} is different and the homodyne phase acquires frequency dependence, which makes the detection very difficult.

2.1.4 Conclusion

We have considered a particular example of a speed meter, and have shown that using this speed meter one could in principle perform a broad-band QND measurement of an external force acting on the test mass. In particular, we have shown that, for the readout scheme of Fig. 2.1, the minimum measureable force $F_{\min}$ is given by

$$F_{\min} = \sqrt{\frac{W_{SQL}}{W}} \Delta F_{SQL} \,, \tag{2.22}$$

where ΔF_{SQL} is the standard quantum limit [Eq. (2.1)], W is the laser power, and W_{SQL} is the minimum laser power required for beating the SQL:

$$
\begin{aligned}
W_{SQL} &= \frac{mc^2}{16\pi\omega_o\tau^2} \\
&= 5 \times 10^4 \text{Watt} \frac{m}{10\text{kg}} \frac{4 \times 10^{15}\text{s}^{-1}}{\omega_o} \left(\frac{0.01\text{s}}{\tau}\right)^2
\end{aligned}
\tag{2.23}
$$

Although it is not outrageous to imagine achieving the laser powers $W > W_{SQL}$ at which Eq. (2.22) reports a beating of the SQL, there are many serious practical obstacles to implementing such a speed meter in a real interferometric gravitational-wave detector. Nevertheless, this speed meter might contain the conceptual seeds from which will grow a practical QND scheme for the LIGO/VIRGO network.

Acknowledgments

Bibliography

[1] A. Abramovici *et al.*, Science, **256**, 325 (1992); C. Bradaschia *et. al.*, Nucl. Instrum & Methods, **A289**, 518 (1990).

[2] See, e.g., V. B. Braginsky and F. Ya. Khalili, *Quantum Measurement* (Cambridge University Press, 1992).

[3] For a translation of this SQL into the corresponding limits on the sensitivities of LIGO/VIRGO interferometers, see, e.g., pp. 430–432 of K. S. Thorne, Chapter 9 of *300 Years of Gravitation*, eds. S. W. Hawking and W. Israel (Cambridge University Press, Cambridge, 1987).

[4] See, e.g., V. B. Braginsky, Yu. I. Vorontsov, and K. S. Thorne, *Science*, **209**, 547 (1988).

[5] W. G. Unruh, in *Quantum Optics, Experimental Gravitation and Measurement theory*, eds. Pierre Meystre and Marlin O. Scully (Plenum, 1982), p. 647; M. T. Jaekel, S. Reynaud, *Europhys. Lett.*, **13**, pp. 301-306 (1990) and S. P. Vyatchanin, E. A. Zubova, *Optics Communications*, **111**, 301-303 (1994).

[6] V. B. Braginsky, private communication, also V. B. Braginsky, F. Ya. Khalili, *Phys. Lett. A*, **147**, 251-256 (1990).

[7] S. P. Vyatchanin and A. B. Matsko, *JETP*, **77**, 218 (1993).

2.2 Paper II: QND and higher order effects for a nonlinear meter in an interferometric gravitational wave antenna

ABSTRACT

A new optical topology and signal readout strategy for a laser interferometer gravitational wave detector were proposed recently by Braginsky and Khalili. Their method is based on using a nonlinear medium inside a microwave oscillator to detect the gravitational-wave-induced spatial shift of the interferometer's standing optical wave. This paper proposes a quantum nondemolition (QND) scheme that could be realistically used for such a readout device and discusses a "fundamental" sensitivity limit imposed by a higher order optical effect.

2.2.1 Introduction and Summary

Laser interferometer gravitational wave detectors (LIGO, VIRGO, GEO 600, TAMA) are designed to detect small perturbations h in the spatial metric due to gravitational waves (GW) passing through the Earth [1] . Being very far from major astrophysical sources [2], these detectors are likely to encounter GW's that are very weak, so the detectors must be correspondingly sensitive—e.g., the first LIGO interferometer will be able to detect GW's with $h \sim 3 \times 10^{-21}$ in the frequency band of $30 - 300 \mathrm{Hz}$. Improving the sensitivity of measurement may be necessary to achieve the first GW detection and will surely be necessary to improve the event rate.

One of the major noise sources in traditional interferometers is the so-called shot noise. What is being detected is the phase shift of the output optical wave [1]:

$$\delta\phi \sim \omega_{\mathrm{opt}}\tau_{\mathrm{GW}}h \tag{2.24}$$

where ω_{opt} is the angular frequency of the optical wave and τ_{GW} is the half-period of a gravitational wave. For coherent optical pumping the uncertainty in the phase due to shot noise is given by $\Delta\phi = 1/\sqrt{N_{\mathrm{GW}}}$, where N_{GW} is the number of photons introduced into the interferometer during τ_{GW}. Thus a gravitational wave can be

detected if

$$N_{\mathrm{GW}} > N_{\min} \simeq \frac{1}{(h\omega_{\mathrm{opt}}\tau^*_{\mathrm{GW}})^2}. \tag{2.25}$$

Therefore, in order to increase the gravity–wave sensitivity of the interferometer, we have to increase the number of photons in the resonator (and hence the consumed laser power) as $N \propto 1/h^2$. On the other hand, the presence of the large number of optical photons in the resonator poses severe technical and fundamental problems. Among the technical problems are distortion of mirrors due to overheating, and large laser power consumption [1]. The fundamental problem is that photons in the interferometer will randomly buffet the mirrors inducing random motion indistinguishable from the motion produced by a gravitational wave. Balancing this radiation pressure noise and the shot noise produces the Standard Quantum Limit (SQL) for monitoring the displacements of the test masses [2].

Recently Braginsky and Khalili have proposed a new way to improve the sensitivity of an interferometric GW detector without increasing the interferometer's optical power [3]. Their method entails a new type of GW readout based on a microwave oscillator containing an optically nonlinear medium, which is placed inside the GW detector's high quality Fabry-Perot resonator. The advantage of this readout method is that, unlike conventional interferometers, it does not require large optical power circulating inside the FP resonator in order to achieve high sensitivity. In section 2.2.2 the principles of this scheme are briefly outlined and some numerical estimates are quoted.

Section 2.2.3 describes a potentially practical Quantum Nondemolition (QND) strategy which can be used in the Braginsky–Khalili readout system (BK-meter). We show in Sec. 2.2.3 and Appendix A [cf. Eq. (2.44)] that a QND measurement can be performed within a narrow frequency band centered around

$$\Omega_0 = \sqrt{\frac{6\hbar N}{mcL}}\omega_{\mathrm{opt}}, \tag{2.26}$$

where ω_{opt} and N are the frequency of light and the number of photons stored in

the FP resonator respectively, L is the distance between the end mirrors of the FP resonator and m is the mass of each of the test masses to which the mirrors are attached. For $N = 2.8 \times 10^{20}$, $L = 4$km, $m = 10$kg, $\omega_{\text{opt}} = 3 \times 10^{15}$ one obtains $\Omega_0/2\pi = 60$Hz, which is within LIGO band. For the resonator's relaxation time of 10 seconds (as assumed in [3]), the necessary laser power to achieve this number of photons inside the resonator is ~ 9Watt.

We demonstrate in Appendix B that the bandwidth $\Delta\Omega$ of this measurement determines the optimal power input to the microwave oscillator:

$$W_{\text{optimal}} \sim W_{\text{SQL}} \frac{\Omega_0}{\Delta\Omega}, \tag{2.27}$$

where W_{SQL} is the power input necessary to achieve the Standard Quantum Limit sensitivity at frequency Ω_0; cf. Eq. (2.47) where the expression and the numerical estimate for W_{SQL} are given. The signal-to-noise ratio achieved by this QND measurement is greater by a factor of $\sqrt{\Omega_0/\Delta\Omega}$ than the SQL:

$$\left(\frac{S}{N}\right)_{\text{QND}} \sim \sqrt{\frac{\Omega_0}{\Delta\Omega}} \left(\frac{S}{N}\right)_{\text{SQL}}. \tag{2.28}$$

Section 4 and Appendix C discuss a higher-order optical effect in the BK readout system and derive the sensitivity limit that it imposes. In particular, thermally excited mechanical modes in the test masses will, after interacting with light inside the FP resonator, produce a "double conversion" of photons, which will be registered as noise by the detector; cf. Eq. (2.48) and Eq. (2.49).

2.2.2 Principle of operation of the BK meter

The layout of the BK meter is shown in Fig. 2.2 (for more detail the reader is referred to [3]). Three freely suspended mirrors—A,B and C—form walls of an L-shaped Fabry-Perot (FP) resonator which supports a standing optical wave, driven by a laser at end A or C. Section A-B of the resonator would be in one arm of the LIGO (or other) vacuum system, and B-C in the other. The block D containing two thin slabs

of non-linear medium (Fig. 2.3) is sandwiched between two thin focusing lenses two focal lengths apart. The lenses and the block are attached to mirror B. When the polarization tensor of a gravitational wave is aligned with the arms of the FP resonator, the distances between A and B and between B and C will change in counterphase– i.e., when one is increasing, the other one will decrease. This will produce the net spatial shift of the standing optical wave with respect to mirror B, thus changing the amplitude of the optical field within the two slabs of nonlinear medium. The slabs have cubic nonlinearities that are equal in magnitude but opposite in sign. They are positioned symmetrically with respect to the crest of the standing optical wave as shown in Fig. 2.3. Block D, which contains the slabs, is placed in between the plates of a capacitor which in turn is part of a microwave oscillator.

The spatial shift in the optical standing wave produces changes of electric field in the first and second slabs that are equal in magnitude and opposite in sign:

$$\delta E_1 = -\delta E_2. \tag{2.29}$$

Since the two slabs have the opposite nonlinearities, $\chi_1^{(3)} = -\chi_2^{(3)}$, the change in the index of refraction is the same for both of them:

$$\delta n_1 = \delta n_2 = 4\pi\chi_1^{(3)} E_1 \delta E_1. \tag{2.30}$$

This change in dielectric constants of the plates in turn changes the value of the microwave oscillator's capacitance, thus producing a shift in its resonant frequency:

$$\delta\omega_e = \frac{K\omega_{\text{opt}}}{2} h \tag{2.31}$$

where ω_e is the frequency of the microwave oscillator, ω_{opt} is the frequency of the optical wave, and $K = 16\pi^2\chi^{(3)} lN\hbar\omega_{\text{opt}}\omega_e/Vc$. Here l is the width of each of the nonlinear slabs and V is the volume of the capacitor. This shift is seen as a phase
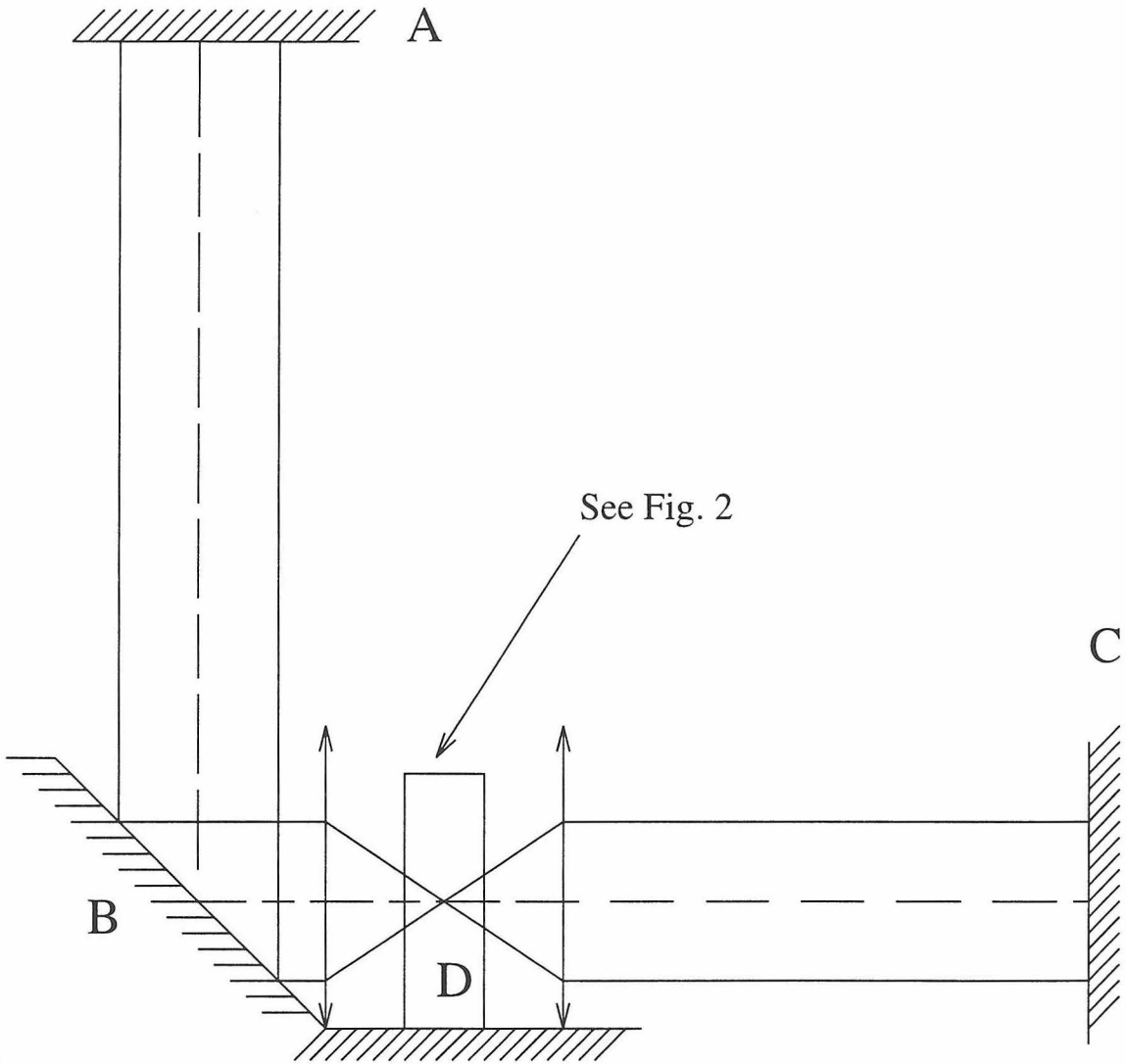
Figure 2.2: **The Braginsky-Khalili readout system.**
Two thin lenses focus light on block D containing nonlinear medium. Block D is shown on Fig. 2.3.
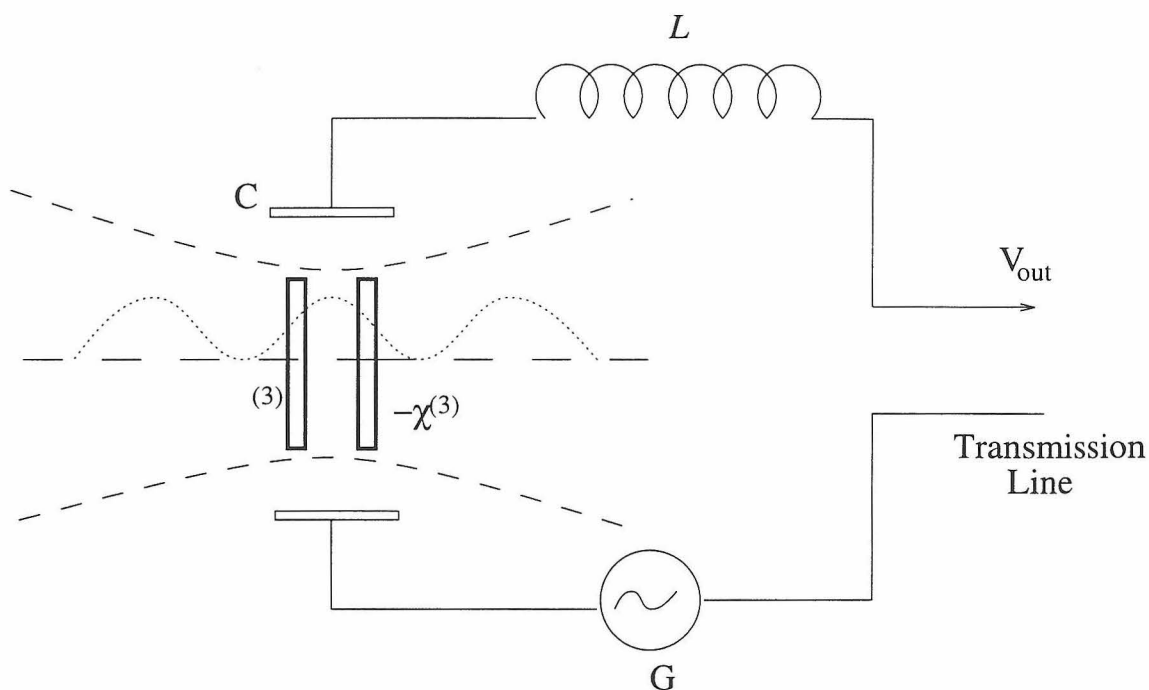
Figure 2.3: **Nonlinear readout device.**
This is an enlarged view of block D from Fig. 2.2. Two slabs of nonlinear medium are positioned at the points of maximal gradient of the intensity of the optical standing wave. The spacial shift of the optical standing wave changes the resonant frequency of the microwave LC oscillator.

shift in the readout of the microwave oscillator:

$$\delta\phi = \delta\omega_{\mathrm{e}}\tau_{\mathrm{e}}^* = \frac{1}{2}K\omega_{\mathrm{opt}}\tau_{\mathrm{e}}^*h, \tag{2.32}$$

where τ_{e}^* is the oscillator's ringdown time.

Braginsky and Khalili compare this with the traditional optical readout schemes in which the phase shift of the recombined optical wave is detected:

$$\delta\phi_{\mathrm{opt}} = \omega_{\mathrm{opt}}\tau_o^*h, \tag{2.33}$$

where τ_o^* is the ringdown time of the two traditional FP resonators, one in each arm of the interferometer. For $\chi^{(3)} = 10^{-14}\mathrm{cm}^2/\mathrm{Volt}^2$ (fused silica), $E_{\mathrm{opt}}^2 = 10^7\mathrm{Volt}^2/\mathrm{cm}^2$ (optical breakdown of fused silica), they calculate K in Eq. (2.31) to be of order 1, so for $\tau_{\mathrm{opt}}^* \sim \tau_{\mathrm{e}}^*$ the responses of both systems in terms of phaseshift are of the same order,

$$\phi_{\mathrm{opt}} \sim \phi_{\mathrm{e}}. \tag{2.34}$$

For coherent pumping in both cases the uncertainty in the phase is $\Delta\phi \sim 1/\sqrt{N_{\mathrm{GW}}}$, where N_{GW} is the number of photons (optical in conventional interferometers and microwave in the BK readout system) introduced into the interferometer during an averaging time (half the GW period). So to achieve the same level of sensitivity, one needs to pump the same number of photons in both cases, but the power needed by the BK meter is smaller by a factor of $\omega_{\mathrm{opt}}/\omega_{\mathrm{e}} \sim 10^4$. The BK estimate for the microwave power is

$$W_{\mathrm{e}} = \frac{\hbar\omega_{\mathrm{e}}N_{\mathrm{e}}}{\tau_{\mathrm{e}}^*} \sim 1\mathrm{Watt} \tag{2.35}$$

for $N_{\mathrm{e}} \sim 10^{20}$. For more detailed estimates the reader is refered to Ref.[3] .

2.2.3   QND for the BK readout system

Any readout system that monitors the displacement of the mirrors must exert on them a fluctuating back action force, thus enforcing the Heisenberg uncertainty relation.

As a consequence of this, all straightforward displacement measurements run into the Standard Quantum Limit (SQL) [4], [5]

$$\Delta x_{\mathrm{SQL}} = \sqrt{\frac{\hbar\tau}{m}}, \tag{2.36}$$

where Δx is the minimal uncertainty in displacement of a free mass m monitored over a time interval τ. This SQL for displacement can also be written in terms of the limiting spectral density of the mirrors' displacement fluctuations[4]:

$$S_x^{\mathrm{SQL}}(\Omega) = \frac{\hbar}{m\Omega^2} \tag{2.37}$$

where Ω is the frequency. Then $\Delta x = \sqrt{S_x^{\mathrm{SQL}}\Delta\Omega}$, and for $\Omega \sim \Delta\Omega \sim 1/\tau$ one recovers Eq. (2.36)

The SQL for a free mass is by no means a fundamental limit; it can be overcome by a variety of techniques [6] which are known collectively as Quantum Nondemolition (QND) measurements. All previously proposed QND schemes that are applicable for conventional GW interferometers utilize highly non-classical states of light, and none of them are practical because of technical difficulties (most especially because of the large required optical pumping power and because losses so easily destroy the non-classical states of light). In this paper a different strategy is proposed, one which does not require the deliberate creation or detection of any non-classical state of light and thus can be more practically implemented. This scheme, however, is confined to narrow-band measurements.

We begin by describing the backaction mechanism by which the BK readout system enforces the Heisenberg Uncertainty relation on the measurement of the test-mass position. The quantum state of the BK microwave oscillator satisfies the usual phase-number uncertainty relation

$$\Delta\phi_e \Delta N_e > \frac{1}{2}. \tag{2.38}$$

The more accurately the BK-meter reads out ϕ_e, the larger will be the fluctuations ΔN_e in the oscillator's number of microwave photons. The $\chi^{(3)}$ nonlinearity will

transform ΔN_e into an uncertainty of the optical index of refraction of the slabs:

$$\delta n_1 = -\delta n_2 = \frac{16\pi^2 \chi^{(3)} \hbar}{\epsilon V} \delta N_e, \tag{2.39}$$

where δN_e is the fluctuation in N_e, δn_1 and δn_2 are the resulting fluctuations in n_1 and n_2, ϵ is the coefficient of dielectric permitivity and V is the volume of the capacitor. Braginsky and Khalili have argued[3] that δn_1 and δn_2 cause a redistribution of the optical energy between the left and the right parts of the FP resonator, thereby giving rise to a net difference in the forces buffeting the mirrors:

$$\delta F = K \frac{\omega_{\text{opt}}}{\omega_e} \frac{\hbar \delta N_e}{L}, \tag{2.40}$$

where L is the total length of the FP resonator. This fluctuating force will cause fluctuations in the positions of the mirrors, thus causing fluctuations in the spatial shift of the optical field with respect to the mirror B and the nonlinear slabs attached to it:

$$\delta \tilde{x}(\Omega) = -\frac{3}{2} \frac{\delta \tilde{F}(\Omega)}{m\Omega^2} = -\frac{3}{2} K \frac{\omega_{\text{opt}}}{\omega_e} \frac{\hbar}{L} \delta \tilde{N}_e(\Omega), \tag{2.41}$$

where $\delta \tilde{x}(\Omega)$, $\delta \tilde{F}(\Omega)$ and $\delta \tilde{N}_e(\Omega)$ are Fourier components of the corresponding quantities, m is the mass of each of the mirrors, and the factor $\frac{3}{2}$ comes about when motion of all three mirrors is taken into account.

Now we are ready to describe our QND method, but first the following simple remark must be made. Suppose for a moment that all of the mirrors are rigidly fixed. As already mentioned above, fluctuations in N_e, by changing the optical coefficient of refraction of the slabs [Eq. (2.39)], will redistribute optical energy between the left and right parts of the FP resonator. A straightforward calculation [Eq. (2.66) in Appendix A] shows that this alone will change the optical field inside the nonlinear slabs so that

$$\delta E_1 = -\delta E_2 = E_0 \frac{n\omega_{\text{opt}} l}{c\sqrt{2}} \delta n, \tag{2.42}$$

thereby simulating a spatial shift of the optical field as in Eq. (2.29). Here l is the

width of the nonlinear slab, $n \equiv n_1 = n_2$, $\delta n \equiv \delta n_1 = -\delta n_2$ and E_0 is the peak amplitude of the optical standing wave inside the FP resonator.

Now if we release the mirrors, the back action (2.41) will affect our reading as well, and the total fluctuations of the optical field inside the nonlinear slabs will be given by

$$
\begin{aligned}
\delta \tilde{E}_1(\Omega) \quad - \quad & \delta \tilde{E}_2(\Omega) = \\
= \quad & \sqrt{2} n E_0 \frac{\omega_{\text{opt}} l}{c} \left(1 - 6 \frac{\omega_{\text{opt}}^2}{\Omega^2} \frac{\hbar N}{mc^2 \tau} \right) \delta n(\Omega)
\end{aligned}
\tag{2.43}
$$

where $\tau = L/c$; cf. Eq. (2.67) of Appendix A. From the above equation we see that for a given frequency $\Omega = \Omega_0$ we can adjust N in such a way that $\delta \tilde{E}_1(\Omega) = \delta \tilde{E}_2(\Omega) = 0$ and thus the readout system does not register any fluctuations due to the back action (but only for that value of Ω). Thus a QND measurement is performed. The relationship between the QND angular frequency Ω_0 and the number N of optical photons in the Fabry-Perot resonator is

$$
\Omega_0 = \sqrt{\frac{6\hbar N}{mcL}} \omega_{\text{opt}};
\tag{2.44}
$$

see Eq. (2.26).

The essential reason that this readout is QND is that it registers not only the fluctuations of the mirrors' displacement x due to backaction [the second term in large parentheses in Eq. (17)], but also directly the back-action force (the first term). Thus a position-momentum correlation is introduced into the measurement procedure, and such correlations are known to make QND possible[4]. For $L = 4$km, $\Omega/2\pi = 60$Hz, $\omega_{\text{opt}} = 3 \times 10^{15} \text{s}^{-1}$, and $m = 10$kg the necessary number of optical photons to perform QND is

$$
N = \frac{1}{6} \frac{\Omega_0^2}{\omega_{\text{opt}}^2} \frac{mc^2 \tau}{\hbar} \sim 2.8 \times 10^{20}.
\tag{2.45}
$$

The QND measurement described above is clearly narrowband. In principle one can dynamically tune the frequency at which the QND is performed by changing the laser power and thus changing the number of optical photons N in the resonator, provided

that the frequency of the signal changes slowly compared to the ring-down rate of the optical resonator. In practice the issues of fluctuations in N and stability of control systems may be a serious abstacle for such dynamical tuning. Analysis of these and other practical difficulties is beyond the scope of the present work.

Appendix B considers a particular scheme for measuring of the phase of the microwave oscillator. In this scheme the oscillator is coupled to a transmission line, and the physically measured quantity is the phase quadrature of the outgoing electromagnetic wave propagating along the transmission line. Having specified fully the measurement model, we find that if the bandwidth of measurement is $\Delta\Omega$ then the signal-to-noise ratio for the narrow-band QND measurement can be as high as

$$
\begin{aligned}
\left(\frac{S}{N}\right)^2_{\text{QND}} &\sim \left(\frac{S}{N}\right)^2_{\text{SQL}} \frac{\Omega_0}{\Delta\Omega} \\
&= \frac{1}{2\pi} \frac{\Omega_0}{\Delta\Omega} \int_{\Omega_0-\Delta\Omega}^{\Omega_0+\Delta\Omega} \frac{m\Omega^2 L^2 |h(\tilde{\Omega})|^2}{\hbar} d\Omega.
\end{aligned}
\tag{2.46}
$$

The above signal-to-noise ratio is achieved when the pumping power of the microwave oscillator is given by

$$
\begin{aligned}
W_{\text{optimal}} &= \frac{V^2}{32\pi^2 \chi^{(3)2} N\tau} \left(\frac{\Omega_0}{\omega_{\text{opt}}}\right)^2 \left(\frac{L}{l}\right)^2 \frac{1}{\hbar\omega_e} \frac{\Omega_0}{\Delta\Omega} \\
&= W_{\text{SQL}} \frac{\Omega_0}{\Delta\Omega},
\end{aligned}
\tag{2.47}
$$

where V is the volume of the capacitor and W_{SQL} is the minimal power necessary to achieve the SQL sensitivity level; cf. Eq. (2.80) of Appendix B and Eq. (2.27) of the introduction. For $V = (.01\text{mm})^3$, $\omega_e = 10^{11}\text{s}^{-1}$ and for other parameters having numerical values as in Eq. (2.45), we get $W_{\text{optimal}} = 0.1\text{Watt}\,(\Omega_0/\Delta\Omega)$ (cf. the 1kW of the optical power required to achieve the SQL in a conventional interferometric scheme).

While we have not devised a general proof, it seems likely that no other microwave readout scheme can operate with a power less than in Eq. (2.47); expression (2.47) is probably a general relation for optimally disigned microwave readout schemes.

2.2.4 Higher-order optical effects; fundamental sensitivity limit

In this section we identify and discuss a fundamental limit on the sensitivity of the BK readout system—a limit that applies whether or not the system is being operated in a QND mode.

In an interferometric GW detector, mirrors are installed on the surfaces of test masses, which have internal elastic mechanical modes of frequencies $\Omega_m/2\pi \geq 12$ kHz. The noise curve of the interferometer will have large peaks near these frequencies. When photons of frequency $\omega_{\rm opt}$ interact with walls oscillating with the frequancy Ω_m, some of the photons will be up or down converted to frequencies $\omega_{\rm opt} \pm \Omega_m$. These up or down converted photons in turn interact with the "noisy" walls, and if there is a non-zero component of the mirrors' motion at $\Omega_m \pm \Omega$, then some of the photons will up or down convert a second time to frequencies $\omega_0 \pm \Omega$. If Ω is the frequency of detection, then this second-order process of double frequency conversion will be registered by the BK readout system as a signal from a gravitational wave.

The perturbation theory for FP resonators with moving walls is worked out in detail in Appendix C. Here just the main result is quoted. From Eq. (2.107) the noise curve in units of $1/\sqrt{\rm Hz}$ is given by

$$\sqrt{S_h(\Omega)} \sim \frac{1}{3\pi} \frac{\omega_{\rm opt} k_B T_e \sqrt{\gamma_m}}{m L \Omega_m^2 \Omega^2 \tau c} \sqrt{\Omega\tau + \epsilon} \tag{2.48}$$

where T_e is the temperature of the test masses, γ_m is the damping rate of their mechanical modes, and $\epsilon \sim \max\left(\delta\chi^{(3)}/\chi^{(3)}, \delta l/\lambda\right)$. Here $\delta\chi \equiv \chi_1^{(3)} + \chi_2^{(3)}$, $\chi^{(3)} \equiv \chi_1^{(3)}$, λ is the wavelength of light in the resonator and δl is the spatial offset of the slabs from the position in shown Fig. 2. For $L = 4$ km, $\Omega = 60$rad/sec, $T_e = 300$K, $\Omega_m = 7.2 \times 10^4$rad/sec, $m = 10$kg and $\gamma_m = 10^{-8}\Omega_m$ we get the noise level of

$$\sqrt{S_h} \sim 10^{-28}\sqrt{(\Omega\tau + \epsilon)}/\sqrt{\rm Hz} \tag{2.49}$$

It is not unimaginable that future interferometers will achieve sensitivities $\sqrt{S_h} \sim$

$10^{-29}/\sqrt{\text{Hz}}$ for low frequency $(10 - 100\text{Hz})$ narrow band signals (by, e.g., using the QND technique described in this paper). In this case, Eqs. (2.48) and (2.49) show that higher order effects will give rise to a "fundamental" low frequency noise limit of magnitude

$$\sqrt{S_h(\Omega)} \sim 10^{-28} \left(\frac{60\text{rad/s}}{\Omega} \right)^2 / \sqrt{\text{Hz}}. \tag{2.50}$$

2.2.5 Conclusions

In this paper we have shown that a practical QND measurement might be possible for a narrow-band measurement by a gravitational wave interferometer using a BK readout system. Also it was shown that second-order effects set a "fundumental" limit on the precision of the measurement.

Acknowledgements

2.2.6 Appendix A: physics of the nonlinear medium inside the BK Fabry-Perot resonator

First consider one slab of nonlinear medium positioned inside a FP resonator. Let x_1 (Fig. 2.4) be the total path length from the left mirror to the left edge of the slab, x_3 be the path length from the right mirror to the right edge of the slab and l be the width of the slab. For simplicity of the calculation, we assume $l \ll \lambda$ where λ is the wavelength of light in the resonator. Also for convenience define $\tau_1 = x_1/c$, $\tau_2 = l/c$, $\tau_3 = x_3/c$. The eigenfrequencies ω of this optical resonator were worked out in [3]. They satisfy the following eigenequation:

$$\sin(\omega\tau) = (n-1)\sin(n\omega\tau_2) \times$$
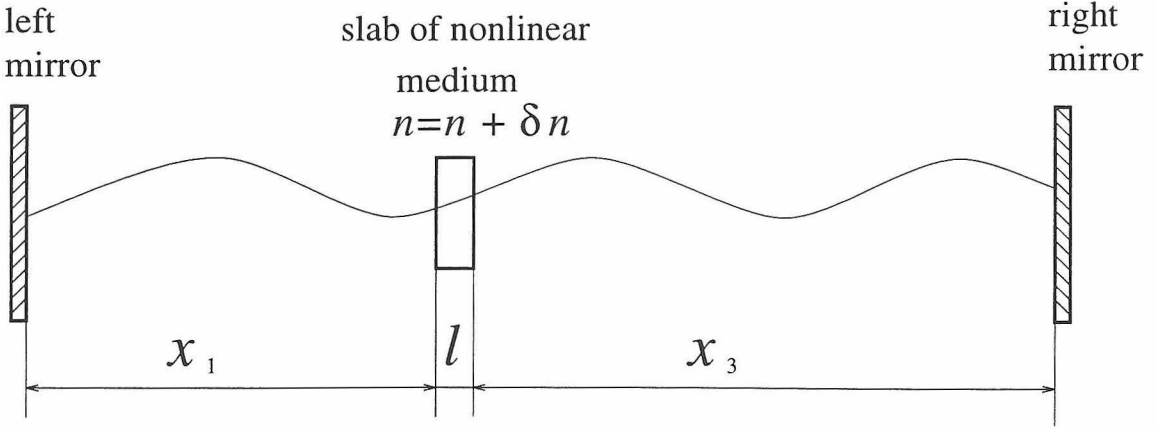
Figure 2.4: **Thin slab of nonlinear medium inside a Fabry-Perot resonator.** The changing index of refraction of the slab will redistribute optical energy between the left and the right parts of the resonator.

$$\left[\sin\left(\omega\tau_1\right)\sin\left(\omega\tau_3\right) + \frac{1}{n}\cos\left(\omega\tau_1\right)\cos\left(\omega\tau_3\right)\right] \tag{2.51}$$

where $\tau = \tau_1 + \tau_3 + n\tau_2$. This equation has approximate solutions

$$\omega = \omega_0 + (n^2 - 1)\omega_0\frac{\tau_2}{2\tau}\left\{\cos\left[\omega_0\left(\tau_1 - \tau_3\right)\right] - 1\right\} \tag{2.52}$$

where $\omega_0 = \pi k/\tau$, and k is any integer. When the slab's index of refraction n changes, ω changes accordingly:

$$\frac{d\omega}{dn} = \frac{n\omega^0\tau_2}{\tau}\left\{\cos\left[\omega^0\left(\tau_1 - \tau_3\right)\right] - 1\right\} \tag{2.53}$$

The total optical energy contained in the resonator is

$$U = N\hbar\omega \tag{2.54}$$

where N is the number of optical photons. We can find all of the forces acting on the mirrors by taking derivatives of U with respect to τ_1 and τ_3. For example,

$$F_{\text{left}} = -\frac{N\hbar}{c}\frac{\partial\omega}{\partial\tau_1} \tag{2.55}$$

and

$$F_{\text{right}} = -\frac{N\hbar}{c}\frac{\partial\omega}{\partial\tau_3} \tag{2.56}$$

where F_{left} and F_{right} are the forces acting on the left and the right mirrors respectively, with the positive direction being out of the resonator. When taking derivatives of ω, one has to keep in mind that ω_0 also depends on τ_1 and τ_3.

The force acting on the slab of nonlinear medium is $F_{\text{left}} - F_{\text{right}}$. The total spatial shift of the optical wave with respect to the slab due to the forces acting on the end mirrors and the slab itself is

$$\delta\tilde{x}(\Omega) = -\frac{3}{2m\Omega^2}\left[\tilde{F}_{\text{left}}(\Omega) - \tilde{F}_{\text{right}}(\Omega)\right], \tag{2.57}$$

where "tildas" stand for Fourier Transforms. If F_{left} and F_{right} are produced by a fluctuating index of refraction $n = n_0 + \delta n$, then on substituting Eqs. (2.55) and (2.56) into Eq. (2.57) we get

$$\delta\tilde{x}(\Omega) = \frac{3N\hbar}{2m\Omega^2}\left(\frac{\partial}{\partial\tau_1} - \frac{\partial}{\partial\tau_3}\right)\frac{d\omega}{dn}\delta\tilde{n}(\Omega). \tag{2.58}$$

By then putting Eqs. (2.53) and (2.58) together we obtain

$$\delta\tilde{x}(\Omega) = -\frac{3N\hbar n}{mc}\frac{\omega^2}{\Omega^2}\frac{\tau_2}{\tau}\sin\left[\omega\left(\tau_1 - \tau_3\right)\right]\delta\tilde{n}(\Omega). \tag{2.59}$$

For the two slabs of opposite nonlinearities ($\delta n_1 = -\delta n_2 = \delta n$) in the configuration of Fig. 2.2, their two contributions add up to give

$$\delta\tilde{x}(\Omega) = -6\frac{Nn\hbar}{mc}\frac{\omega^2}{\Omega^2}\frac{\tau_2}{\tau}\delta\tilde{n}(\Omega). \tag{2.60}$$

The above expression is a manifestation of the back action as explained in Sec. II.

Now let the amplitude of the optical electric field in the left part of the resonator be

$$E_{\text{left}} = E_0\sin\left(\frac{\omega x}{c}\right) \tag{2.61}$$

where x is the spatial coordinate with the origin at the left wall. Then the field in the middle of the left slab is given by

$$
\begin{aligned}
E_1 &= E_0 \left[\sin(\omega\tau_1) + \frac{1}{n}\cos(\omega\tau_1)\sin\left(\frac{n\omega\tau_2}{2}\right) \right] \\
&+ O\left[(\omega\tau_2)^2\right].
\end{aligned}
\tag{2.62}
$$

Now

$$
\frac{dE_1}{dn} \simeq \frac{dE_0}{dn}\sin(\omega\tau_1) + E_0\tau_1\cos(\omega\tau_1)\frac{d\omega}{dn}.
\tag{2.63}
$$

In the case when two slabs are present inside the FP resonator, their contributions to the frequency and field changes add up linearly (since the perturbations are very small). For the configuration of Fig. 2.2 we see from Eq.(2.53) that $d\omega/dn = 0$, so

$$
\frac{dE_1}{dn} = \frac{dE_0}{dn}\sin(\omega\tau_1).
\tag{2.64}
$$

But $F_{\text{left}} \propto E_0^2$, so

$$
\frac{dE_0/dn}{E_0} = \frac{1}{2}\frac{dF_{\text{left}}/dn}{F_{\text{left}}} = -\frac{\tau}{\omega}\frac{d}{dn}\frac{\partial\omega}{\partial\tau_1}.
\tag{2.65}
$$

Putting Eq. (2.53) and Eq. (2.64) into Eq. (2.65) and doing exactly the same calculation for the second slab, we obtain

$$
\delta E_1 = -\delta E_2 = E_0\frac{n\omega_{\text{opt}}l}{\sqrt{2}c}\delta n
\tag{2.66}
$$

for the case when mirror B is in the middle of the resonator. Combining this with the back action from Eq. (2.60), we finally get Eq. (2.43) of Sec. 2.3:

$$
\begin{aligned}
\delta\tilde{E}_1(\Omega) &- \delta\tilde{E}_2(\Omega) = \\
&= \sqrt{2}nE_0\frac{\omega_{\text{opt}}l}{c}\left(1 - 6\frac{\omega_{\text{opt}}^2}{\Omega^2}\frac{\hbar N}{mc^2\tau}\right)\delta n(\Omega).
\end{aligned}
\tag{2.67}
$$

.

2.2.7 Appendix B: Calculation of optimal microwave power and signal-to-noise ratio for a QND measurement

Consider the microwave oscillator as shown on Fig. 2.3. In order to get information about the phase of the oscillator, we have to couple it to the outside world. Whatever the nature of this coupling is, it will cause dissipation of the induced oscillations and hence, by the fluctuation-dissipation theorem, give birth to a fluctuating component of the oscillator's current.

For concreteness, we model this coupling by an open transmission line of impedance R. We assume that the oscillator, consisting of the capacitor C and inductor $\mathcal{L}$, is driven on resonance by a generator G with a voltage output of amplitude V_0 (see Fig. 2.3). We also assume the transmission line encompasses all of the dissipation present in the oscillator, i.e., more generally, that we can access all of the information escaping from the oscillator. And finally, we set the temperature of the outside world to 0 (in reality, one will have to cool the oscillator to temperatures below the ones corresponding to a microwave frequency). The ingoing vacuum modes drive fluctuations in the circuit as described above, and the phase of the outgoing wave contains information about the phase of the oscillator.

The ingoing modes are described by the positive frequency part of a voltage operator

$$V_{\text{in}} = \int_0^\infty d\omega \sqrt{R\hbar\omega} a_{\text{in}}(\omega)e^{-\imath\omega t}, \tag{2.68}$$

where $a_{\text{in}}(\omega)$ is the annihilation operator for the ingoing mode of frequency ω normalized so that $\langle 0|a_{\text{in}}(\omega)a_{\text{in}}^\dagger(\omega')|0\rangle = \delta(\omega - \omega')$. Then the fourier component of the outgoing wave is

$$
\begin{aligned}
V_{\text{out}}(\omega_e + \Omega) &= \sqrt{R\hbar\omega_e}\frac{\alpha + \imath\Omega}{\alpha - \imath\Omega}a_{\text{in}}(\omega_e + \Omega) \\
&+ \frac{V_0\delta\omega_e(\Omega)}{2\Omega + \imath\alpha},
\end{aligned}
\tag{2.69}
$$

where $\alpha = R/\mathcal{L}$ is the ringdown rate of the microwave oscillator and $\delta\omega_e$ is the variation in the oscillator's resonant frequency due to fluctuating optical fields in the

slabs of nonlinear medium, as explained in Sec. 2.2.2:

$$\delta\omega_e = \frac{8\pi^2\chi^{(3)}lN\hbar\omega_{\text{opt}}\omega_e}{\sqrt{2}VL}\frac{\delta E_1 - \delta E_2}{E_0}.$$ (2.70)

Here V is the volume of the capacitor. The change of the optical field inside the slabs is given by

$$\begin{aligned}
\delta E_1(\Omega) - \delta E_2(\Omega) &= \sqrt{2}E_0 n\omega_{\text{opt}}\tau_2\left(1 - 6\frac{N\hbar}{mc^2\tau}\frac{\omega_{\text{opt}}^2}{\Omega^2}\right)\delta n(\Omega) \\
&\quad + \sqrt{2}E_0\frac{\omega_{\text{opt}}}{c}x_{\text{s}}(\Omega),
\end{aligned}$$ (2.71)

where the first term on the right-hand side is due to the fluctuating index of refraction of the slabs [cf. Eq. (2.43) of Sec. 2.2.3 and discussion therein], and the second term is due to the GW-induced relative displacement x_s of the slabs with respect to the standing optical wave. The fluctuations δn of the indices of refraction of the nonlinear slabs in the above expression are caused by the voltage fluctuations on the plates of the capacitor, which in turn can be traced to the incoming vacuum modes of the transmission line:

$$\delta n(\Omega) = -i\frac{2\pi\chi^{(3)}\sqrt{R\hbar\omega_e}V_0\omega_e^2}{\alpha(2\Omega + i\alpha)d^2}\left[a_{\text{in}}(\omega_e + \Omega) + a_{\text{in}}^\dagger(\omega_e - \Omega)\right],$$ (2.72)

where d is the distance between the plates of the capacitor. Collecting Equations (2.69), (2.70), (2.71) and (2.72) together, we can write down the expression for the phase quadrature of the outgoing wave in the transmission line, which is the measured readout signal:

$$\begin{aligned}
r(\Omega) &= \left[V_{\text{out}}(\omega_e + \Omega) - V_{\text{out}}^\dagger(\omega_e - \Omega)\right]/V_0 \\
&= \frac{\sqrt{R\hbar\omega_e}}{V_0}\frac{\alpha + i\Omega}{\alpha - i\Omega}\left[a_{\text{in}}(\omega_e + \Omega) - a_{\text{in}}^\dagger(\omega_e - \Omega)\right] + \\
&\quad + \frac{8\pi^2V_0\chi^{(3)}lN\hbar\omega_{\text{opt}}^2\omega_e}{V_0(2\Omega + i\alpha)VLc}\left\{x_s - \right. \\
&\quad \left. - \frac{8\pi^2\chi^{(3)}V_0\sqrt{R\hbar\omega_e}l}{RV(2\Omega + i\alpha)}\left(1 - \frac{6N\hbar}{mc^2\tau}\frac{\omega_{\text{opt}}^2}{\Omega^2}\right)\left[a_{\text{in}}(\omega_e + \Omega) + a_{\text{in}}^\dagger(\omega_e - \Omega)\right]\right\}.
\end{aligned}$$ (2.73)

The measured x is then given by

$$
\begin{aligned}
x_{\text{measured}}(\Omega) &= x_s(\Omega) - \frac{8\pi^2\chi^{(3)}\sqrt{\hbar\omega_e W}l}{V(2\Omega + \imath\alpha)}\left(1 - \frac{6N\hbar}{mc^2\tau}\frac{\omega_{\text{opt}}^2}{\Omega^2}\right)\left[a_{\text{in}}\left(\omega_e + \Omega\right) + a_{\text{in}}^\dagger\left(\omega_e - \Omega\right)\right] + \\
&\quad + \frac{VLc(2\Omega + \imath\alpha)\sqrt{\hbar\omega_e}}{16\pi^2\chi^{(3)}lN\hbar\omega_{\text{opt}}^2\omega_e\sqrt{W}}\left[a_{\text{in}}\left(\omega_e + \Omega\right) - a_{\text{in}}^\dagger\left(\omega_e - \Omega\right)\right],
\end{aligned}
\tag{2.74}
$$

where $W = V_0^2/R$ is the power pumped into the microwave oscillator by the generator G. The corresponding spectral density of the Gaussian noise seen by the readout system is

$$
\begin{aligned}
S_x(\Omega) &= \left(\frac{8\pi^2\chi^{(3)}l}{V}\right)^2\frac{\hbar\omega_e W}{4\Omega^2 + \alpha^2}\left(1 - \frac{6N\hbar}{mc^2\tau}\frac{\omega_{\text{opt}}^2}{\Omega^2}\right)^2 + \\
&\quad + \left(\frac{VLc}{16\pi^2\chi^{(3)}lN\hbar\omega_{\text{opt}}^2\omega_e}\right)^2\frac{(4\Omega^2 + \alpha^2)\hbar\omega_e}{W}.
\end{aligned}
\tag{2.75}
$$

The first term on the right-hand side corresponds to the back-action noise and the second term corresponds to the intrinsic noise of the measuring device.

We aim to perform a measurement with a narrow frequency band centered around the frequency Ω_0 at which the back-action noise is zero:

$$
\Omega_0 = \sqrt{\frac{6N\hbar}{m\tau}\frac{\omega_{\text{opt}}}{c}}.
\tag{2.76}
$$

We write S_x as a Taylor expansion in frequency around Ω_0:

$$
S_x(\Omega) \simeq A(\Omega_0)W\frac{(\Omega - \Omega_0)^2}{\Omega_0^2} + \frac{B(\Omega_0)}{W},
\tag{2.77}
$$

where A and B can be read from Eq. (2.75). If the relevant bandwidth is $\Delta\Omega$, then we place a limit $(\Omega - \Omega_0)^2 \leq \Delta\Omega^2$ and

$$
S_x(\Omega) \leq A(\Omega_0)W\frac{\Delta\Omega^2}{\Omega_0^2} + \frac{B(\Omega_0)}{W}.
\tag{2.78}
$$

Minimizing the right-hand side of the above equation with respect to W, we find the

expression for the minimum noise in a fixed bandwidth:

$$
\begin{aligned}
S_{x\,optimal}(\Omega) &\leq 2\sqrt{AB}\frac{\Delta\Omega}{\Omega_0} = \\
&= \frac{1}{2\pi^2}\frac{\lambda^2\tau}{N}\frac{\Delta\Omega}{\Omega_0} \sim S_{x\,\mathrm{SQL}}(\Omega_0)\frac{\Delta\Omega}{\Omega_0},
\end{aligned}
\tag{2.79}
$$

which is achieved at the input power

$$
W_{\mathrm{optimal}} = \frac{V^2}{32\pi^2\chi^{(3)^2}N\tau}\left(\frac{\Omega_0}{\omega_{\mathrm{opt}}}\right)^2\left(\frac{L}{l}\right)^2\frac{1}{\hbar\omega_e}\frac{\Omega_0}{\Delta\Omega}.
\tag{2.80}
$$

In the above expressions λ is the wavelength of light inside the FP resonator and $S_{\mathrm{SQL}}(\Omega_0)$ is the Standard Quantum Limit noise at the frequency Ω_0 for a free mass. Clearly, the signal-to-noise ratio for this narrow-band measurement is $\sqrt{\Omega_0/\Delta\Omega}$ greater than that in the case of the SQL:

$$
\left(\frac{S}{N}\right) \sim \left(\frac{S}{N}\right)_{\mathrm{SQL}}\sqrt{\frac{\Omega_0}{\Delta\Omega}}.
\tag{2.81}
$$

2.2.8 Appendix C: Perturbation theory for Fabry-Perot cavity with moving walls

In this appendix we derive a formal series for the optical field inside a Fabry-Perot resonator which is pumped by a monochromatic laser beam and the walls of which are free to perform motions small compared to the wavelength of light λ. The expansion parameter is $\delta x/\lambda$, where δx is the change of length of the resonator. For our purposes we are only interested in expanding up to $(\delta x/\lambda)^2$; and we use this formal series to derive Eq. (2.48).

The following situation is considered: for simplicity we assume that light is pumped on resonance by a laser beam $E_{\mathrm{in}} = \alpha e^{-i(\omega_{\mathrm{opt}}t-kx)}$ through the left mirror which is at rest and has reflectivity r and transmissivity T. For concreteness it is assumed that the fluctuations in length δx originate from the motion of the right mirror which is assumed to be perfectly reflecting. Further, we assume that the plain wave

approximation is applicable and hence the optical field inside the resonator satisfies the one-dimensional wave equation:

$$\left(\frac{\partial^2}{\partial t^2} - c^2 \frac{\partial^2}{\partial x^2} \right) A(x,t) = 0 \tag{2.82}$$

The general solution of of the above equation is

$$A(x,t) = f\left(t + \frac{x}{c} \right) + g\left(t - \frac{x}{c} \right) \tag{2.83}$$

where f and g are arbitrary functions. The boundary conditions at the left mirror $(x = 0)$ and at the right mirror $(x = L + \delta x)$ read respectively

$$g(t) - rf(t) = T\alpha e^{-\imath \omega_{\mathrm{opt}} t} \tag{2.84}$$

and

$$f\left(t + \tau_0 + \frac{\delta x}{c} \right) + g\left(t - \tau_0 - \frac{\delta x}{c} \right) = 0 \tag{2.85}$$

where $\tau_0 = L/c$. Eliminating $g(t)$ from these two equations, we get

$$\begin{aligned} f\left(t + \tau_0 + \frac{\delta x}{c} \right) &- rf\left(t - \tau_0 - \frac{\delta x}{c} \right) \\ &= T\alpha e^{-\imath \omega_{\mathrm{opt}} t} e^{\imath \omega_{\mathrm{opt}} \tau_0} e^{\imath \frac{\omega_{\mathrm{opt}}}{c} \delta x} \end{aligned} \tag{2.86}$$

or, expanding in δx up to second order,

$$\begin{aligned} f(t + \tau_0) - rf(t - \tau_0) &= T\alpha e^{-\imath \omega_{\mathrm{opt}} t} e^{\imath \omega_{\mathrm{opt}} \tau_0} \left(1 + \imath \frac{\omega_{\mathrm{opt}}}{c} \delta x - \frac{\omega_{\mathrm{opt}}^2}{c^2} \delta x^2 \right) \\ &\quad - \frac{1}{c} \left[f'(t + \tau_0) + rf'(t - \tau_0) \right] \delta x \\ &\quad - \frac{1}{2c^2} \left[f''(t + \tau_0) - rf''(t - \tau_0) \right] \delta x^2. \end{aligned} \tag{2.87}$$

We take a Fourier tranform of the above equation and then solve it by iterations:

$$f(\omega) = f^{(0)}(\omega) + f^{(1)}(\omega) + f^{(2)}(\omega) + \dots \tag{2.88}$$

where

$$f^{(0)}(\omega) = \frac{T\alpha}{1-r}\delta(\omega - \omega_{\text{opt}}),$$

(2.89)

$$f^{(1)}(\omega) = \frac{2\imath\omega_{\text{opt}}T\alpha}{c\left[(1-r)\cos(\omega\tau_0) - \imath(1+r)\sin(\omega\tau_0)\right](1-r)}\delta x(\omega - \omega_{\text{opt}}),$$

(2.90)

$$
\begin{aligned}
f^{(2)}(\omega) &= -\frac{4\omega_{\text{opt}}^2 T\alpha}{c^2\left[(1-r)\cos(\omega\tau_0) - \imath(1+r)\sin(\omega\tau_0)\right](1-r)} \\
&\times \int d\omega' \frac{\cos(\omega'\tau_0)\delta x(\omega' - \omega_{\text{opt}})\delta x(\omega - \omega')}{(1-r)\cos(\omega'\tau_0) - \imath(1+r)\sin(\omega'\tau_0)}.
\end{aligned}
$$

(2.91)

When writing down the above terms we took into account the fact that $1 - r \ll 1$. The structure of $f^{(2)}$ is clear: it corresponds to upconversion of light at frequency ω_{opt} to an intermediate frequency ω' and then from ω' to ω, with ω' being integrated over. From Eqs. (2.83) and (2.84)

$$A(x,\omega) \simeq -2\imath \sin\left(\frac{\omega}{c}x\right)f(\omega).$$

(2.92)

The BK readout system detects the square of the amplitude of the optical field:

$$
\begin{aligned}
S(x,t) &\equiv |A(x,t)|^2 \\
&= S^{(0)}(x,t) + S^{(1)}(x,t) + S^{(2)}(x,t) + \ldots
\end{aligned}
$$

(2.93)

where

$$S^{(0)}(x,\Omega) = 4\sin^2\left(\frac{\omega_{\text{opt}}}{c}x\right)C^2\delta(\Omega),$$

(2.94)

$$S^{(1)}(x,\Omega) = 0$$

(2.95)

and

$$
\begin{aligned}
S^{(2)}(x,\Omega) &= -\left(\frac{2\omega_{\text{opt}}C}{c}\right)^2 \int \left\{ \frac{\sin\left[\frac{\omega_{\text{opt}}-\Omega'}{c}x\right]\sin\left[\frac{\omega_{\text{opt}}+\Omega-\Omega'}{c}x\right]}{\mathcal{L}(\Omega')\mathcal{L}(\Omega-\Omega')} + \right. \\
&\left. \frac{2\left[\sin\left(\frac{\omega_{\text{opt}}+\Omega}{c}x\right) + \sin\left(\frac{\omega_{\text{opt}}-\Omega}{c}x\right)\right]}{\mathcal{L}(\Omega)\mathcal{L}(\Omega')} \right\} \delta x(\Omega')\delta x(\Omega - \Omega')d\Omega'.
\end{aligned}
$$

(2.96)

In the above expression $C \equiv T\alpha/(1-r)$ and

$\mathcal{L}(\Omega) \equiv (1-r)\cos(\Omega\tau) + (1+r)\sin(\Omega\tau)$.

In real interferometers δx represents, for example, motion of the surface of the mirror due to the thermal excitation of the test mass's internal modes. In what follows the contribution from the internal mode of lowest frequency is considered and then it will be shown that the sum of contributions of all the higher modes will have the same order of magnitude. It is assumed that the thermal noise is a Markoff Gaussian process, and therefore is described by the following equation:

$$\delta x(\Omega) = \frac{F(\Omega)}{\Omega^2 - \Omega_m^2 + i\gamma_m\Omega}, \tag{2.97}$$

where Ω_m is the eigenfrequency of the mechanical mode, γ_m is the damping rate and $F(\Omega)$ is the Langevin force satisfying

$$\langle F(\Omega_1)F(\Omega_2)\rangle = \frac{D}{2\pi}\delta(\Omega_1 + \Omega_2), \tag{2.98}$$

where $D = k_B T_e \gamma_m/m^*$ is the velocity diffusion rate. Here m^* is the effective mass of the mode (approximately given by the mirror mass m), k_B is Boltzmann's constant and T_e is the temperature of the enviroment. To calculate the spectral density of the fluctuations of $S^{(2)}$ (the goal of this analysis), we will need the 4-point correlation function:

$$\langle F(\Omega_1)F(\Omega_2)F(\Omega_3)F(\Omega_4)\rangle = \frac{D^2}{8\pi^2}[\delta(\Omega_1 + \Omega_2)\delta(\Omega_3 + \Omega_4) \tag{2.99}$$
$$+\delta(\Omega_1 + \Omega_3)\delta(\Omega_2 + \Omega_4) + \delta(\Omega_1 + \Omega_4)\delta(\Omega_2 + \Omega_3)].$$

Using the above expression, Eq. (2.96) and Eq. (2.97), we obtain

$$\langle S^{(2)}(x,\Omega_1)S^{(2)}(x,\Omega_2)\rangle = (2\omega_0 C)^4 [M_1\delta(\Omega_1)\delta(\Omega_2) + M_2(x,\Omega_1)\delta(\Omega_1 + \Omega_2)]. \tag{2.100}$$

Here $M_2(\Omega)$, which characterizes the spectral density of fluctuations of $S^{(2)}$, is given

by

$$M_2(x,\Omega) = \frac{D^2}{8\pi^2} \int \left[K\left(\Omega,\Omega'\right) K\left(-\Omega,-\Omega'\right) + \right. \qquad (2.101)$$
$$\left. K\left(\Omega,\Omega'\right) K\left(-\Omega,-\Omega+\Omega'\right)\right] d\Omega',$$

where

$$K(\Omega,\Omega') = \frac{1}{\mathcal{L}(\Omega')(\Omega'^2 - \Omega_m^2 + \imath\gamma_m\Omega')\left[(\Omega-\Omega')^2 - \Omega_m^2 + \imath\gamma_m\left(\Omega-\Omega'\right)\right]}$$
$$\left\{ \frac{\sin\left(\frac{\omega_{\mathrm{opt}}-\Omega'}{c}x\right)\sin\left(\frac{\omega_{\mathrm{opt}}+\Omega-\Omega'}{c}x\right)}{\mathcal{L}(\Omega-\Omega')} \right. \qquad (2.102)$$
$$\left. + \frac{\left[\sin\left(\frac{\omega_{\mathrm{opt}}+\Omega}{c}x\right) + \sin\left(\frac{\omega_{\mathrm{opt}}-\Omega}{c}x\right)\right]\sin\left(\frac{\omega_{\mathrm{opt}}}{c}x\right)}{\mathcal{L}(\Omega)} \right\}.$$

It is possible to integrate Eq. (2.101) exactly, but it is clear that the main contribution will come from mechanical and optical resonances, $\Omega' = \Omega_{\mathrm{opt}}$ and $\Omega' = \Omega_m$. For $\gamma_m \ll (1-r)/\tau$ (which is the case for, e.g., fused silica) the major contribution in Eq. (2.101) is due to the mechanical resonances:

$$M_2(x,\Omega) \sim \frac{D^2}{8\pi^2}(2\omega_{\mathrm{opt}}C)^2\left[K_1\left(x,\Omega\right) + K_2\left(x,\Omega\right) + K_3\left(x,\Omega\right)\right] \qquad (2.103)$$

where

$$K_1(x,\Omega) \sim \frac{2\sin^2\left(\frac{\omega_{\mathrm{opt}}-\Omega_m}{c}x\right)\sin^2\left(\frac{\omega_{\mathrm{opt}}+\Omega_m}{c}x\right) + \sin^4\left(\frac{\omega_{\mathrm{opt}}+\Omega_m}{c}x\right) + \sin^4\left(\frac{\omega_{\mathrm{opt}}-\Omega_m}{c}x\right)}{16\sin^4(\Omega_m\tau)\Omega_m^4\Omega^2\gamma_m},$$
$$(2.104)$$

$$K_2(x,\Omega) \sim \frac{\left[\sin\left(\frac{\omega_{\mathrm{opt}}+\Omega}{c}x\right) + \sin\left(\frac{\omega_{\mathrm{opt}}-\Omega}{c}x\right)\right]^2}{16\sin^2(\Omega_m\tau)(\Omega\tau)^2\Omega_m^4\Omega^2\gamma_m}, \qquad (2.105)$$

$$K_3(x,\Omega) \sim \frac{\left[\sin^2\left(\frac{\omega_{\mathrm{opt}}+\Omega_m}{c}x\right) + \sin^2\left(\frac{\omega_{\mathrm{opt}}-\Omega_m}{c}x\right)\right]\sin^2(\frac{\omega_{\mathrm{rmopt}}}{c}x)}{16\sin^3(\Omega_m\tau)(\Omega\tau)\Omega_m^4\Omega^2\gamma_m}. \qquad (2.106)$$

We are only interested in detection frequencies such that $\Omega\tau \ll 1$. Then for the configuration of nonlinear slabs shown in Fig. 2.2, the main contribution to the noise in the BK meter readout will come from K_2 and K_3. The spectral density of the

displacement noise will be

$$S_{\delta x} \sim \frac{1}{8\pi^2} \left(\frac{k_B T_e}{m^*}\right)^2 \frac{\omega_{\text{opt}}^2}{c^2} \frac{\gamma_m}{\Omega_m^4 \Omega^2 (\Omega\tau)^2} (\Omega\tau + \epsilon), \qquad (2.107)$$

where ϵ characterizes the degree of positioning error and the mismatch of nonlinearities of the two slabs:

$$\epsilon \sim \max\left(\frac{|\chi_1^{(3)}| - |\chi_2^{(3)}|}{\chi_1^{(3)}}, \frac{\delta l}{\lambda}\right). \qquad (2.108)$$

Here δl is the spatial offset of the central point between the two slabs.

Equation (2.107) is the main result of this Appendix. Its implications are discussed at the end of Sec. 2.2.4.

Bibliography

[1] A. Abramovici *et al.*, Science, **256**, 325 (1992); C. Baradaschia *et al.*, Nucl. Instrum & Methods, **A289**, 518 (1990).

[2] K. S. Thorne, Chapter 9 of *300 Years of Gravitation*, eds. S. W. Hawking and W. Israel (Cambridge University Press, Cambridge 1987), pp. 430–432.

[3] V. B. Braginsky and F. Ya. Khalili, *Phys. Lett. A*, **218**, 167 (1996).

[4] See, e.g., V. B. Braginsky and F. Ya. Khalili, *Quantum Measurement* (Cambridge University Press, 1992).

[5] V. B. Braginsky and F. Ya. Khalili, *Rev. Mod. Phys.*, **68**, 1 (1996).

[6] W. G. Unruh, in *Quantum Optics, Experimental Gravitation and Measurement theory*, eds. Pierre Meystre and Marlin O. Scully (Plenum, 1982), p. 647; M. T. Jaekel and S. Reynaud, *Europhys. Lett.*, **13**, 301 (1990); S. P. Vyatchanin and E. A. Zubova, *Phys. Lett. A*, **201**, 269 (1995); also an unpublished narrow-band QND scheme by W. G. Unruh is described in Ref. [2].

Chapter 3   Issues in thermal noise for LIGO

3.1 Paper III: Internal thermal noise in the LIGO test masses: a direct approach.

ABSTRACT

The internal thermal noise in LIGO's test masses is analyzed by a new technique, a direct application of the Fluctuation-Dissipation Theorem to LIGO's readout observable, $x(t) =$ (longitudinal position of test-mass face, weighted by laser beam's Gaussian profile). Previous analyses, which relied on a normal-mode decomposition of the test-mass motion, were valid only if the dissipation is uniformly distributed over the test-mass interior, and they converged reliably to a final answer only when the beam size was a non-negligible fraction of the test-mass cross section. This paper's direct analysis, by contrast, can handle inhomogeneous dissipation and arbitrary beam sizes. In the domain of validity of the previous analysis, the two methods give the same answer for $S_x(f)$, the spectral density of thermal noise, to within expected accuracy. The new analysis predicts that thermal noise due to dissipation concentrated in the test mass's front face (e.g., due to mirror coating) scales as $1/r_0^2$, by contrast with homogeneous dissipation, which scales as $1/r_0$ (r_0 is the beam radius); so surface dissipation could become significant for small beam sizes.

3.1.1 Introduction

Random thermal fluctuations are expected to be the dominant noise source for the first interferometers in the Laser Interferometer Gravitational Wave Observatory (LIGO) at frequencies between 35 and 100 Hz [1]. This thermal noise is generally decomposed into a suspension thermal noise and an internal thermal noise for the test masses. The former can be traced back to the friction in the test masses' pendular suspension system; the latter is due to internal damping inside the test masses themselves. Traditionally, thermal noise calculations have been based on a normal-mode expansion [2], [3]. However, Gonzalez and Saulson have also performed an exact calculation of the suspension thermal noise by applying directly the Fluctuation-Dissipation (FD) theorem [5] in its most general form, due to H. B. Callan and T. A. Welton [9]. The purpose of this paper is to use the general method of Gonzales and Saulson to calculate the internal thermal noise (also, [10] has somewhat complementary to this

paper's treatment of the internal thermal noise).

In Section 3.1.2 we analyze a general situation when a measuring device (e.g., a laser interferometer) monitors the displacement of the surface of a test mass whose internal degrees of freedom are in thermal equilibrium with each other. We develop a general formalism for using the FD theorem to calculate the thermal noise in the most general surface readout quantity. In brief our method is as follows:

To work out the thermal noise at a particular frequency f, one should mentally apply pressure oscillating at this frequency to the observed surface of the test mass. The spatial variation of this pressure should mimic that of the light beam intensity (for example, in the case of a gaussian beam this oscillating pressure has a gaussian profile of the same width as the beam). The thermal noise is then given by

$$S_x(f) = \frac{2k_B T}{\pi^2 f^2} \frac{W_{diss}}{F_0^2},$$
(3.1)

where k_B and T are the Boltzmann's constant and the temperature of the mirror respectively, F_0 is the amplitude of the oscillating force applied to the surface (i.e., the pressure integrated over the surface), and W_{diss} is the time-averaged power dissipated in the test mass when this oscillating pressure is applied.

To demonstrate the computational power of this general approach, in Section 3.1.3 we consider the case of a cylindrical fused silica test mass monitored by a circular gaussian laser beam. For the case when the radius of the beam is much less then the size of the test mass and the dissipation is uniformly distributed throughout test mass volume, we derive an analytical expression for the thermal noise [cf. Eq. (3.15) of Section 3.1.3]:

$$S_x(f) = \frac{4k_B T}{f} \frac{1 - \sigma^2}{\pi^3 E_0 r_0} I \phi \left[1 + O\left(\frac{r_0}{R}\right) \right].$$
(3.2)

Here σ, E_0, and ϕ are the Poisson ratio, Young's modulus, and dissipational loss angle [Eq. (3.11)] of the test-mass material, r_0 is the radius of the laser beam (which is defined here as a radius at which the intensity of light is $1/e$ of the maximum intensity), R is a characteristic size of the test mass, and $I = 1.87322...$ in the case of a gaussian beam. Putting numbers in Eqs. (3.1) and (3.2), we find that our results are

in agreement with those of Raab and Gillespie [3], who used the more complicated and computationally involved method of normal-mode decomposition. It is interesting to note that as r_0/R tends to zero, our simple analytical formula becomes more precise, whereas the more complicated and computationally involved method of normal-mode decomposition requires summing over a larger number of modes and thus becomes computationally more expensive.

Not only can the normal-mode decomposition be computationally expensive, it can also be misleading. We demonstrate this point in Section 3.4.4 by considering a test mass which has a lossy surface, e.g., due to a lossy mirror coating. We estimate the contribution of the surface to the thermal noise using the general method of Section 3.1.2, and show that it differs from the estimate obtained by the method of normal modes (which gives a result too small by a factor of at least $\sim r_0/R$). This breakdown of the normal-mode analysis will in general happen when the sources of friction are not distributed homogeneously over the test mass. The fundamental reason is that in this case different normal modes can have a common Langevin driving force (which is not so if the defects are distributed homogeneously).

Our analysis shows that thermal noise due to surface losses near the laser beam spot scales as $S_x(f) \propto 1/r_0^2$, whereas thermal noise due to volume losses scales as $1/r_0$. Correspondingly, for small beam spots the surface losses could become significant. To protect against this, it is important to keep the surface near the laser beam spot as free of potential sources of friction as possible.

3.1.2 General method

For concreteness, consider a situation where LIGO's laser beam is shining on the circular surface of one of LIGO's cylindrical test masses. The phase shift of the reflected light contains information about the motion of the test mass's surface. The variable read out by this procedure can be written as

$$x(t) = \int f(\vec{r}) y(\vec{r}, t) d^2 r. \tag{3.3}$$

Here $\vec{r}$ is the transverse location of a point on the test-mass surface, and $y(\vec{r}, t)$ is the displacement of the boundary along the direction of the laser beam at point $\vec{r}$ and time t. The form factor $f(\vec{r})$ depends on the laser beam profile and is proportional to the laser light intensity at the point $\vec{r}$ [3]; it is normalized by $\int f(\vec{r})d^2r = 1$.

The internal thermal noise of the test mass is defined as the fluctuations in $x(t)$, and our objective is to find the spectral density $S_x(f)$ of these fluctuations. We assume that the test mass is in thermal equilibrium at temperature T.

Callen and Welton's generalized Fluctuation-Dissipation Theorem [9] says that the spectral density of the fluctuations of LIGO's readout variable $x(t)$ is given by the formula

$$S_x(f) = \frac{k_B T}{\pi^2 f^2} \left| Re\left[Y\left(f\right)\right] \right|, \tag{3.4}$$

where k_B is Boltzman's constant and $Y(f)$ is a complex admittance associated with $x(t)$. This complex admittance can be understood and computed as follows. Introduce a special set of generalized coordinates for the test mass's degrees of freedom–a set for which x is one of the coordinates. (Since x is not the coordinate of a normal mode of the test mass, these generalized coordinates will not be the usual ones associated with normal modes.) Apply to the test mass a generalized force $F(t)$ that drives the generalized momentum conjugate to x but does not drive any of the other generalized momenta. This generalized force will show up as the following interaction term in the test mass's Hamiltonian:

$$H_{\text{int}} = -F(t)x. \tag{3.5}$$

This driving force, together with the test mass's internal elastic forces and internal dissipation, will generate a time evolution $x(t)$ of the observable x. Denote by $F(f)$ and $x(f)$ the Fourier transforms of the (arbitrary) driving force $F(t)$ and the observable's response $x(t)$. Then the admittance that appears in the thermal noise formula Eq. (3.4) is

$$Y(f) = 2\pi \imath f x(f)/F(f). \tag{3.6}$$

The physical nature of the driving force $F(t)$ can be deduced by inserting the

definition (3.3) of the observable x into the interaction Hamiltonian (3.5):

$$H_{\text{int}} = -\int P(\vec{r})y(\vec{r}, t)d^2r, \tag{3.7}$$

where

$$P(\vec{r}, t) = F(t)f(\vec{r}). \tag{3.8}$$

From Eq. (3.7) we see that the generalized force $F(t)$ consists of a pressure $P(\vec{r}, t)$ [Eq. (3.8)] applied to the test mass's surface. Note that the spatial distribution of this pressure is the same as LIGO's laser beam intensity profile.

The real part of the admittance, $Re[Y(f)]$, describes the coupling of the test mass's dissipation to the observable x. We can see this most clearly by applying an oscillatory pressure $P(\vec{r}, t) = F_0 \cos(2\pi ft)f(\vec{r})$ to the test mass's face. From the response formula (3.6) we infer that the power W_{diss} that this oscillatory pressure feeds into the test mass, and that the test mass then dissipates, is related to $|Re[Y(f)]|$ by

$$|Re\left[Y\left(f\right)\right]| = \frac{2W_{\text{diss}}}{F_0^2}. \tag{3.9}$$

Substituting Eq. (3.9) into Eq. (3.4), we get

$$S_x(f) = \frac{2k_B T}{\pi^2 f^2}\frac{W_{\text{diss}}}{F_0^2}. \tag{3.10}$$

Equation (3.10) is the most important equation of this paper. Let us reephasize it's physical content:

1. Apply an oscillatory pressure
   $P(\vec{r}, t) = F_0 \cos(2\pi ft)f(\vec{r})$ to the face of the test mass.

2. Work out the average power W_{diss} dissipated in the test mass under the action of this oscillatory pressure.

3. Use F_0 and W_{diss} in Eq. (3.10) to calculate $S_x(f)$.

This procedure is different from the one employed in previous calculations of internal thermal noise for the LIGO and VIRGO test masses [2], [3], [4]. The previous authors decomposed a test mass's motion into normal elastic modes; then they calculated the contribution of each mode to S_x independently and added up these contributions. This method of "normal-mode decomposition" works fine in many cases, but it has two drawbacks:

1. The fundamental assumption in this method is that different normal modes have independent Langevin forces. This assumption is correct only if the sources of friction are homogeneously distributed over the test-mass volume. It breaks down if the defects are more concentrated in one place than in others— for example, when there is significant damping concentrated in the test-mass surface. We will return to this in Section IV.

2. For a small laser beam diameter the sum over normal modes converges very slowly, so one has to sum over many modes, which may be computationally expensive. By contrast, using the new method described in this paper, one can write down a simple analytic expression for the low-frequency noise in the case of a narrow laser beam. In the next section we derive this expression and make comparison with the normal-mode decomposition results derived in [3].

3.1.3 Thermal noise due to homogeneously distributed damping

Consider the case where all the friction in the test mass comes from homogeneously distributed damping. It is conventional to characterize such friction by an imaginary

part of the material's Young's modulus:

$$E = E_0 \left[1 + \imath \phi(f) \right]; \tag{3.11}$$

$\phi(f)$ is called the material's "loss angle." It is suspected [6], [2] that for fused silica, which will be used in LIGO's test masses, ϕ might be independent of frequency within LIGO's detection band (but there is no evidence for such behavior of ϕ for figh-quality resonators—see [7] for some healthy scepticism). In this f-independent case the damping is called "structural."

To calculate the thermal noise for homogeneous dissipation, we express W_{diss} in Eq. (3.10) as

$$W_{\text{diss}} = 2\pi f U_{\text{max}} \phi(f), \tag{3.12}$$

where U_{max} is the energy of elastic deformation at a moment when the test mass is maximally contracted or extended under the action of the oscillatory pressure of Eq. (3.8).

LIGO's detection frequencies $(10 - 300\text{Hz})$ are much lower than the eigenfrequencies of the test mass's normal modes (the lowest of which is $\sim 6\text{kHz}$); so we can assume constant, non-oscillating pressure $P(\vec{r}) = F_0 f(\vec{r})$ when evaluating U_{max}.

In the case when the beam profile is gaussian and the centre of the light spot coincides with the centre of the transverse coordinates, we have

$$f(\vec{r}) = \frac{1}{\pi r_0^2} e^{-r^2/r_0^2}, \tag{3.13}$$

where r_0 is the radius of the laser beam. When the characteristic size of the test mass R is much greater than r_0, we can approximate the test mass as an infinite half-space in order to find U_{max}. Appendix A uses elasticity theory to derive U_{max} in this case [cf. Eq. (3.27)]:

$$U_{\text{max}} = \frac{F_0^2}{\pi^2 E_0 r_0} (1 - \sigma^2) I \left[1 + O \left(\frac{r_0}{R} \right) \right], \tag{3.14}$$

where E_0 and σ are the Young's modulus and Poisson ratio of the material respec-

tively, and $I \simeq 1.87322$. Here $O(r_0/R)$ is a correction due to the finite size of the cylinder. Putting Eqs. (3.14) and (3.12) into Eq. (3.10), one gets

$$S_x(f) = \frac{4k_B T}{f} \frac{1-\sigma^2}{\pi^3 E_0 r_0} I\phi \left[1 + O\left(\frac{r_0}{R}\right)\right]. \tag{3.15}$$

Below we take the numerical values [1] used by Gillespie and Raab [3]: $r_0 = 1.56$cm, $E_0 = 7.18 \times 10^{10}$Pa, $\sigma = 0.16$, $\phi = 10^{-7}$, the mirror diameter of 25cm and the mirror length of 10cm. Gillespie and Raab, after summing over the relevant ~ 30 modes, get

$$S_x^{\text{GR}}(100\text{Hz}) \simeq 8.0 \times 10^{-40} \text{m}^2/\text{Hz}. \tag{3.16}$$

Our analytical approximation (3.15) (which should be valid to within ~ 10 percent in this case) gives

$$S_x(100\text{Hz}) \simeq 8.7 \times 10^{-40} \text{m}^2/\text{Hz}. \tag{3.17}$$

Notice that our analytic expression in Eq. (3.15) gets more exact when $r_0/R \to 0$, whereas, by contrast, the sum over modes converges more slowly and gets more complicated.

The ratio r_0/R may turn out to be of order unity in real experiments. In this case, Eq. (3.15) can only be used for order-of-magnitude estimates. To work out the exact value of the internal thermal noise, one would need to calculate U_{max} numerically. We have done such a numerical computetion using finite-element techniques. More specifically, we have used finite-element software called PDEase2D [Version 3.0], which runs as part of Mascyma [Version 2.1], to solve the elasticity equations for the loaded mirror and to compute U_{max} and, by virtue of Eqs. (3.12) and (3.10), S_x. The exact answer for the mirror and light spot parameters given above is

$$S_x(100\text{Hz}) = 8.76 \times 10^{-40} \text{m}^2/\text{Hz}, \tag{3.18}$$

which is consistent (better than expected) with our analytical approximation.

---

[1]Note that our definition of the beam radius (location where intensity has fallen to $1/e$ of its central value) differs by $\sqrt{2}$ from the beam radius of Ref. [3] (location of $1/e$ amplitude falloff).

The purpose of the present section is to convince the reader that the method presented in this paper is correct and could be computationally cheaper than the normal-mode expansion. The next section concentrates on the cases where a direct application of the FD theorem can be crucial for getting the right results, and the method of normal-mode decomposition fails.

3.1.4   The case of surface damping

In this section we study thermal noise due to surface losses–caused, e.g., by inadequate polishing or by a lossy mirror coating.

From Eq. (3.10) we see that the key quantity in the thermal noise calculation is the power dissipated in the test mass when an oscillating pressure is applied to the laser beam spot on the test-mass surface. The power dissipated at each point of the material is proportional to the square of the stress at this point. Most of the surface stress is in or near the spot to which the pressure is applied, so

$$W_{\text{diss}}^{\text{coating}} \propto \left(\frac{F_0}{r_0^2}\right)^2 r_0^2 = \frac{F_0^2}{r_0^2}. \tag{3.19}$$

Thus the thermal noise due to the surface damping scales like

$$S_x(\text{boundary}) \propto 1/r_0^2. \tag{3.20}$$

For comparison, the thermal noise due to bulk damping [Eq. (3.15)] scales as

$$S_x(\text{bulk}) \propto 1/r_0. \tag{3.21}$$

Thus as the spot size decreases, the thermal noise due to surface damping grows faster than that due to bulk damping.

Contrast this conclusion with the intuition one gets from normal-mode decomposition. There one is concerned with how much the surface contributes to the quality factors (Q's) of the normal modes. For a typical mode the strain at the surface is at

most of the same order as the characteristic strain inside the test mass (likely, much less for first few modes—because of the free boundary condition). Therefore, one would presume that the surface contributes no more than some mode-independent fraction of the test mass's Q's. In order of magnitude this fraction should be the ratio of the power dissipated in the surface to that in the bulk if one applies an oscillating pressure uniformly to the whole surface, which in the context of our method corresponds to a beam radius of R. Therefore the normal-mode estimate of the surface thermal noise is at least r_0/R less than the correct value.

Current experiments show that the mirror coating does not contribute significantly to the $Q's$ of the test-mass normal modes. The conclusion commonly made is that coating is also not likely to contribute significantly to the internal thermal noise. The above analysis shows that this conclusion is not justified and that there might be a significant contribution of the coating to the internal thermal noise, despite the fact that Q's are not significantly changed.

3.1.5   Discussion and conclusion

The normal-mode decomposition of the thermal noise is exact when the defects are distributed homogeneously through the volume of the test mass. However, as was shown explicitly in Section IV for the case of surface losses, when the defect distribution is not homogeneous, the normal-mode decomposition may be misleading, and a direct application of the Fluctuation-Dissipation theorem is required.

Thermal noise is ultimately linked to friction in the test mass; this friction is caused by various (structural and otherwise) defects. Those defects which are closer to the beam spot will contribute more to the thermal noise that is read out by the laser beam's phase shift. Although this fact is a direct consequence of the formalism developed in this paper, we would like to give an intuitive example in order to emphasize this point.

Consider, for the sake of simplicity, a one dimensional elastic test mass with two identical defects A and B, as shown on Fig. 3.1; A is closer to the beam spot than
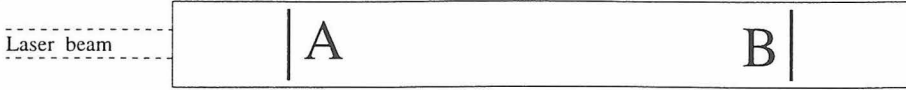
Figure 3.1: **Example of normal-mode decomposition breakdown.**
Identical defects A and B create fluctuating strees in different parts of the test mass.
The stress created by defect A will influence the phase shift of the laser beam readout
more than the stress created by defect B, although both A and B make identical
contributions to Q's of the test mass's elastic modes.

B. Each of these defects creates a random stress which pushes apart or pulls together
the left and right (relative to the defect) parts of the test mass. By conservation
of momentum, the part of the test mass which is lighter will respond more to the
random stress than the other part; therefore defect A will have a larger effect on the
optical readout than the B.

Note that if the defects A and B are positioned symmetrically with respect to
the centre of the test mass, they will have the same effect on the Q's of all elastic
modes (we assume for simplicity that only one-dimensional longitudinal modes are
present—and all of them are either symmetric or antisymmetric with respect to the
centre). Therefore, the normal-mode decomposition applied to the test-mass with
just one defect—A or B—would give the same result for the thermal noise as read
by the laser. Clearly, we have found yet another illustration of the breakdown of the
normal-mode decomposition .

The considerations presented above lead to the following advice for real experi-
ments: keep the neighbourhood of the laser beam spot as clean of defects as possible.

Not only does our direct applicatin of the Fluctuation-Dissipation Theorem have
broader validity than the normal-mode decomposition; it is also be computationally
simpler. In the case of homogeneous structural damping it yields a simple analytical
expression for the internal thermal noise spectrum [cf. Eq. (3.15)]:

$$S_x(f) = \frac{4k_B T}{f} \frac{1 - \sigma^2}{\pi^3 E_0 r_0} I\phi \left[1 - O\left(\frac{r_0}{R}\right)\right]. \tag{3.22}$$

This result is consistent with the numerical sum-over-modes done in Ref. [3] and is
accurate when the radius of the laser beam is small relative to the size of the test mass,

i.e. in the regime when the sum over modes converges especially slowly. When r_0/R is not small, a numerical solution of the elasticity equations to deduce the dissipation power W_{diss}, and thence the thermal noise (10), is straightforward and is probably also much simpler than performing a sum over modes.

Acknowledgements

3.1.6 Appendix: The strain energy in a test mass subjected to a gaussianly distributed surface pressure

The objective of this Appendix is to derive Eq. (3.14) of Section III for the energy of elastic strain in a cylindrical test mass when the pressure $P(\vec{r}) = F_0 f(\vec{r})$ is applied to one of it's circular faces. (As was discussed in Section III, we can assume that the pressure is constant in time since LIGO's detection frequencies are much lower than the lowest normal-mode frequency.) For a circular laser beam with a gaussian intensity profile $f(\vec{r})$ is given by [cf. Eq. (3.13)]

$$f(\vec{r}) = \frac{1}{\pi r_0^2} e^{-r^2/r_0^2}, \tag{3.23}$$

where we assume that the centre of the light spot coincides with the centre of the test mass's circular face.

If the radius of the laser beam r_0 is small compared to the size of the test mass, we can approximate the test mass by an infinite elastic half-space. Then our calculation of the elastic energy is correct up to a fractional accuracy of $O(r_0/R)$, where R is the

characteristic size of the test mass.

Let $y(\vec{r})$ be the normal displacement of the surface at location $\vec{r}$ under the action of the pressure $P(\vec{r})$. In the linear approximation of small strains

$$y(\vec{r}) = \int G(\vec{r}, \vec{r'}) P(\vec{r'}) d^2 r', \tag{3.24}$$

where $G(\vec{r}, \vec{r'})$ is a Green's function. The calculation of G is a non-trivial albeit standard exercise in elasticity theory [8], which gives

$$G(\vec{r}, \vec{r'}) = \frac{1 - \sigma^2}{\pi E_0} \frac{1}{|\vec{r} - \vec{r'}|}, \tag{3.25}$$

where σ is the Poisson ratio and E_0 the Young's modulus of the material. The elastic energy stored in the material is

$$\begin{aligned}
U_{\text{max}} &= \int P(\vec{r}) y(\vec{r}) d^2 r \\
&= \frac{1 - \sigma^2}{\pi E_0} \int \frac{P(\vec{r}) P(\vec{r'})}{|\vec{r} - \vec{r'}|} d^2 r d^2 r' \\
&= \frac{1 - \sigma^2}{\pi^3 E_0 r_0^4} F_0^2 \int \frac{e^{-(r^2 + r'^2)/r_0^2}}{\sqrt{r^2 + r'^2 - 2rr' \cos\theta}} d^2 r d^2 r',
\end{aligned} \tag{3.26}$$

where θ is the angle between $\vec{r}$ and $\vec{r'}$. The integral in the last term of Eq. (3.26) (as was pointed out by Glenn Sobermann) can be taken by introducing "polar" coordinates R and ϕ: $r = R \cos\phi$, $r' = R \sin\phi$. One then integrates out the radial part of the integrand and expands the remaining angular part in a power series with respect to $\cos\theta$; termwise integration of this power series finally yields Eq. (3.14) [up to a fractional error of $O(r_o/R)$]

$$U_{\text{max}} \simeq \frac{F_0^2}{\pi^2 E_0 r_0} (1 - \sigma^2) I, \tag{3.27}$$

where

$$I = \frac{\pi^{3/2}}{4} \left[1 + \sum_{n=1}^{\infty} \frac{(4n-1)!!}{(2n)! 4^n (2n+1)} \right] \simeq 1.87322. \tag{3.28}$$

It can be shown that if, instead of an infinite half-space, we consider a finite cylindrical test mass, the leading fractional correction to the elastic energy is of the order $O(r_0/R)$.

Bibliography

[1] A. Abramovici *et al.*, Science, **256**, 325 (1992); C. Baradaschia *et al.*, Nucl. Instrum & Methods, **A289**, 518 (1990).

[2] P. R. Saulson, *Phys. Rev. D*, **42**, 2437-2445 (1990).

[3] A. Gillespie and F. Raab, *Phys. Rev. D*, **52**, 577-585 (1995).

[4] F. Bondu and J. Y. Vinet, *Phys. Lett. A*, **198 (2)**, 74-78 (1995).

[5] G. I. Gonzalez and P. R. Saulson, *J. Accoust. Soc. Am*, **96**, 207-212 (1994).

[6] A. Gillespie and F. Raab, *Phys. Lett. A*, **178**, 357-363 (1993).

[7] V. B. Braginsky et al., *Phys. Lett. A*, **218**, 164-166 (1996) and references therein; private communications.

[8] Equation (8.19) of L. D. Landau and E. M. Lifshitz, *Theory of Elasticity* (Pergamon Press, New York, 1986).

[9] H. B. Callen and T. A. Welton, *Phys. Rev.* **83**, 34-50 (1951).

[10] N. Nakagawa et al., *Rev. Sci. Instrum.* **68(9)**, 1-4 (1997).

3.2 Paper IV: How to reduce the suspension thermal noise in LIGO without improving the Q's of the pendulum and violin modes.

Written with V. B. Braginsky and S. P. Vyatchanin,

To appear in Measurement Science and Technology

ABSTRACT

The suspension noise in interferometric gravitational wave detectors is caused by losses at the top and the bottom attachments of each suspension fiber. We use the Fluctuation-Dissipation theorem to argue that by careful positioning of the laser beam spot on the mirror face it is possible to reduce the contribution of the bottom attachment point to the suspension noise by several orders of magnitude. For example, for the initial and enhanced LIGO design parameters (i.e., mirror masses and sizes, and suspension fibers' lengths and diameters) we predict a reduction of ~ 100 in the "bottom" spectral density throughout the band $35 - 100$Hz of serious thermal noise.

We then propose a readout scheme which suppresses the suspension noise contribution of the top attachment point. The idea is to monitor an averaged horizontal displacement of the fiber of length l; this allows one to record the contribution of the top attachment point to the suspension noise, and later subtract it from the interferometer readout. This method will allow a suppression factor in spectral density of $7.4 \ (l/d^2) \ \sqrt{Mg/\pi E}(\Delta l/d^2)$, where d is the fiber's diameter, E is it's Young modulus and M is the mass of the mirror. For the test mass parameters of the initial and enhanced LIGO designs this reduction factor is $132 \times (l/30\text{cm})(0.6\text{mm}/d)^2$.

We offer what we think might become a practical implementation of such a readout scheme. We propose to position a thin optical waveguide close to a fused silica fiber used as the suspension fiber. The waveguide itself is at the surface of a solid fused silica slab which is attached rigidly to the last mass of the seismic isolation stack (see Fig. 3.6). The thermal motion of the suspension fiber is recorded through the phaseshift of an optical wave passed through the waveguide. A laser power of 1mW should be sufficient to achieve the desired sensitivity.

3.2.1 Introduction

Random thermal motion will be the dominant noise source in the frequency band of $35 - 100$ Hz for the first interferometers [1] and in the frequency band of $25 - 126$

Hz for the enhanced interferometers [2] in the Laser Interferometer Gravitational Wave Observatory (LIGO) [3].

The thermal noise in this frequency band is caused by the losses in the suspension fibers, in particular at the top and the bottom of each fiber's attachment point. So far the only known way to reduce the thermal noise has been to improve the quality of the suspension fibers and their attachments. Here we suggest a different approach:

In Section 3.2.2 we will present a general analysis of the suspension noise based on a direct application of the Fluctuation-Dissipation theorem. We will explicitly separate the contributions to the thermal noise of the top and the bottom attachment points of the suspension fibers. It has been a common opinion that the top and bottom attachments contribute equally to the thermal noise. We shall challenge this point of view. In fact, we will show that if one shifts the laser beam spot down from the center of the mirror by an appropriately chosen distance h, the contribution of the bottom attachment point to the thermal noise can be reduced by several orders of magnitude. Fig. 3.4 presents plots of this reduction factor in the frequency band 35–100Hz for three different choices of h. What is plotted here is the ratio $S_{\text{bottom}}(f)/S_{\text{top}}(f)$, where $S_{\text{bottom}}(f)$ and $S_{\text{top}}(f)$ are the spectral densities of thermal noise contributed by the bottom and the top attachment points respectively. All three values of h are close to

$$h = \frac{I}{M(R+l)} \tag{3.29}$$

[cf. Eq. (3.42)], where l is the length of the suspension fiber, I is the test-mass moment of inertia for rotation about the center of mass in the plane of Fig. 3.2 (see later), R is the radius of the mirror face and M is the mass of the test mass. The numerical values of these parameters for the initial and enhanced LIGO interferometers are

---

[2]To be specific, we refer to the step 4 of LIGO enhancement — see [2]. In these the suspension thermal noise was calculated assuming the structural damping mechanism. However, the nature of dissipation in fused silica (e.g., viscous vs structural) is not yet fully established for the above frequency bands.

[3]The analysis of this paper is fully applicable to all other Interferometric Gravitational Wave detectors (e.g., VIRGO, GEO-600, TAMA, etc.). For the sake of brevity in this paper we will refer only to LIGO.

$$M = 10\text{kg}, \quad l = 30\text{cm}, \quad R = 12.5\text{cm}, \tag{3.30}$$

$$I = 4.73 \times 10^5 \text{g cm}^2, \quad h = 1.11\text{cm}.$$

Out of the three graphs presented in Fig. 3.4, the one with $h = 1.0$cm seems to be the optimal one. From the graphs we see that reduction factors of $\simeq 10^{-2}$ in the "bottom" component of the thermal noise is possible over the entire band of serious thermal noise: 35 to 100 Hz.

In Sec. 3.2.3 we concentrate on the top attachment point. Lossy defects at the top create noise not only in the test mass motion, but also noise in the motion of the fiber. The latter is significantly larger than the former — by a factor of order $f^2/f^2_{\text{pendulum}}$ at frequencies above the pendulum frequency and below the violin resonances (which are the frequencies of interest for LIGO thermal noise). We show that if one monitors the average horizontal displacement of the suspension fiber of length l, one can essentially record the fluctuating "driving force" originating at the suspension top, and then subtract it from the interferometer's readout, thereby reducing thermal noise originating at the suspension top. The reduction factor in the spectral density of thermal noise is given by $P = 0.93 \cdot l/\lambda$ [cf. Eq(3.54)]. Here

$$\lambda = (d^2/8)\sqrt{\pi E/Mg} \tag{3.31}$$

is the length of the segment of fiber near it's top where the bending is greatest, d is the fiber's diameter, E is the fiber's Young modulus and g is the acceleration of gravity. For a fused silica fiber of diameter $d = 0.6$mm one gets a thermal noise reduction factor of $P \simeq 132$.

We offer a particular way of implementing such a procedure. The basic idea is shown in Fig. 3.6. A fused silica slab is rigidly attached to the "ceiling" (i.e., to the last mass of the seismic isolation stack), and a waveguide ab is carved into the slab's surface. A monochromatic optical wave is set up in the waveguide, and a fused silica fiber used as the suspension fiber is positioned close to the waveguide,
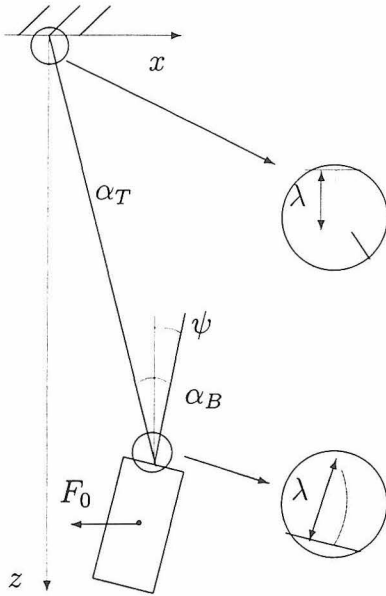
Figure 3.2: **The single-fiber suspension.**
We consider a test mass suspended on a single fiber. The fiber's bottom is attached to the top of the test mass, and the fiber's top is attached to the last stage of the seismic isolation stack. It is assumed that at attachment points the fiber is perpendicular to the surface to which it is attached.

within the optical wave's evanescent field. When the fiber is displaced relative to the waveguide, it will change the optical wave's propagation speed, thus inducing an overall phaseshift of the wave. The detailed calculations in Sec. IIIB show that $\sim 1\text{mW}$ of optical power in the wave is sufficient to reach the required sensitivity.

3.2.2 How to reduce thermal noise originating at the bottom attachment point

The model and formalism   The particular suspension that we consider is sketched in Fig. 3.2. We consider a compact rigid test mass of mass M suspended by a single fiber of length l and mass m; the fiber's bottom end is attached, for concreteness, to the top of the test mass (the main conclusions of this paper are also valid when the test mass is suspended by a fiber loop, as is planned for LIGO). References [3], [4], [5], [7] give detailed explanations of how to use the Fluctuation-Dissipation theorem directly (without normal-mode decomposition) to calculate the spectral density of

thermal noise [4]. In what follows we use the approach elaborated in [7].

To calculate the spectral density $S_x(f)$ of suspension's thermal noise at frequency f we imagine applying an oscillating force F perpendicular to the test mass's mirror surface at the center of the readout laser beam spot [5]:

$$F(t) = F_0 \cos(2\pi f t). \tag{3.32}$$

Then S_x is given by [cf. Eq (3) of [7]]

$$S_x(f) = \frac{2k_B T}{\pi^2 f^2} \frac{W_{\text{diss}}}{F_0^2}, \tag{3.33}$$

where W_{diss} is the average power dissipated in the system (suspension, in our case) when the force $F(t)$ is applied, k_B is Boltzmann's constant and T is the temperature.

For concreteness, assume that the dissipation in the fiber occurs through structural damping (our conclusions will hold equally well for viscous or thermoelastic damping). In this case, the average power dissipated during the oscillatory motion of frequency f is given by [8]

$$W_{\text{diss}} = 2\pi f U_{\text{max}} \phi(f), \tag{3.34}$$

where U_{max} is the energy of the fiber's elastic deformation at a moment when it is maximally bent under the action of the oscillatory force in Eq. (3.32), and $\phi(f)$ is the "loss angle" of the material. The energy of the fiber's elastic deformation is given by

$$U = \frac{JE}{2} \int_0^l dz \, [y'']^2, \tag{3.35}$$

where E is the Young modulus of the fiber material, J is the geometric moment of inertia of the fiber (for a fiber with circular cross section of diameter d one has $J = \pi d^4/64$), z is distance along the fiber with $z = 0$ at the top and $z = l$ at the

---

[4]The original formulation of the Fluctuation-Dissipation theorem is given in [6].

[5]This prescription is only valid when the test masses are perfectly rigid, which is a good approximation when dealing with suspension thermal noise. The case when the test masses are no longer considered to be rigid (e.g., for an internal thermal noise calculations) is treated in detail in [7]. In that case the force $F(t)$ must be spread out over the laser beam spot instead of applied to its center point.
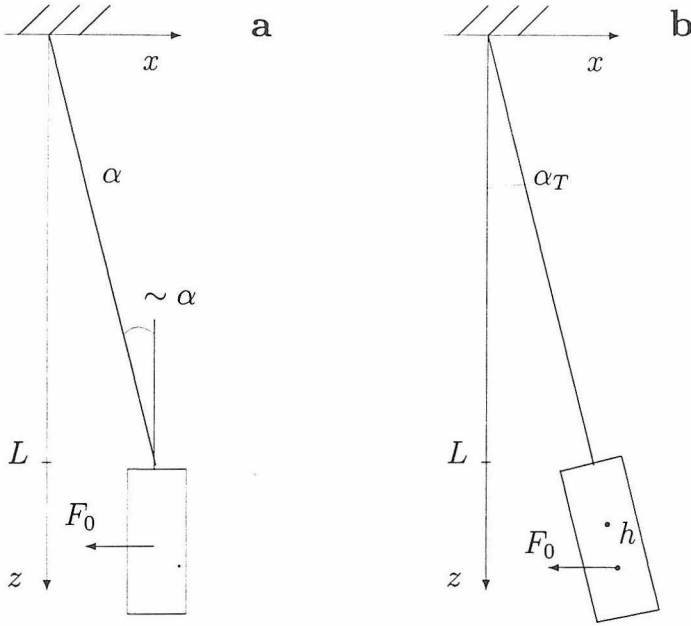
Figure 3.3: **Periodically driven test mass and suspension fiber.**
Motion of the test mass and the suspension fiber under the action of an oscillating force applied at the center of the laser beam spot in two different cases: *a)* the beam spot is positioned at the mirror center, the fiber bends equally at the top and the bottom, and *b)* the position of the beam spot is shifted down from the center of the mirror, so that there is no bending of the fiber at the bottom.

bottom, and $y(z)$ is the fiber's horizontal displacement from a vertical line.

This method of calculating thermal noise is useful for a qualitative analysis of the system, as well as quantitative analysis. In particular, it allows one to see which part of the suspension fiber contributes the most to the thermal noise. Assume, for a start, that the laser beam is positioned exactly in the middle of the mirror. Then to work out the thermal noise one has to imagine applying the oscillating force F in Eq. (3.32) to the mirror center; the motion of the fiber and the mirror under the action of the force are shown in Fig. 3.3a. Here we assume that the detection frequency f (and hence the frequency of the applied force) satisfies $f_p, f_r << f << f_v$, where f_p, f_r, f_v are the frequencies of the pendulum, rocking and first violin mode respectively (this condition implies that horizontal and rotational motion of the test mass is not affected by the presence of the fiber, and that the fiber itself remains straight).

From Fig. 3.3a it is clear that the fiber bends equally at the top and the bottom

(we always assume that at the attachment point the fiber has to be normal to the surface to which it is attached). The total energy of elastic deformation is

$$U_0 = \frac{1}{2} M g \lambda \alpha^2 = \frac{M g \lambda}{2} \left(\frac{F}{M \omega^2 l} \right)^2,$$ (3.36)

where $\lambda = \sqrt{JE/Mg}$ is the characteristic length over which the fiber is bent near the attachment points, $\omega = 2\pi f$ is the angular frequency of detection, and α is the angle between the straight part of the fiber and the vertical.

The bending of the fiber at the bottom can be avoided if one applies the force F in Eq. (3.32) not at the middle of the mirror, but at some distance h below the center. In particular, we should choose h so that the mirror itself rotates by the same angle as the fiber under the action of the applied force; the resulting motion is shown on Fig. 3.3b. Physically this means that if we position our laser beam at a distance h below the mirror center, then the bottom attachment point will not contribute to the thermal noise when h is carefully chosen. This means that the overall suspension noise will be reduced by a factor of order 2 (in fact, more precisely, by a factor of $2(1 + R/l)$, where R is the radius of the mirror and l is the length of the string, — see later in this section).

In the rest of this section and Appendix A we find the general expression for the suspension thermal noise, and we then work out the optimal h for the frequency band of interest for LIGO. We will assume that when a periodic oscillation of frequency f is induced in the system, the average power dissipated as heat in the suspension is given by

$$W_{\text{diss}} = f \left[\zeta_{\text{top}}(f) \bar{\alpha}_{\text{T}}^2 + \zeta_{\text{bottom}}(f) \bar{\alpha}_{\text{B}}^2 \right].$$ (3.37)

Here $\bar{\alpha}_{\text{T}}$ and $\bar{\alpha}_{\text{B}}$ are the amplitudes of oscillations of the angles α_{T} and α_{B} respectively (see Fig. 3.2), and ζ_{top} and ζ_{bottom} are frequency-dependent quantities characterizing dissipation at the top and the bottom respectively. For the case of structural damping

$$\zeta_{\text{top}} = \zeta_{\text{bottom}} = \pi f \phi(f) M g \lambda,$$ (3.38)

where λ is given by Eq. (3.31) of the introduction.

To compute W_{diss} we need to evaluate $\bar{\alpha}_{\mathrm{T}}$ and $\bar{\alpha}_{\mathrm{B}}$ by analyzing the dynamics of the oscillations. This is done in Appendix A, see Eqs. (3.68) and (3.67). Putting these equations into Eq. (3.37) and then into Eq. (3.33), we obtain [cf. Eq. (3.69)]

$$
\begin{aligned}
S_{\mathrm{x}}(f) \;=\; & \frac{8k_{\mathrm{B}}T}{\omega^2} \left\{ \frac{I/M - R(g/\omega^2 + h)}{[Ig - MgR\,(g/\omega^2 - R)]\cos(kl) - (I\omega^2 - MgR)\sin(kl)/k} \right\}^2 \\
& \times \left\{ \zeta_{\mathrm{top}} + \zeta_{\mathrm{bottom}}\cos^2(kl) \left[\frac{I/M - h\,[R + \tan(kl)/k - g/\omega^2]}{I/M - R(g/\omega^2 + h)} \right]^2 \right\} .
\end{aligned} \quad (3.39)
$$

Here $k = \omega/c = 2\pi f/c$, $c = \sqrt{glM/m}$ is the speed of propagation of a transverse wave in the fiber. From the above equation we can infer the ratio of the bottom and the top contributions to the thermal noise:

$$
\frac{S_{\mathrm{bottom}}(f)}{S_{\mathrm{top}}(f)} = \frac{\zeta_{\mathrm{bottom}}(f)}{\zeta_{\mathrm{top}}(f)} \cos^2(kl) \left[\frac{I/M - h\,[R + \tan(kl)/k - g/\omega^2]}{I/M - R(g/\omega^2 + h)} \right]^2 . \quad (3.40)
$$

This is the most important equation in this section of the paper; it will be discussed in the next subsection.

The case of low-frequency suspension noise When the detection frequency f is far below the frequency of the fundamental violin mode, f_{v}, then $kl \ll 1$ in Eq. (3.40) and

$$
\frac{\tan(kl)}{k} \simeq l \left[1 + \frac{1}{3}(kl)^2 \right]. \quad (3.41)
$$

Let us assume that the top and the bottom are equally lossy, i.e., $\zeta_{\mathrm{top}} = \zeta_{\mathrm{bottom}}$, as the would be for structural damping, Eq. (3.38) above. We choose h to be

$$
h = \frac{I}{M(R+l)}. \quad (3.42)
$$

Putting Eqs. (3.42) and (3.41) into Eq. (3.40), we get

$$
\frac{S_{\mathrm{bottom}}(f)}{S_{\mathrm{top}}(f)} \simeq \frac{\pi^4}{9} \frac{1}{\left[1 - (R/h)(\omega_p^2/\omega^2)\right]^2} \left(\frac{f}{f_{\mathrm{v}}}\right)^4, \quad (3.43)
$$
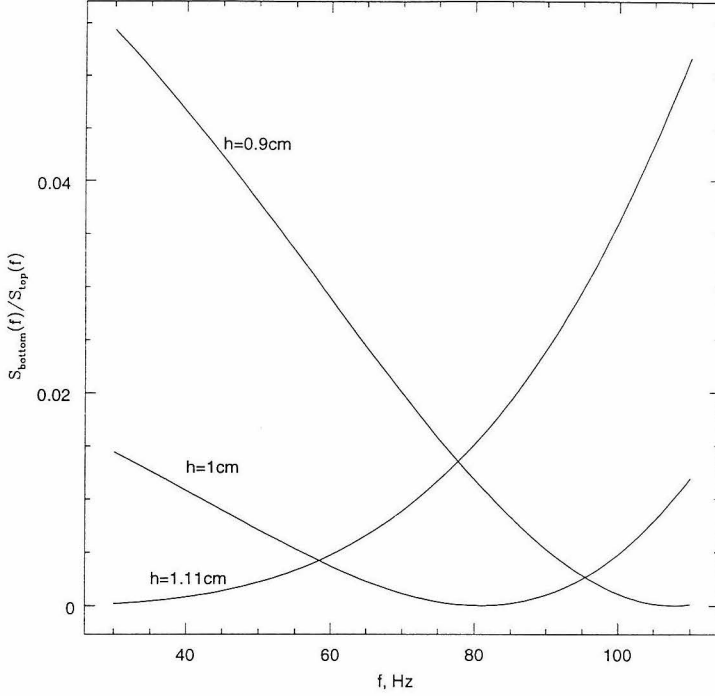
Figure 3.4: **A plot of $S_{\text{bottom}}(f)/S_{\text{top}}(f)$ as a function of frequency f for three different positions of the laser beam spot.**

where $\omega_p = \sqrt{g/l}$.

For the initial and enhanced LIGO design $f_v \simeq 400\text{Hz}$, $M \simeq 10\text{kg}$, $I \simeq 4.73 \times 10^{-2}\text{kg} \times \text{m}^2$, $R \simeq 12.5\text{cm}$, and the interesting frequency range where suspension noise is expected to dominate is $35 - 100\text{Hz}$ (actually, this depends on the stage of enhancement. The frequency band specified above is where the suspension thermal noise is expected to dominate in the initial LIGO; in the enhanced version this frequency interval will be larger). In this case Eq. (3.43) gives $S_{\text{bottom}}(f)/S_{\text{top}}(f) \simeq 0.002 - 0.2$.

In Fig. 3.4 we give plots for $S_{\text{bottom}}/S_{\text{top}}$ as a function of the detection frequency f for three different choices of h. We have used Eq. (3.43) to make all the plots and we set I, M, R and l to the numerical values appropriate for the initial and enhanced LIGO design and given at the beginning of this section.

The first curve is plotted for h given by Eq. (3.42), in our case $h = 1.11\text{cm}$. The second and third curves are for $h = 1.0\text{cm}$ and $h = 0.9\text{cm}$; these values of h are chosen so that $S_{\text{bottom}}/S_{\text{top}} = 0$ for $f = 80\text{Hz}$ and $f = 105\text{Hz}$ respectively. Out of

the three cases the choice $h = 1$cm gives the best overall performance across the considered frequency band, with the typical reduction factor of

$$\frac{S_{\text{bottom}}}{S_{\text{top}}} \sim 10^{-2}. \tag{3.44}$$

From Eq. (3.39) we see that choosing h close to the value in Eq. (3.42) reduces the total suspension thermal noise by a factor close to $2(1 + R/l) \sim 3$ relative to the case when $h = 0$.

High-frequency suspension thermal noise A somewhat less interesting observation is that for $h = 0$ and $f_n = f_v(n + 1/2)$, where n is an integer,

$$\frac{S_{\text{bottom}}(f_n)}{S_{\text{top}}(f_n)} = 0. \tag{3.45}$$

Unfortunately, at $f = f_n$ the interferometer's noise is dominated by shot noise. However, if one uses an advanced optical topology — for example, resonant sideband extraction — then it is possible to reduce the shot noise in a narrow band around any chosen frequency. Then the thermal noise may dominate in this narrow band, and our observation (3.45) may be useful in case one tries to reduce the thermal noise by cooling of the fiber top.

3.2.3 How to control noise from the top

The concept In this section we propose a recipe for how to decrease the influence of the thermally fluctuating stress at the top part of the suspension fiber. The basic idea is the following:

Intuitively, the fluctuations at the top cause bending of the fiber at the top, which will be a random process in time. This random bending will randomly move the rest of the fiber and ultimately drive the random motion of the test mass. We propose to measure directly the thermally driven fluctuations in the horizontal displacement of the fiber, and from them infer the fluctuating force which drives the random motion

of the mirror. We can then subtract the motion due to this fluctuating force from the interferometer output[6].

Formally this amounts to introducing a new readout variable q as follows:

$$q = X_{\text{mirror}} + X_{\text{fiber}}. \tag{3.46}$$

Here X_{mirror} is the horizontal displacement of the laser spot's center (i.e. the signal ultimately read by the interferometer's photodiode), and

$$X_{\text{fiber}} = \int_0^l dz \Phi(z) y(z) \tag{3.47}$$

is the fiber's horizontal displacement weighted by some function $\Phi(z)$ to be discussed below. We will postpone the discussion of how to measure q experimentally until the next section; here we concentrate on finding the optimal $\Phi(z)$ and seeing what is the maximal possible reduction in the thermal noise.

To find the spectral density of fluctuations in q we need to imagine acting on the system with sinusoidal force $F_q \propto \cos(2\pi f t)$ that appears in the interaction hamiltonian in the following way

$$H_{\text{int}} = -q F_q = -X_{\text{mirror}} F_q - \int_0^l dz F_q \Phi(z) y(z); \tag{3.48}$$

cf. the discussion of the Fluctuation-Dissipation theorem in Ref. [7]. From the Eq. (3.48) we observe that applying the generalized force F_q to the system is equivalent to applying two forces simultaneously: one is a force of magnitude F_q applied to the mirror surface at the center of the beam spot, and the other is a force distributed along the fiber in the following manner:

$$\frac{dF_{\text{fiber}}}{dz} = F_q \Phi(z). \tag{3.49}$$

The resulting motion of the system is shown in Fig. 3.5. The intuitive idea is to

---

[6]The idea of thermal noise compensation is not new (e.g., [11], [10]). However, our detailed treatment and concrete experimental proposal is different from anything prior to this paper.
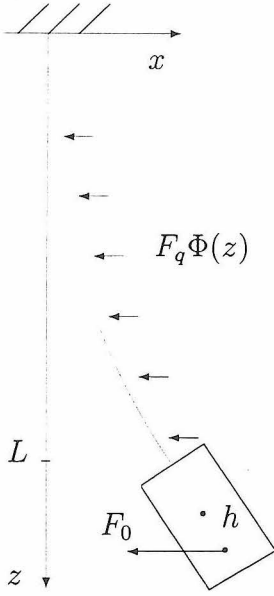
Figure 3.5: **Motion of the test mass and suspension fiber under the action of the generalized force F_q defined in Eq. (3.48) of the text.**
The force F_q should be chosen so that there is no bending of the fiber at it's top and bottom attachment points.

choose the weighting function $\Phi(z)$ so that when the beam spot's height h has also been appropriately chosen, F_q induces no bending of the fiber at the top or at the bottom.

In the case of structural damping the dissipated power is proportional to the elastic energy U of the fiber. Thus formally one has to choose $\Phi(z)$ and h so that U is minimized. It is convenient to reformulate the problem: to find the shape of the fiber $y(z)$ and beam-spot height h for which the functional in Eq. (3.35) has a minimum, and after this calculate the distribution $\Phi(z)$ of the driving force on the fiber that will produce the desired shape $y(z)$. In Appendix B we carry out this straightforward but somewhat tedious task. We obtain [cf. Eq. (3.78)]

$$
\begin{aligned}
y_{\text{optimal}}(z) &= \frac{F_q}{M\omega^2}\left(\frac{z}{l}\right)^2\left(\frac{3(r+1)-z/l}{2(3r^2+3r+1)}\right) \\
&\simeq \frac{F_q}{M\omega^2}\left(\frac{z}{l}\right)^2\left(0.76-0.18\frac{z}{l}\right).
\end{aligned}
\tag{3.50}
$$

Here $r = R/l$, R is the radius of the mirror, l is the length of the fiber, $\omega = 2\pi f$ is the

angular frequency of detection. We substitute here and below $r = 0.42$ corresponding to the initial and enhanced LIGO test masses. The profile of the distributed force acting on the fiber and hence of $\Phi(z)$ is mainly determined by $y''(z)$ (see Appendix B):

$$\Phi(z) \simeq \Phi_0 = -\frac{Mg}{F_q} y''(z), \tag{3.51}$$

which gives [cf. Eq. (3.81)]

$$\begin{aligned} \Phi_0(z) &\simeq -\frac{\omega_p^2}{\omega^2 l} \left(1 + r - \frac{z}{l}\right) \frac{3}{3r^2 + 3r + 1} \\ &= -\frac{\omega_p^2}{\omega^2 l} \left(1.53 - 1.08\frac{z}{l}\right), \end{aligned} \tag{3.52}$$

where $\omega_p = \sqrt{g/l}$. When the force distribution has this optimal form, the elastic energy has the minimum value

$$\begin{aligned} U_{\min} &\simeq \frac{3}{3r^2 + 3r + 1} \frac{\lambda}{l} \frac{Mg\lambda}{2} \left(\frac{F_q}{M\omega^2 l}\right)^2 \\ &= \frac{1.08\lambda}{l} \times U_0, \end{aligned} \tag{3.53}$$

where U_0 is the elastic energy in Eq. (3.36). Therefore, for a fused silica fiber with $E \simeq 6.9 \times 10^{10}$Pa and $d = 0.6$mm, we get $\lambda \simeq 2.1$mm and the maximal reduction factor for the spectral density of suspension thermal noise is

$$P = \frac{l}{1.08\lambda} \simeq 132. \tag{3.54}$$

Experimental realization: preliminary remarks. Before describing a particular experimental realization of the above scheme, a few general remarks are in order.

First, one might worry that our averaging function $\Phi(z)$ is frequency dependent — in general, that could make the experimental implementation very difficult. In particular [see Appendix B, Eq. (3.80)], Φ consists of two components: $\Phi = \Phi_0 + \Phi_1$, where Φ_0 and Φ_1 as given by Eq. (3.80) have very different frequency dependence. However at the frequencies of interest $\Phi_0 \gg \Phi_1$, and then the approximate formula

(3.52) for the averaging function $\Phi(z) = \Phi_0(z)$ is a product of two terms: one which depends only on the frequency f (i.e. $\Phi(z) \propto 1/f^2$), and the other which depends only on the coordinate z. This feature makes the scheme feasible for a broad range of frequencies. It is sufficient that our device measures the displacement of the fiber with the frequency-independent averaging function $\tilde{\Phi}(z) \propto f^2 \times \Phi(z)$, and that the frequency dependence is then put back in during data analysis when constructing the readout variable q:

$$q = X_{\mathrm{mirror}} + \eta(f) \int_0^l dz \tilde{\Phi}(z) y(z), \tag{3.55}$$

where $\eta(f) \propto f^{-2}$ is chosen so that $\eta\tilde{\Phi} = \Phi$.

As mentioned above, Eq. (3.52) is an approximation valid when the fiber has no inertia, i.e. when $f \ll f_v =$ (lowest violin-mode frequency). When the inertia of the fiber becomes important ($\Phi_1 \sim \Phi_0$), it is no longer possible to factor out a frequency-dependent part of Φ. As a result, when f gets closer to f_v, the effectiveness of the thermal noise suppression (i.e., the value of P) is reduced. A detailed analysis shows that if we choose $\tilde{\Phi}(z)$ so that the thermal noise compensation is optimal ($P = P_{\mathrm{max}}$) at low frequencies $f \ll f_v$, then at $f = 0.2 f_v$ we have $P \sim 0.9 P_{\mathrm{max}}$, at $f = 0.32 f_v$ we have $P \sim 0.5 P_{\mathrm{max}}$, and beyond this P is reduced sharply as we approach the first violin mode. For the fused silica fiber discussed above $f_v \sim 400 \mathrm{Hz}$, so the compensation is effective throughout the band $35 - 100 \mathrm{Hz}$ where suspension thermal noise dominates. It is worth emphasizing that this deterioration in the reduction factor only happens when we use the averaging function Φ_0 instead of $\Phi_0 + \Phi_1$ close to the violin frequency. Thus, this limitation is one of technology and not of principle. Perhaps, it is possible to conceive of a scheme where the correct averaging function is implemented at all frequencies. However, we have not been able to do so.

Secondly, any sensor used for monitoring the fiber coordinate X_{fiber} will have an intrinsic noise which will deteriorate the quality of the thermal-noise compensation. In particular, the overall reduction factor P_{eff} is given by

$$\frac{1}{P_{\mathrm{eff}}} = \frac{1}{P} + \frac{S_{\mathrm{fiber\ meas}}(f)}{S_{\mathrm{fiber\ therm}}(f)}, \tag{3.56}$$

where $S_{\text{fiber meas}}(f)$ is the spectral density of intrinsic noise of the device which measures the average displacement of the fiber and $S_{\text{fiber therm}}(f)$ is the spectral density of thermal fluctuations of the same displacement.

For the case of structural damping it is easy to estimate

$$\sqrt{S_{X \text{ fiber therm}}(f)f} \sim \sqrt{\frac{\lambda\phi kT}{Mg}} \sim 10^{-14}\text{cm}, \qquad (3.57)$$

where we assume that $\phi \sim 10^{-7}$ for fused silica. If our goal is to achieve $P \sim 100$ then the condition $P_{\text{eff}} \simeq P$ implies

$$\sqrt{S_{\text{fiber meas}}f} << \sqrt{\frac{S_{\text{fiber therm}}f}{P}} \sim 10^{-15}\text{cm}. \qquad (3.58)$$

We shall take the above number as a sensitivity goal that our measuring device should achieve.

Experimental realization: proposed measuring device Now we are ready to describe a possible practical implementation of our thermal-noise compensation scheme. Figure 3.6 illustrates the basic idea. We propose to use a fused silica optical fiber with the refractive index n_1 for the test mass's suspension. Next to this fiber we attach to the top seismic isolation plate (i.e., the "ceiling") a rigid block of the fused silica A with the same index of refraction n_1. On the surface of this rigid block we put a thin optical waveguide with refractive index n_2 such that $n_2 > n_1$, so that the waveguide is at a distance $\sim \lambda_{\text{optical}}/2\pi$ from the suspension fiber. It is assumed that the side of the waveguide close to the suspension fiber does not have any coating, i.e., it is "naked." In this configuration the optical wave may propagate through the waveguide without substantial scattering even though the suspension fiber is within the wave's evanescent zone. This device will produce a relatively large response to the displacement X_{fiber} in the form of a phaseshift of $\Delta\phi$ of the optical wave:

$$\Delta\phi = K\frac{2\pi X_{\text{fiber}}}{\lambda_{\text{optical}}}\frac{2\pi l}{\lambda_{\text{optical}}}, \qquad (3.59)$$
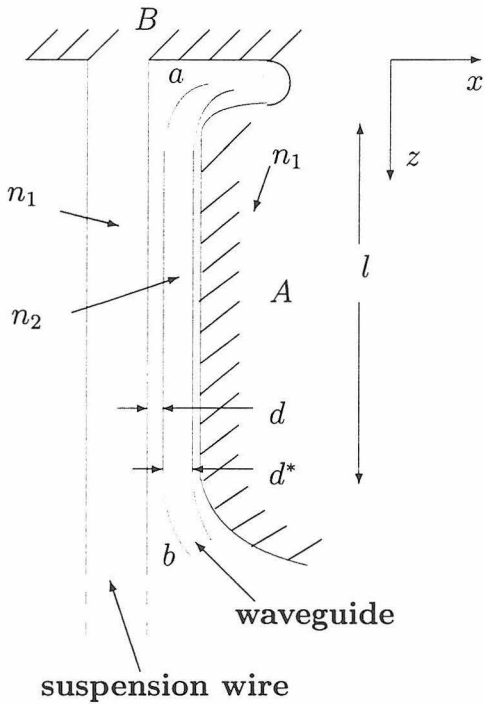
Figure 3.6: **A proposed scheme for compensation of the suspension thermal noise.**
The optical waveguide ab is positioned close to the suspension fiber made of fused silica. A horizontal displacement of the suspension fiber is recorded through a phase shift of an optical wave propagating through the waveguide.

where the dimensionless factor K depends on the values of n_1 and n_2 and for typical optical waveguides is $K \sim 10^{-3}$. Equation (3.59) implies that in order to register $X_{\text{fiber}} \sim 10^{-15}$cm we need a sensitivity $\Delta\phi \sim 10^{-7}$. Thus for averaging time of $\tau_{\text{grav}} = 0.01$sec we need to use the power of coherent light of $W \sim 1$mW. This power can be decreased if one uses a resonant standing wave in the waveguide.

Apart from the shot noise of the laser light, let us briefly discuss two other kinds of noise in this sensor. A more complete discussion will be presented elsewhere.

The first kind is seismic noise. A simple calculation shows that the seismic contribution to the noise in the readout variable q is about twice as large in spectral density as the seismic contribution to the noise in X_{mirror}. Thus the seismic noise will not be an issue at frequencies above the "seismic wall" of the LIGO sensitivity curve.

The second kind of noise we want to mention is the mechanical thermal fluctuations of the waveguide itself. Our estimates show that if these fluctuations are caused by structural damping (and not by some surface or contact defects), then the ratio of the mechanical thermal fluctuations of the waveguide to those of the fiber is

$$\frac{S_{\text{waveguide}}}{S_{\text{fiber}}} \sim \frac{Mg}{El\lambda} \sim 10^{-5}. \tag{3.60}$$

Thus, if the system is sufficiently clean then the mechanical thermal fluctuations of the waveguide will probably not significantly reduce the sensitivity of our sensor.

It is worth noting that in order to achieve the optimal compensation of thermal noise, the distance $d(z)$ between the suspension fiber and the waveguide has to vary in accord with the optimal profile of the averaging function:

$$d = A - B \log\left[\Phi(z)\right], \tag{3.61}$$

where A and B are constants to be discussed elsewhere. In this case the phase of the waveguide's output records the optimally averaged coordinate X_{fiber} of the fiber.

The profile $d(z)$ may be difficult for experimental realization. However, we find that in the simplest case when $\Phi(z)$ is a constant over the length l of averaging, the

factor P is reduced very little: from $P = 132$ to $P \sim 120$.

3.2.4   Conclusions

In this paper we have done two things.

Firstly, we have shown that by an appropriate positioning of the laser's beam spot on the surface of each test-mass mirror, one can reduce the contribution of the suspension fiber's bottom to the suspension thermal noise by two to three orders of magnitude in the frequency band of $35 - 100$Hz for the initial LIGO design.

Secondly, we have proposed a way to compensate the suspension thermal noise originating from the top of each fiber by monitoring independently the fiber's random horizontal displacement. In the best case, with the system parameters for the initial or enhanced LIGO design, one can get a reduction factor of the order of $P = 130$ in spectral density over the entire $35 - 100$Hz band, when both the first and second procedures are applied; and with realistic defects in the design one should be able to get a reduction of at least $P \simeq 100$.

The device that compensates the suspension thermal noise can ease the requirements to quality of suspension system. In particular, if this device allows the reduction factor of $P = 100$, this would effectively increase the quality factors of pendulum and violin modes by a factor of $P = 100$. So far the highest quality factor $Q \simeq 10^8$ of the pendulum mode was achieved in [9] for a fused silica suspension fiber, which allows one to reach the Standard Quantum Limit for averaging time of 10^{-3}sec. Implementation of our proposal could effectively increase this quality factor to $Q_{\text{eff}} \simeq 10^{10}$, which would reduce the thermal noise in LIGO to the level of Standard Quantum Limit for averaging time of 10^{-2}sec. Then the techniques which allow one to beat the Standard Quantum Limit (see, e.g., [13]) could be used in the enhanced LIGO interferometers.

Acknowledgments

3.2.5 Appendix A: Motion of the periodically driven suspension fiber

In this appendix we solve the dynamical problem of finding the amplitudes $\bar{\alpha}_T$ and $\bar{\alpha}_B$ of oscillation of the top and bottom bending angles in Eq. (3.37) when a periodic force

$$F = F_0 \cos(\omega t) \tag{3.62}$$

is applied to the mirror at a distance h below the mirror center [we use these amplitudes in Eq. (3.37) of the text]. For convenience we complexify all of the quantities:

$$F = F_0 e^{\imath \omega t}, \quad \alpha_T = \bar{\alpha}_T e^{\imath \omega t}, \quad \alpha_B = \bar{\alpha}_B e^{\imath \omega t},$$

$$x = \bar{x} e^{\imath \omega t}, \quad \psi = \bar{\psi} e^{\imath \omega t},$$

where x is the displacement of the test mass's center of mass and ψ is the angle by which the mirror is rotated (see Fig. 3.2) under the action of the force $F(t)$. As usual, $\omega = 2\pi f$ is the angular frequency.

From the projection of the Newton's Second Law on the horizontal axis we have

$$F_0 - (\bar{\alpha}_B - \bar{\psi})Mg = -M\omega^2 \bar{x}, \tag{3.63}$$

and, for the rotational degree of freedom, the equation of motion is

$$F_0 h + MgR\bar{\alpha}_B = I\omega^2 \bar{\psi}, \tag{3.64}$$

where R is the radius of the test-mass cylinder and I is the moment of inertia for rotation about the test-mass center of mass in the plane of the Fig. 3.2. In the two equations above we assume that α_B and ψ are small.

The fiber's horizontal displacement y from a vertical line approximately satisfies the wave equation:

$$\frac{\partial^2 y}{\partial t^2} = c^2 \frac{\partial^2 y}{\partial z^2}, \tag{3.65}$$

where z is distance along the wire, with $z = 0$ at the top and $z = l$ at the bottom, and $c = \sqrt{glM/m}$ is the transverse speed of sound in the wire. In this Appendix we use Eq. (3.65) for flexible wire since it's solutions are simple. If one takes the stiffness into account this changes the solutions of Eq. (3.65) by a relative order of λ/l, see e.g. [12]. However, when using Eq. (3.65), we must allow non-zero bending angles at the top and bottom attachment points, α_T and α_B. The energy of elastic strain of the wire then consists of two components: one from the bulk of the wire given by Eq. (3.35), and the other from the bending at the attachment points given by Eq. (3.36). The solution to Eq. (3.65) is

$$y(z,t) = A \sin(kz) e^{i\omega t}, \tag{3.66}$$

where $k = \omega/c$ is the wave vector of an off-resonance standing wave induced in the fiber and A is a constant. The boundary condition is set at the bottom by

$$
\begin{aligned}
A \sin(kl) &= \bar{x} + R\bar{\psi} \\
kA \cos(kl) &= \left(\bar{\alpha}_B - \bar{\psi}\right).
\end{aligned}
$$

Putting these two equations into Eqs. (3.63) and (3.64), we find

$$\bar{\alpha}_{\mathrm{B}} = -F_0 \frac{I/M - h\left[R + \tan\left(kl\right)/k - g/\omega^2\right]}{MgR^2 + \left(I\omega^2 - MgR\right)\left[g/\omega^2 - \tan\left(kl\right)/k\right]} \tag{3.67}$$

and

$$\bar{\alpha}_{\mathrm{T}} = -F_0 \frac{I/M - R(g/\omega^2 + h)}{\left[Ig - MgR\left(g/\omega^2 - R\right)\right]\cos(kl) - \left(I\omega^2 - MgR\right)\sin(kl)/k}. \tag{3.68}$$

Putting Eqs. (3.67), (3.68) and (3.37) into Eq. (3.33), we finally get for the spectral density of the suspension thermal noise:

$$\begin{aligned}
S_{\mathrm{x}}(f) \;=\; & \frac{8k_{\mathrm{B}}T}{\omega^2} \left\{ \frac{I/M - R(g/\omega^2 + h)}{\left[Ig - MgR\left(g/\omega^2 - R\right)\right]\cos(kl) - \left(I\omega^2 - MgR\right)\sin(kl)/k} \right\}^2 \\
& \left\{ \zeta_{\mathrm{top}} + \zeta_{\mathrm{bottom}}\cos^2(kl)\left[\frac{I/M - h\left[R + \tan\left(kl\right)/k - g/\omega^2\right]}{I/M - R(g/\omega^2 + h)} \right]^2 \right\}.
\end{aligned} \tag{3.69}$$

3.2.6   Appendix B: Calculation of the optimal detection strategy

Here we calculate the optimal shape $y_{\mathrm{optimal}}(z)$ of the fiber and the vertical position of the laser beam spot h that minimize the fiber's elastic deformation energy [Eq. (3.35)].

It is easy to deduce from Eq. (3.35) that energy minimizing function $y(z)$ obeys the equation $y''''(z) = 0$. Therefore,

$$\frac{y(z)}{l} = a_0 + a_1\frac{z}{l} + a_2\frac{z^2}{l^2} + a_3\frac{z^3}{l^3}, \tag{3.70}$$

where a_i are constants to be determined.

Let us discuss the boundary conditions. Strictly speaking, the boundary conditions should be such that the fiber is perpendicular to the surface of attachment at both the top and the bottom. Therefore, at the top we have $y(0) = y'(0) = 0$, from which immediately follows $a_0 = a_1 = 0$. However, at the bottom it is more convenient for our calculations embody the bending of the fiber, on the lengthscale λ, in a

bending angle α_B as in Fig. 1, and correspondingly add an additional term

$$U_{\text{add}} = (1/4)Mg\lambda\alpha_B^2 \tag{3.71}$$

to the energy functional in Eq. (3.35), and then in Eq. (3.70) evaluate $y(l)$ and it's derivatives above the λ-scale bend. Our energy minimization procedure will make the angle α_B so small that the additional elastic energy as given by Eq. (3.71) is negligible compared to U in Eq. (3.35)

The coefficients a_2 and a_3 can be inferred from force and torque balance at the test mass:

$$F_q - Mgy'(l) = -M\omega^2(y(l) + R(y'(l) + \alpha_B)), \tag{3.72}$$

and

$$F_q h - MgR\alpha_B = -I\omega^2(y'(l) + \alpha_B).$$

It is useful to rewrite these equations in a dimensionless form:

$$\begin{aligned}
\xi(1 + \eta(r - a)) \quad + \quad r\alpha_B &= -\xi_0, \\
\eta\xi \quad + \quad \alpha_B(1 - \mu ra) &= -\mu s\xi_0;
\end{aligned} \tag{3.73}$$

where

$$\xi = \frac{y(l)}{l}, \quad \eta = \frac{y'(l)l}{y(l)}, \quad s = \frac{h}{l},$$

$$a = \frac{\omega_p^2}{\omega^2} \simeq 10^{-3} \div 10^{-6}, \quad r = 0.42, \quad \mu = \frac{Ml^2}{I} = 19,$$

where $\omega_p = \sqrt{g/l}$. Here we have used for estimates the mirror parameters for the initial and enhanced LIGO interferometers. Solving the above system of equations (3.73) for ξ and α_B (taking η as a parameter), we get:

$$\alpha_B = \xi_0 \frac{\eta - \mu s(1 + \eta(r - a))}{[1 + \eta(r - a)][1 - \mu ra] - r\eta} \simeq \xi_0[\eta - \mu s(1 + \eta(r - a))]$$

$$\xi = -\xi_0 \frac{1 - \mu r(a + s)}{[1 + \eta(r - a)][1 - \mu r a] - r\eta} \simeq -\xi_0(1 - \mu r(a + s))$$

Let us choose the parameter s so that $\alpha_{\mathrm{B}} = 0$ for some angular frequency ω_0 in the frequency band $35 - 100\mathrm{Hz}$ where thermal noise is most serious:

$$s \simeq \frac{\eta}{\mu[1 + \eta(r - a_0)]} \simeq \frac{\eta}{\mu[1 + \eta r]}, \quad a_0 = \frac{\omega_p^2}{\omega_0^2} \tag{3.74}$$

Then we get for α_{B} and ξ

$$\alpha_{\mathrm{B}} \simeq \xi_0 \frac{\eta^2}{1 + \eta r}(a - a_0) \tag{3.75}$$

$$\xi \simeq -\xi_0 \frac{1}{1 + \eta r}.$$

We can express the coefficients a_3 and a_2 in terms of ξ and η by combining Eqs. (3.70) and (3.73), and we can then calculate the elastic energy according to Eq. (3.35):

$$U \simeq \frac{Mg\lambda}{2}\left(\frac{F_q}{M\omega^2 l}\right)^2 \times \frac{\lambda}{l} \times \frac{4(\eta^2 - 3\eta + 3)}{(1 + r\eta)^2} \tag{3.76}$$

This function has the minimal value

$$U_{\min} \simeq \frac{l}{\lambda} \times \frac{3}{1 + 3r + 3r^2} \times U_0 = \frac{1.08\lambda}{l} \times U_0$$

at optimal η given by

$$\eta_{\mathrm{opt}} = \frac{3(1 + 2r)}{2 + 3r} = 1.69. \tag{3.77}$$

Here U_0 is the energy of elastic strain of the fiber when the force of magnitude F_q is applied in mirror center, as worked out in Eq. (3.36). Now we can figure out the optimal shape of the fiber's horizontal displacement:

$$\begin{aligned} y_{\mathrm{optimal}}(z) &= \frac{F_q}{M\omega^2}\left(\frac{z}{l}\right)^2\left(\frac{3(r + 1) - z/l}{2(3r^2 + 3r + 1)}\right) \\ &\simeq \frac{F_q}{M\omega^2}\left(\frac{z}{l}\right)^2\left(0.76 - 0.18\frac{z}{l}\right). \end{aligned} \tag{3.78}$$

From Eq. (3.74) we get $h = l \times s \simeq 1.55\mathrm{cm}$.

Using (3.75) one can show that $\alpha_{\mathrm{B}} \leq 1.7 \cdot 10^{-3} \cdot \xi_0$ over the frequency band

$35 - 100$Hz. From this and Eq. (3.71), one can compute the energy due to the bending at the fiber bottom: $U_{add} \simeq 1.4 \cdot 10^{-6} \times E_0$. We see that $U_{add} \ll U_{min}$ and hence over the frequency band of interest the small bending at the bottom does not contribute significantly to the total energy of elastic deformation.

The profile of the distributed force and correspondingly the function Φ are given by

$$F_q \Phi(z) = -\rho \omega^2 y(z) - Mg y''(z) + IE y''''(z).$$ (3.79)

Here ρ is the fiber density per unit length. Since $y''''(z) = 0$, the function Φ consists of two terms $\Phi(z) = \Phi_0(z) + \Phi_1(z)$, where

$$\Phi_0(z) = -\frac{Mg}{F_q} y''(z), \quad \Phi_1(z) = -\frac{\rho \omega^2}{F_q} y(z).$$ (3.80)

$$\Phi_0(z) = \frac{\omega_p^2}{l\omega^2} \cdot \left(1 + r - \frac{z}{l}\right) \cdot \frac{3}{3r^2 + 3r + 1} = \frac{\omega_p^2}{l\omega^2} \cdot \left(1.53 - 1.08\frac{z}{l}\right).$$ (3.81)

We see that Φ_0 is much greater than Φ_1 in our frequency range ($10 - 100$Hz for the initial LIGO).

Bibliography

[1] A. Abramovici *et al.*, Science, **256**, 325 (1992); C. Baradaschia *et al.*, Nucl. Instrum & Methods, **A289**, 518 (1990).

[2] B. Barish *et al.*, "LIGO advanced Research and Development Program Proposal", LIGO technical document LIGO-M970107-00-M (Caltech, 1996).

[3] G. I. Gonzalez and P. R. Saulson, *J. Accoust. Soc. Am*, **96**, 207-212 (1994).

[4] N. Nakagawa *et al.*, *Rev. Sci. Instrum.* **68(9)**, 1-4 (1997).

[5] A. V. Gusev *et al.*, *Radiotekhnika i Elektronika*, **40**, 1353-1359 (1995).

[6] H. B. Callen and T. A. Welton, *Phys. Rev.* **83**, 3 4-50 (1951).

[7] Yu. Levin, *Phys. Rev. D*, **57**, 659-663 (1998).

[8] P. R. Saulson, *Phys. Rev. D*, **42**, 2437-2445 (1990).

[9] V. B. Braginsky, V. P. Mitrofanov, K. V. Tokmakov, *Phys. Lett. A*, **218**, 164-166 (1996) and references therein.

[10] V. V. Kulagin, First E. Amaldi conference on grav. wave experiments, editors E. Coccia, G. Pizzella, F. Ronga, World Sci. Publ. Comp., 1995, p. 328.

[11] Remarks by R. Weiss and others in informal LIGO team discussions.

[12] L. D. Landau and E. M. Lifschitz, *Theory of Elasticity* (Pergamon Press, New York, 1986).

[13] At the moment there is no practical proposal to beat the Standard Quantum Limit which could be readily implemented in LIGO. However, conceptual schemes can be found in, e.g.,

A. V. Syrtsev and F. Ya. Khalili, JETP **79** (3), 409-413 (1994);

S. P. Vyatchanin and A. B. Matsko, Zh. Eksp. Teor. Fiz. v.110 (1996) 1253 (*English translation:* JETP v.83(4), 690 (1996));

V. B. Braginsky, M. L. Gorodetsky, F. Ya. Khalili, Physical Letters A **A232**, 340-348 (1997)

and references therein.

Chapter 4 Runaway heating by r-modes of neutron stars in Low-Mass X-ray binaries (paper V)

To appear in ApJ

ABSTRACT

Recently Andersson et al., and Bildsten have independently suggested that an r-mode instability might be responsible for stalling the neutron-star spin-up in strongly accreting, Low Mass X-ray Binaries (LMXBs). We show that if this does occur, then there are two possibilities for the resulting neutron-star evolution:

If the r-mode damping is a decreasing function of temperature, then the star undergoes a cyclic evolution: (i) accretional spin-up triggers the instability near the observed maximum spin rate; (ii) the r-modes become highly excited through gravitational-radiation-reaction, and in a fraction of a year (0.13yrs in a particular model that we have considered) they viscously heat the star up to $T \sim 2.5 \times 10^9$K; (iii) r-mode gravitational-radiation-reaction then spins the star down in $t_{\text{spindown}} \simeq 0.08(f_{\text{final}}/130\text{Hz})^{-6}$yrs to a limiting rotational frequency f_{final}, whose exact value depends on the not fully understood mechanisms of r-mode damping; (iv) the r-mode instability shuts off; (v) the neutron star slowly cools and is spun up by accretion for $\sim 5 \times 10^6$yrs, until it once again reaches the instability point, closing the cycle. The shortness of the epoch of r-mode activity makes it unlikely that r-modes are currently excited in the neutron star of any galactic LMXBs, and unlikely that advanced LIGO interferometers will see gravitational waves from extragalactic LMXBs. Nevertheless, this cyclic evolution could be responsible for keeping the rotational frequencies within the observed LMXB frequency range.

If, on the other hand, the r-mode damping is temperature independent, then a steady state with constant angular velocity and $T_{\text{core}} \simeq 4 \times 10^8$K is reached, in which r-mode viscous heating is balanced by neutrino cooling and accretional spin-up torque is balanced by gravitational-radiation-reaction spin-down torque. In this case (as Bildsten and Andersson et al. have shown) the neutron stars in LMXBs could be potential sources of periodic gravitational waves, detectable by enhanced LIGO interferometers.

4.1 Introduction

Most of the rapidly accreting neutron stars in Low Mass X-ray Binaries (LMXBs) are observed to rotate in a strikingly narrow range of frequencies—from 260Hz to 330Hz (see, e.g., Van der Klis 1997). A natural explanation for this could be some mechanism which prevents further neutron-star spin-up once the rotational frequency is sufficiently high. Recently several such mechanisms were proposed:

White and Zhang (1997) suggested that magnetic braking could be responsible for halting the spin-up; this idea will not be discussed here. Bildsten (1998) pointed out that, because gravitational radiation reaction is a sharply increasing function of rotational frequency, it might halt the spin-ip. In his original manuscript, Bildsten identified one mechanism for triggering the necessary gravitational waves: lateral density variations caused by temperature dependence of electron capture reactions. While his manuscript was being refereed, Bildsten learned of the discovery that an r-mode instability, driven by gravitational radiation, can be very strong in spinning neutron stars (Andersson 1998, Friedman and Morsink 1998, Lindblom, Owen and Morsink 1998, Andersson, Kokkotas and Schutz 1998, Owen et al 1998); and the r-mode experts learned of Bildsten's gravitational-wave idea for saturating LMXB spinup. Both groups independently saw the connection: Bildsten (1998) and Andersson, Kokkotas and Stergioulas (1998) proposed that the r-mode instability could provide enough gravitational-radiation reaction to halt the LMXB spinup. In this letter we examine the consequences of this proposal.

Our conclusions depend crucially on whether the dissipation of the r-modes decreases with temperature (as is the case, e.g., when shear viscosity dominates the r-mode damping), or instead is temperature-independent (as is the case when, e.g., the mutual friction of proton and neutron superfluids dominates the damping). In the former case (Section 2 of this paper) we find that the neutron star will undergo a spin-up—heating—spin-down—cooling cycle; in the latter case (Section 3) it will probably settle down to a stable equilibrium state with an internal neutron-star temperature of about 4×10^8K.

4.2 The case of "viscous" r-mode damping

Let us consider first the case when dissipation is a decreasing function of temperature. We show that, if some r-modes become unstable in a neutron star spun up by accretion, then they heat up the neutron star through shear viscousity. As the neutron star heats up, the r-modes become more unstable. A thermo-gravitational runaway takes place, in which the r-mode amplitude grows, as a result of this growth the star's temperature rises, the dissipation becomes weaker and the instability becomes stronger. Within a fraction of a year the r-modes' gravitational radiation reaction spins the star down to a rotation frequency which is close to the minimum of the critical stability curve (probably around $100 - 150$Hz, but the exact value depends on poorly understood dissipation mechanisms—see below), with a final temperature of about 2×10^9K. The instability then shuts off and the star begins a several-million-year epoch of neutrino cooling and accretional spinup, leading back to the original instability point.

Figure 4.1 shows a typical evolutionary trajectory $A \rightarrow B \rightarrow C \rightarrow D \rightarrow B$ of the neutron star in the $\log(T_8) - \tilde{\Omega}$ plane, where T_8 is the temperature of the star's core measured in units of 10^8K, and $\tilde{\Omega} = \Omega/\sqrt{\pi G \bar{\rho}}$. Here Ω is the angular velocity of the neutron star and $\bar{\rho}$ is it's mean density. The portion $A \rightarrow B$ of the curve represents the accretional spin-up of the neutron star to the critical angular frequency $\Omega_{\mathrm{cr}}(T)$; $B \rightarrow C$ represents the heating stage in which the r-modes become unstable, grow and heat up the neutron star; $C \rightarrow D$ shows the spindown stage in which the r-mode amplitude saturates because of poorly understood nonlinear effects, and the angular velocity decreases due to the emission of gravitational radiation; and $D \rightarrow B$ represents cooling back to the equilibrium temperature with simultaneous spin-up by accretion. All four stages are discussed in more detail below.

The initial (steady-state) temperature T_0 of the neutron-star core in steadily accreting LMXB's is somewhat uncertain; according to Brown and Bildsten (1998), who analyzed heat transport during steady thermonuclear burning of the accreted material and nuclear reactions in the deep ocean, $T_0 = 1 - 4 \times 10^8$K. In Fig. 4.1 we
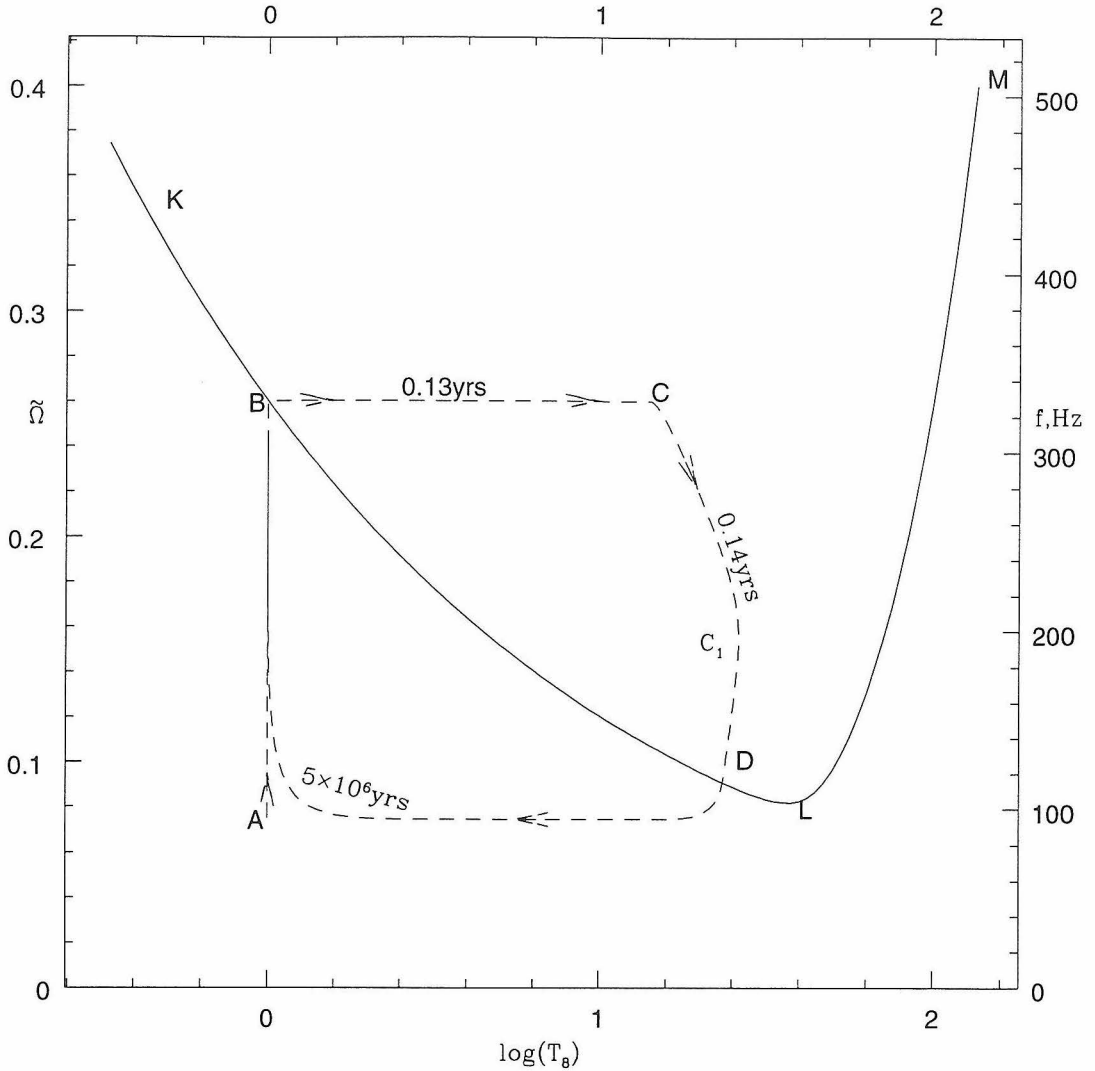
Figure 4.1: **Cyclic evolution of a strongly accreting neutron star in an LMXB.**

The r-mode damping is assumed to decrease with the temperature T of the neutron-star core. Line $K - L - M$ represents the "stability curve"; when the neutron star gets above this line, r-modes grow due to gravitational radiation reaction. Leg $A \to B$ of the evolutionary track represents the accretional spin-up of neutron star to the critical angular frequency; $B \to C$ represents the heating stage in which the r-modes become unstable, grow and heat up the neutron star; $C \to D$ shows the spindown stage in which the angular velocity decreases due to the emission of gravitational radiation; and $D \to B$ represents the neutron-star cooling back to the equilibrium temperature with simultaneous spin-up by accretion, thus closing the cycle.

assume $T_0 = 10^8$K.

The curve $K - L - M$ is the so-called r-mode "stability curve" (Lindblom, Owen and Morsink 1998). If the neutron star is represented by a point above the curve, then some r-modes in the star are unstable and grow. Otherwise, all r-modes decay. The portion $K - L$ of the stability curve is determined by the shear viscosity, or by mutual friction if part of the star is superfluid. Its exact location is uncertain precisely because the dissipation of the r-modes at the relevant temperatures is poorly understood. If shear viscosity dominates the dissipation, then the equation of the $K - L$ portion of the stability curve is given by

$$\tilde{\Omega}_{cr} = 0.1 \left(\frac{\eta}{\eta_0} \right)^{1/6} T_8^{-1/3}, \tag{4.1}$$

where η is the shear viscosity of the neutron star material, and η_0 is the shear viscosity due to electron-electron scattering in the neutron star [we have used Eqs (2.10), (2.14), (2.15) and Table I of Owen et al. (1998) to work out Eq. (4.1)]. If only shear viscosity due to to electron-electron scattering were operating, with the shear viscosity given by $\eta_0 = 347\rho^{9/4}T^{-2}$, where all quantities are in cgs units (see Cutler and Lindblom 1987 and references therein), then the critical rotational frequency at $T = 10^8$K would be 130Hz, which is much less than observed values (van der Klis 1998). However, the friction is probably larger than this (and therefore Ω_{cr} is also larger) because of interaction of the core fluid with the crust and maybe mutual friction in a superfluid state. The emphasis of this paper is not to figure out whether the r-mode instability is relevant for LMXBs, but to investigate the consequences if it is relevant. For purpose of illustration, we assume that $\eta = 244 \times \eta_0$; this makes the critical rotational frequency 330Hz at $T = 10^8$K, which is consistent with observations (van der Klis 1998). This choice of viscosity is a cheat since we don't yet know the T and ρ-dependence of η. However, unless the damping is due to mutual friction, η is likely to decrease with increasing temperature, which is a sufficient condition for thermo-gravitational runaway. Our choice of viscosity possesses this feature; therefore we believe it has a good chance of representing the real physics.

The portion $L - M$ of the stability curve is determined by bulk-viscosity dissipation; it's exact location is also a subject of yet unsettled controversy [the heart of the problem is the calculation of Lagrangian perturbation in density (Lindblom, Owen and Morsink 1998, Andersson, Kokkotas and Schutz 1998), which, to our best knowledge, has not been reliably carried out by any of the groups]. Of the two current estimates of the bulk-viscosity contribution to damping of the r-modes, we have chosen the one which gives the higher values of $\tilde{\Omega}_{cr}$, thus maximizing its effect (see Lindblom, Owen and Morsink 1998). The fact that, for the evolution curve shown in Figure 4.1 no part is in the region where the bulk viscosity dominates suggests that the details of the bulk viscosity will not be of particular importance.

In this work for concreteness we specialize to a polytropic model of a neutron star with $p \propto \rho^2$, and consider the r-mode with $l = m = 2$, which is expected to have the strongest instability in such polytropes (Friedman and Morsink 1998, Lindblom, Owen and Morsink 1998). We assume that the time evolution of the normalized angular velocity $\tilde{\Omega} = \Omega/\sqrt{\pi G \bar{\rho}}$ of the star and the dimensionless amplitude α of the r-mode are given by phenomenological Equations (3.14), (3.15), (3.16) and (3.17) of Owen et al. (1998):

$$\frac{d\tilde{\Omega}}{dt} = -\frac{2\alpha^2 Q}{1 + \alpha^2 Q} \frac{\tilde{\Omega}}{\tau_v} + \sqrt{\frac{4}{3} \frac{1}{\tilde{I}} \frac{\dot{M}}{M}} \times p, \tag{4.2}$$

$$\frac{d\alpha}{dt} = -\left(\frac{1}{\tau_{\text{grav}}} + \frac{1}{\tau_v} \frac{1 - \alpha^2 Q}{1 + \alpha^2 Q} \right) \alpha \tag{4.3}$$

when $\alpha^2 < k$ (the saturation value of α^2, which we assume to be $k = 1$), and by

$$\alpha^2 = k, \tag{4.4}$$

$$\frac{d\tilde{\Omega}}{dt} = \frac{2\tilde{\Omega}}{\tau_{\text{grav}}} \frac{kQ}{1 - kQ} \tag{4.5}$$

when α is saturated due to not yet understood non-linear effects. Here α is the dimensionless amplitude of the r-mode defined by Eq. (1) of Lindblom, Owen and Morsink (1998), and τ_v and τ_{grav} are the viscous and gravitational timescales for the

r-mode dissipation and are given by Eqs. (2.14) and (2.15) of Owen et al. (1998):

$$\tau_{\text{grav}} = -3.26\tilde{\Omega}^{-6}\text{sec},$$
$$\frac{1}{\tau_v} = \frac{1}{\tilde{\tau}_s}\left(\frac{10^8\text{K}}{T}\right)^2 + \frac{1}{\tilde{\tau}_B}\left(\frac{T}{10^8\text{K}}\right)^6\tilde{\Omega}^2. \tag{4.6}$$

In the above equation the viscous damping rate is a sum of contributions from the shear and the bulk viscosities; the former is determined by $\tilde{\tau}_s$ which we took to be 1.03×10^4sec in order to fit the observed data; the latter is determined by $\tilde{\tau}_B$ which is taken to be 6.99×10^{14}sec, in agreement with Owen et al. (1998).

Note that τ_{grav} is negative since gravitational radiation always amplifies the r-mode. The second term in Eq. (4.2) represents the neutron-star spin-up by accretion; M and $\dot{M}$ are the mass of the neutron star and its accretion rate respectively, and p is a factor of order unity which depends on the accretion radius and the angular velocity of the neutron star; it's exact value is not essential for the physics discussed here and we set $p = 1$ from here onwards. The numerical parameters Q and $\tilde{I}$ are given by 0.094 and 0.261 respectively for a polytrope star of adiabatic index $\gamma = 2$ (Lindblom, Owen and Morsink 1998). For the evolution shown in Fig. 4.1 we took $M = 1.4M_\odot$ and $\dot{M} = 10^{-8}M_\odot/\text{yr}$, and we assumed a random initial perturbation of magnitude $\alpha = 10^{-8}$ when the neutron star reaches the stability curve $K - L$.

Now consider the star's thermal evolution. The r-mode deposits heat into the star at the rate

$$W_{\text{diss}} = \frac{2E_{\text{r}-\text{mode}}}{\tau_v} = \frac{\alpha^2\Omega^2 M R^2 \tilde{J}}{\tau_v}, \tag{4.7}$$

where $E_{\text{r}-\text{mode}}$ is the energy in the r-mode [cf. Eq. (3.11) of Owen et al. (1998)]. Here R is the radius of the neutron star taken to be 12.53km, and $\tilde{J} = 1.635 \times 10^{-2}$ for the polytropic model considered here. At the relevant temperatures the neutron star is expected to cool predominantly by the modified URCA process (this is not entirely true, since close to 10^8K neutrino bremstruhlung cooling from the crust and radiative cooling by photons might become significant. However, their cooling rates are not significantly larger than that of the modified URCA process at 10^8K, and they

become negligible at higher temperatures. In this work for simplicity we assume that modified URCA is the only cooling process; the inclusion of other processes would not change the general evolutionary picture). The modified URCA cooling rate, reduced by heating from nuclear reactions in the deep crust, is given by (Shapiro and Teukolsky, 1983)

$$L_{\text{cool}} = 7 \times 10^{31}(T_8^8 - \bar{T}_8^8)\text{erg/sec.} \tag{4.8}$$

Here the subscript 8 indicates that the temperature is measured in units of 10^8K and $\bar{T}$ is the equilibrium temperature of the neutron star before the r-mode heating starts, taken to be 10^8K for our calculation. The thermal evolution equation is then given by

$$\frac{dT}{dt} = \frac{W_{\text{diss}} - L_{\text{cool}}}{C_v}, \tag{4.9}$$

where C_v is the heat capacity of the neutron star, taken to be $1.4 \times 10^{38}(\text{erg/K}) \times T_8$ [from Shapiro and Teukolsky (1983), Eq. (11.8.2). However, the heat capacity of neutron star with a superfluid core is less].

Equations (4.2), (4.3), (4.5), (4.4) and (4.9) determine the time evolution of the angular velocity Ω and temperature T. Figure 4.1 shows the predicted evolution, for the representative parameter values, introduced above. The evolution consists of four stages:

The first stage $A \rightarrow B$ is the spin-up of the neutron star, during which it's angular velocity Ω is increasing towards the critical one, and the r-mode instability is suppressed by viscosity; since we assume that the star begins at its equilibrium temperature $T_8 = \bar{T}_8 = 1$, its temperature changes little during the spin-up. For an assumed accretion rate of $10^{-8}M_\odot/$yr this stage takes $\sim 5 \times 10^6$ years.

When the angular velocity reaches its critical value, the r-mode starts to grow and the second stage $B \rightarrow C$ begins. The neutron star gets heated up by the r-mode through viscosity, the r-mode becomes more unstable, and thermo-gravitational runaway follows. It takes 0.13 years for the r-mode's amplitude to evolve from $\alpha = \alpha_{\text{W}}$ to $\alpha = 1$, where $\alpha_{\text{W}} \simeq 1.2 \times 10^{-5}$ is the value of the r-mode amplitude at which the accretional torque is exactly compensated by the gravitational radiation reaction [see

Wagoner (1984)]. For our intuition it is useful to define two characteristic α-dependent timescales for stage $B \to C$: the thermal timescale [cf Eq. (4.7)]

$$t_{\text{th}} = \frac{dt}{d \log T} = \frac{C_v T}{W_{\text{diss}}} \sim 3.7 \times 10^{-5} T_8^2 \frac{\tau_v}{\alpha^2} \qquad (4.10)$$

and the timescale for the decrease of angular velocity [cf Eq. (4.2)]

$$t_\Omega = \frac{dt}{d \log \Omega} \simeq \frac{1}{2Q} \frac{\tau_v}{\alpha^2} \simeq 5 \times \frac{\tau_v}{\alpha^2}. \qquad (4.11)$$

Clearly, the neutron star heats up much faster than it spins down due to gravitational radiation. Therefore, during this stage the angular velocity of the star decreases by only a small amount, $\Delta \tilde{\Omega} = 0.0003$. Physically, the reasons for such little change in $\tilde{\Omega}$ are that the r-mode amplitude grows so quickly, and that in this phase the angular momentum loss is not manifested in a reduction of the angular velocity, but instead in the growth of the r-mode itself (the r-mode which is driven by gravitational radiation reaction carries a negative angular momentum).

Eventually the r-mode amplitude saturates due to nonlinear effects. This initiates the third stage of the evolution, in which all of the angular momentum loss is manifested by reduction of angular velocity (since the r-mode cannot grow any more), and the star spins down $C \to D$ to the critical angular velocity. At point C_1 the temperature of the neutron star is such that the neutrino cooling exactly compensates the dissipative heating from the r-modes. After that the temperature does not change much until the spin-down stage is terminated. The physical reason for this is that even though the thermal timescale at $C_1 \to D$ is comparable or smaller than the spindown timescale, the rate of dissipative heating does not change much. If the heat capacity C_v of neutron star were zero, we would have $W_{\text{diss}} = L_{\text{cool}}$ at all points of $C_1 \to D$. This would imply $T \propto \Omega^{1/4}$, so even then the temperature would not change significantly over this last part of the spin-down.

An analytical expression for the duration of this rapid spin-down stage can be

derived from Eqs (4.5) and (4.6):

$$t_{\text{spindown}} \simeq 0.08(1/k)(\tilde{\Omega}_f/0.1)^{-6}\text{yr}, \tag{4.12}$$

where Ω_f is the angular velocity at the end of the spin-down. In our simulations t_{spindown} is about 0.14 years.

After the neutron star reaches the stability curve, the r-mode is damped by viscosity stronger than it is driven by gravitational-radiation reaction; therefore its amplitude decreases and the neutron star cools back to its original equilibrium temperature, while being spun up by accretion. This part of the evolution is represented by $D \to B$ on Fig. 4.1; its timescale is the same as that for the original accretional spin-up, i.e. $\sim 5 \times 10^6$ years. After this the cycle is closed and can repeat itself as long as the accretion continues.

We believe that the sharp kink at point C is not a real physical effect, but a result of our poor understanding of the non-linear saturation of the r-mode; however, this artificial feature of our simulations does not seem to affect the existence of the thermo-gravitational runaway and the subsequent rapid spin-down to a lower angular velocity. Despite a large number of uncertainties in the details of the evolution, we believe that this scenario is robust so long as the r-mode instability does occur in LMXBs, and the damping of the r-modes decreases with temperature.

If the above described evolutionary scenario is generic, it is then clear that none of the currently observed LMXBs can possess an actively operating r-mode instability—otherwise we would observe a rapid spindown on a time-scale less than a year. However, it is conceivable that many of the neutron stars in these LMXBs have undergone the r-mode instability at some stage of their evolution, and are currently below the stability curve, evolving along leg $D \to B$ of Fig. 1.

From Equations (4.12) and (4.2) we can estimate the fraction r of neutron stars in extragalactic LMXBs that are in the phase of active emission of gravitational waves:

$$r = \frac{t_{\text{spindown}}}{t_{\text{accretion}}} \sim 1.6(1/k) \times 10^{-8} \left(\frac{\tilde{\Omega}_f}{0.1}\right)^{-6}. \tag{4.13}$$

The quantity $\tilde{\Omega}_f$ is bounded from below by the rotational frequencies of young pulsars (this statement is true only if the r-mode damping is the same for young and old pulsars at the same temperatures). The rotational frequency of the recently discovered N157B (Marshall et al 1998) is 62.5Hz. Using the braking index theory one can project the initial rotational frequency of this pulsar to be no smaller then 100Hz, which implies $\tilde{\Omega}_f > 0.08$. Therefore, only $r < (6/k) \times 10^{-8}$ of neutron stars in extragalactic LMXBs are in the phase of rapid gravitational wave emission, which implies that to catch one star in this phase, gravitational-wave detectors must reach out through a volume large enough to encompass $\sim 0.1 - 0.01/r \sim 10^6$ galaxies like our own (this assumes that there are $10 - 100$ strongly accreting neutron stars in LMXBs in our galaxy). An analysis similar to that of Owen et al (1998) shows that even "advanced LIGO" detectors are unlikely to be able to see these sources at such great distances.

4.3   The case of temperature-independent r-mode damping

There is a possible alternative evolutionary scenario which is similar to the one proposed by Bildsten (1998) and Andersson, Kokkotas and Stergioulas (1998) (we thank Lee Lindblom for pointing this out). It may be that the r-mode damping is dominated not by normal dissipative processes, but by mutual friction in the neutron-proton superfluid. Detailed calculations of the effect of such friction on the r-mode damping are in progress (Lindblom and Mendell); however for our analysis the essential feature of this dissipative process is already known: it is temperature independent. Therefore, if this process dominates, one would not expect a thermo-gravitational runaway; instead the neutron star will reach a state of three-fold equilibrium. The neutron star will "sit" on the stability curve $[(1/\tau_{\mathrm{grav}}) + (1/\tau_v) = 0]$, the amplitude of the r-mode will adjust so that the accretional torque is compensated by the gravitational-radiation reaction torque ($\alpha = \alpha_W \simeq 1.2 \times 10^{-5}$ for our model), and the temperature of the neutron star will adjust so that the cooling compensates the frictional heating from

the r-mode: $W_{\mathrm{diss}} = L_{\mathrm{cool}}$. From Eqs (4.2), (4.6), (4.7) and (4.8) one can work out the equilibrium temperature:

$$T_{\mathrm{eq}} = 4.2 \times 10^8 \mathrm{K} \left(\frac{f}{330\mathrm{Hz}} \right)^{1/8} \left(\frac{\dot{M}}{10^{-8} M_\odot/\mathrm{y}} \right)^{1/8} \left(\frac{1.4 M_\odot p}{M} \right)^{1/8}, \qquad (4.14)$$

where f is the rotational frequency of the star.

It is interesting to examine how (and whether) the star reaches this equilibrium point. For temperature-independent damping, Eqs (4.2) and (4.3) form a closed system with two independent variables, $\tilde{\Omega}$ and α. To investigate the behavior of the star after it reaches the stability curve at $\tilde{\Omega} = \tilde{\Omega}_{\mathrm{cr}}$, we set $\tilde{\Omega} = \tilde{\Omega}_{\mathrm{cr}} + \tilde{\Omega}_1$ and expand Eqs (4.2) and (4.3) to first order in $\tilde{\Omega}_1$. After trivial algebraic manipulations, we can then reduce the system of two first-order differential equations to a single second-order differential equation:

$$\frac{d^2 x}{dt^2} + \gamma(x) \frac{dx}{dt} = -\frac{\partial V(x)}{\partial x}. \qquad (4.15)$$

Here $x = \ln \alpha$, and $\gamma(x)$ and $V(x)$ are given by

$$\gamma(x) = \frac{2Q \exp(2x)}{\tau_v} \qquad (4.16)$$

and

$$V(x) = \frac{6}{\tau_{\mathrm{grav}}} \left(\frac{Q \exp(2x)}{\tau_v} - \frac{x}{\tau_{\mathrm{acc}}} \right). \qquad (4.17)$$

In the above Equations τ_{grav} is given by Eq. (4.6), and $\tau_{\mathrm{acc}} = (1/p)\sqrt{(3/4)}\tilde{\Omega}_{\mathrm{cr}} \tilde{I} M/\dot{M}$ is the timescale for the neutron star to be spun up by accretion to the angular frequency Ω_{cr}.

Clearly Eq. (4.15) can be thought of as an equation of motion for a particle of unit mass in the potential well given by $V(x)$ and with the damping $\gamma(x)$. The bottom of the potential well corresponds to the equilibrium state described above, and the damping insures that the "particle" gets there (i.e. that the neutron star settles into the equilibrium state). However, the damping is small. To see this, consider damped oscillatory motion close to the bottom of the well. The complex angular frequency of

this motion is given by

$$\omega = \sqrt{12/(\tau_{\text{acc}}\tau_{\text{grav}})} - i/(2\tau_{\text{acc}}).$$ (4.18)

The period of these small oscillations is

$$P \sim 230 \left(\frac{M}{1.4M_\odot}\right)^{1/2} \left(\frac{10^{-8}M_\odot\text{y}^{-1}}{\dot{M}}\right)^{1/2} \left(\frac{f}{330\text{Hz}}\right)^{-5/3} \text{y},$$ (4.19)

but the timescale on which they are damped (i.e. the timescale on which the equilibrium is reached) is $\tau_{\text{eq}} \sim 2\tau_{\text{acc}} \sim 10^7\text{y}$.

Since the damping is so small, fluctuating disturbances may keep this nonlinear oscillator off it's equilibrium position. For example, in our evolutionary scenario we have assumed that there is a mechanism which gives α some non-zero initial value. Presumably, the same mechanism could keep the oscillator in an excited state. Then the amplitude of the r-mode, and hence the temperature of the star's core, would vary on the timescales of hundreds of years. Detailed investigation of these issues is a subject for further work. However it is clear that the time-averaged temperature should be close to the equilibrium value given by Eq. (4.14).

If the r-mode damping does not depend on temperature, we can expect r-modes to be excited in many of the rapidly rotating neutron stars in LMXBs. These presumably superfluid steady gravitational-wave emitters could be detected by enhanced LIGO gravitational wave detectors, as discussed in Bildsten (1998) and Andersson, Kokkotas and Stergioulas (1998). Recently, Brady and Creighton (1998) have considered the computational cost of such detection. Their conclusion was that with the enhanced LIGO sensitivity and available computational capabilities one could detect gravitational-wave emitters in LMXBs that are as bright in X-ray flux as SCO-X1.

If the rotational frequency of the emitting neutron star is localized to within a few 10s of Hz using astronomical observations (by, e.g., QPO's), one could narrow-band the interferometer response around the frequency of r-mode oscillations (see e.g. Meers 1988). This could allow LIGO to detect gravitational-wave emitters in LMXBs

which are $10 - 100$ times dimmer in X-ray flux than SCO-X1.

Positive detection of gravitational waves at the r-mode oscillation frequency would make a strong case for the superfluid nature of the r-mode damping.

4.4   Conclusions

In this paper we have investigated the recent proposal that the accretional spin-up of the neutron star in an LMXB is stopped by r-mode gravitational radiation reaction. There are two possible evolutionary scenarios. In the first scenario, the neutron star goes through cycles such as that shown on Fig. 4.1. The necessary condition for this scenario to be relevant is that r-mode damping should decrease with increasing temperature. In this case, it is very unlikely that any of the currently observed neutron stars in LMXBs in our galaxy are in the r-mode excited phase of the cycle. The detection of gravitational radiation from extragalactic LMXBs in the r-mode excited phase is also not likely, even with advanced LIGO interferometers.

In the second scenario, r-mode damping is temperature independent, and a steady-state equilibrium is probably reached, where both angular velocity and temperature stay constant, or are oscillating with periods of several hundreds of years. Equation (4.14) makes a robust prediction for the temperature of these objects to be $\simeq 4 \times 10^8 \text{K}$; this temperature is on the high end of what is typically expected; and it might be possible to test this prediction by observations. In this case the neutron stars are emitters of periodic gravitational waves, which could be detected by interferometers like enhanced LIGO.

Acknowledgements

Bibliography

[1] Andersson, N. 1998, ApJ, **502**, 708.

[2] Andersson, N., Kokkotas, KD. and Stergioulas, N. 1988, ApJ, in press (astro-ph/9806089).

[3] Andersson, N., Kokkotas, KD. and Schutz, B. F., ApJ, in press (astro-ph/9805225).

[4] Bildsten, L., ApJ, 501, L89.

[5] Brady, P. R. and Creighton, T. D. 1998, in preparation.

[6] Brown, E. F. and Bildsten, L. 1998, ApJ, 496, 915.

[7] Cutler, C. and Lindblom, L. 1987, ApJ, 314, 234.

[8] Friedman, J. L. and Morsink, S. 1998, gr-qc/9706073 [to appear in ApJ].

[9] Lindblom, L. 1995, ApJ, 438, 265.

[10] Lindblom, L. and Mendell, G. 1995, ApJ, 444, 804.

[11] Lindblom, L. and Mendell, G. 1998, in progress.

[12] Lindblom, L., Owen, B. J. and Morsink, S. 1998, Phys. Rev. Lett., 80, 4843.

[13] Marshall, F. E. et al. 1998, ApJ, 499, L179.

[14] Meers, B. J. 1988, Phys. Rev. D, 38, 2317.

[15] Mendell, G. 1991, ApJ, 380, 530.

[16] Owen, B. J. et al. 1998, Phys. Rev. D, **58**, 084020.

[17] Shapiro, S. L. and Teukolsky, S. 1983, Black Holes, White Dwarfs and Neutron Stars (John Wiley and sons, New York).

[18] van der Klis, M. 1998, in Proc. NATO/ASI Conf. Ser. C, The many faces of neutron stars, ed. R. Buccheri, J. van Paradijs and M. A. Alpar (Dordrecht: Kluwer), in press (astro-ph/9710016).

[19] Wagoner, R. V. 1984, ApJ, 278, 345.

[20] White, N. E. and Zhang, W. 1997, ApJ, 490, L87.